The temperature dependent optical properties of (circum)stellar dust analogs in the infrared

Dissertation

Zur Erlangung des akademischen Grades
Doktor rerum naturalium (Dr.rer.nat.)

vorgelegt dem Rat der physikalisch-astronomischen Fakultät der Friedrich-Schiller-Universität Jena

von **Dipl.-Phys. Simon Zeidler**
geboren am **28.08.1982 in Halle/Saale**

Gutachter:

1. Prof. Dr. Ralph Neuhäuser
2. assoc. Prof. Dr. Anja Andersen
3. Prof. Dr. Annemarie Pucchi

Tag der Disputation: 04. Juli 2013

Contents

1 Introduction **4**
1.1 Dust in astronomical environments 4
1.2 Spectroscopy of circumstellar dust 5
1.3 Influence of temperature on dust spectra 6
1.4 Structure of this work 7

2 Theoretical considerations on the optical properties of solids **8**
2.1 Interatomic potential and the energy of crystal lattices 8
2.1.1 Energetic description of bonds 8
2.1.2 Lattice vibrations 10
2.1.3 Quantum mechanical view on the energy of bonds 12
2.2 The influence of the temperature on anharmonic potentials 13
2.2.1 The mode Grüneisen parameter 13
2.2.2 Phonon-phonon interaction and the phonon self energy 15
2.3 Interaction of electromagnetic fields with solids 19
2.3.1 Classical description of external excitations 19
2.3.2 Quantum mechanical view on external excitations 23
2.3.3 The FPSQ model 24
2.3.4 Contributions of higher order phonon processes 27
2.3.5 Crystal field theory/Ligand field theory 29
2.4 Optical properties of small particles 32
2.4.1 Spherical particles 32
2.4.2 Ellipsoidal particles 34
2.4.3 Irregularly shaped particles 36

3 Experimental setup for temperature dependent in-situ spectroscopy in the IR and NIR **38**
3.1 Temperature dependent IR reflection measurements 38
3.1.1 The Bruker FTIR spectrometer 38
3.1.2 Low-temperature measurements 39
3.1.3 High-temperature measurements 40
3.1.4 Performing reflection measurements 42
3.2 Temperature dependent NIR transmission measurements 44

3.2.1 The Lambda 19 NIR-UV spectrometer . . . 44
3.2.2 Low-temperature measurements . . . 45
3.2.3 Transmission measurements with the HTHP cell . . . 45
3.2.4 Performing transmission measurements . . . 46

4 Temperature dependent reflection spectra of selected oxides and silicates 47
4.1 Corundum . . . 47
4.1.1 Properties . . . 47
4.1.2 Reflection data and fit results . . . 49
4.1.3 Development of the fit parameters with the temperature . . . 51
4.2 Spinel . . . 55
4.2.1 Properties . . . 55
4.2.2 Reflection data and fit results . . . 56
4.2.3 Development of the fit parameters with temperature . . . 58
4.3 Quartz . . . 60
4.3.1 Properties . . . 60
4.3.2 Reflection data and fit results . . . 62
4.3.3 Development of the fit parameters with temperature . . . 64
4.4 Olivine . . . 65
4.4.1 Properties . . . 65
4.4.2 Reflection data and fit results . . . 67
4.4.3 Development of the fit parameters with temperature . . . 71
4.5 Enstatite . . . 72
4.5.1 Properties . . . 72
4.5.2 Reflection data and fit results . . . 75
4.5.3 Development of the fit parameters with temperature . . . 77
4.6 Concluding remarks . . . 79

5 Temperature dependent transmission spectra of olivine 80
5.1 Multiphonon absorption in the NIR . . . 80
5.1.1 ϵ_∞ at high temperatures . . . 80
5.1.2 Multiphonon absorption at low temperatures . . . 80
5.2 Crystal field bands in the NIR-VIS . . . 82

6 Applications on the astronomical spectral analysis 87
6.1 The 13 μm feature of oxygen rich AGB stars . . . 87
6.1.1 The influence of the grain-shape on the 13 μm feature of corundum and spinel at RT . . . 89
6.1.2 Temperature dependent spectral properties of small corundum and spinel grains . . . 91
6.1.3 Temperature distribution . . . 93

6.2 Silicates in protoplanetary disks - features as temperature indicator 94

7 Conclusions **99**

8 Zusammenfassung **101**

Appendices **103**

A Oscillator parameters of the reflectance fits **104**

1. Introduction

1.1. Dust in astronomical environments

In 1853, *Angelo Secchi* postulated the existence of interstellar matter as being responsible for the apparent weakening of light in specific regions of our galaxy due to extinction (absorption and scattering). Since that time, the question of the composition of this interstellar matter has become an important subject of astronomical research. As it has become clear that dust is a probable constituent of the interstellar matter, the question rose what is the role of dust in the universe, a question that could not be answered till basic theoretical considerations of dust in cosmic environments have been obtained in the 1960s and 70s and not till pioneering discoveries have been made by the astronomers with modern observational techniques like space telescopes. Today it is known that dust exists almost everywhere in space and takes part in almost all processes in the universe. Investigation of the role of dust in these processes is the main task of laboratory astrophysics, and especially spectroscopy acts as an important instrument for analysis of dust in the lab or in space.

Almost all dust that is found in space was created in supernovae[1] and in the outflows of stars on the asymptotic giant branch (AGB). In the close environment of an AGB star ($T \approx$1000–2000 K, $p \approx 10^{-8}$–10^{-10} bar), small solid particles can condense from the gas that is ejected by the star (Molster and Waters, 2003). In general, most of the new formed dust is amorphous and consists of silicates[2] and carbon. Accelerated by the stellar winds of their host stars, the dust enters the interstellar medium (ISM) where it is confronted with the influences of energetic radiation (protons, ultraviolet light, etc.) over long periods of time which can change the inner structure of dust grains and is even able to destroy them. It has been also found that in the ISM there must be a still unknown process that leads to grain formation, too[3] (Molster and Waters, 2003). So far, only amorphous material but no signs of crystalline material have been found in the dust of the ISM which is usually gathered to huge clouds

[1] Unfortunately, dust production in supernovae is still not well understood because of the short period of their existence which make it difficult to get analyzable spectra.

[2] The ratio of amorphous to crystalline dust is actually depending on the mass loss rate of the star (Blommaert et al., 2007)

[3] The median lifetime of dust in the ISM is limited to about 4×10^8 yrs and a replenishment of the respective material will take 2.5×10^9yrs but the existence of dust in the ISM is proven by infrared spectroscopy (especially by the strong 10 μm absorption feature of the silicates)

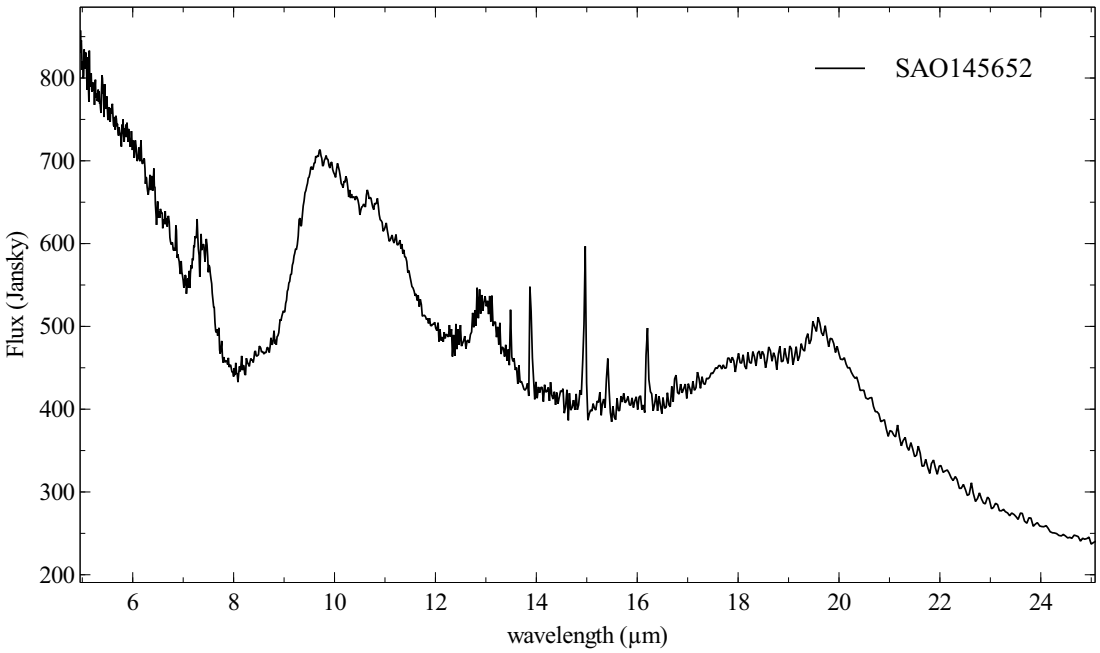

Figure 1.1.: Emission spectrum of the M-star SAO145652 in the wavelengths range 5–25 μm.

together with hydrogen and helium gas. Excited by e.g. shock waves from supernovae, these clouds can start to collapse to form a new star. Because of momentum conservation, the gravitation, and the stellar wind of the young star, a surrounding protoplanetary disk (PPD) can be created from the accreting material which at last can form a new planetary system and close the 'life cycle' of cosmic dust.

1.2. Spectroscopy of circumstellar dust

Spectroscopy is one of the most important instruments in astrophysics for the identification of cosmic materials. With the aid of infrared (IR) spectroscopic analysis of e.g. dust envelopes around AGB stars, many dust components could already be identified, which gives fundamental insights in the still not completely understood dust production in space. As for M-stars (oxygen rich AGB stars), besides the broad and smooth IR emission bands of metal-rich amorphous silicates (olivine composition), crystalline Mg-rich silicates like forsterite (Mg_2SiO_4) and enstatite ($MgSiO_3$) but also diverse oxides like Mg/Al-oxides have been found in the spectra (Molster and Waters, 2003). In PPDs of young stellar systems, crystalline materials in form of forsterite, carbonates and even iron-sulfide (FeS) have been identified by IR spectroscopy whereas it is assumed that the amorphous silicates in PPDs are rather metal-poor (pyroxene composition) (Molster and Waters, 2003).

Since the dust around AGB stars is condensing directly from the outflow of the star, it should be in a somewhat thermal equilibrium with the gas. Therefore, the first condensing

crystalline dust can be expected to be comparably hot which means an enhanced emission compared to cold dust due to the Planck law[4]. As an example, in Fig. 1.1 the emission spectrum of the M-star SAO145652 is shown. The two strong spectral features at around 10 and 20 μm wavelengths are due to the fundamental asymmetric stretching and bending vibrations of the $[SiO_4]^{4-}$ tetrahedron, the basic unit of all silicates (Hinz, 1970) and therefore especially visible as broad features in spectra of amorphous silicates. However, crystalline silicates usually have a much more complex spectrum. They show several strong and sharp features also at around 10 μm wavelengths (the exact positions depend on the material) and other sharp features from 20 to 70 μm wavelengths. Crystalline Aluminum oxides like corundum or spinel are responsible for the strong and distinct spectral feature at around 13 μm (Posch et al., 1999; Fabian et al., 2000). The existence of amorphous Al oxide that is characterized by a very broad feature from 10 to 20 μm wavelengths with a maximum emission at around 11.3 μm (Begemann et al., 1997) cannot be verified in this spectrum but has been identified in spectra of M-stars with lower mass loss rates ($<10^{-7}M_\odot$/yr).

The first considerations of the composition of the dust can be drawn with the aid of the spectral features of the respective constituent known from laboratory measurements on earth. However, if a particular fit to an emission spectrum has to be done or a model for the emission of circumstellar dust shall be established, also the optical constants (real and imaginary part of the refraction index) of the respective constituents need to be determined. From the optical constants, the spectral emission cross section of particles can be calculated that allows a direct comparison with astronomical emission spectra. Juhasz et al. (2010) did this in case of PPDs of Herbig Ae/Be stars.

1.3. Influence of temperature on dust spectra

The influence of the temperature on spectra of dust is twofold. On the one hand, temperature dependent emission of light of heated solid matter follows the Planck-law (extrinsic). On the other hand, the actual spectral emission profile is determined by the physical properties of the respective material which are also temperature dependent (intrinsic). The product of both intrinsic and extrinsic processes leads to the emission spectrum of a material. Though, while the Planck-law is well known, the temperature dependence of the physical properties is somehow individual for each material and has to be determined by measurements if the particular emission shall be known.

In the case of low temperatures (T<300 K) temperature dependent spectral measurements have been done already since many years with great success (Boudet and Mutschke, 2006; Koike et al., 2006; Suto et al., 2006) but in the case of hot environments as they appear

[4]In some AGB stars also spectral absorption features from cold dust in the outer regions could be taken.

around stars still laboratory spectra taken at room temperature (RT) are used for analyzing the dust spectra although the temperature effects could be even bigger than in the case of cold regions. Additionally, temperature dependent spectra would help to give a thermometer for the respective dust component in a disk and therefore would give important insights in the temperature distribution of a dust disk or dust envelope which is quite important in understanding the formation of dust or even the structure of a dust disk and dust envelope, respectively.

1.4. Structure of this work

This thesis is structured as follows:

- The second chapter concentrates on the theoretical basics of the temperature dependence of the optical properties of solids. Though, also the theoretical aspects of the interaction of light with both bulk materials and particles, respectively, are treated. In the beginning of this chapter, some basic points about bonds in solids are presented before the influence of the temperature in solids on a microscopic level is discussed.
- In the third chapter, the experimental equipment that has been used to perform temperature dependent spectroscopic measurements from IR to visible (VIS) wavelengths is introduced.
- In the fourth and the fifth chapter, the theoretical insights from the second chapter are combined with the results of spectroscopic measurements of materials with astrophysical relevance at low and high temperatures. Two main groups of materials are treated: oxides and silicates. The fourth chapter concentrates on oscillator-fits of the results of IR spectroscopic reflection measurements which are important to determine the optical constants of the samples in the IR. The fifth chapter focuses on near infrared (NIR)–VIS transmission measurements of olivine (Mg-Fe silicate) samples.
- In the sixth chapter, important implications of the considerations from the preceding chapters on astrophysical spectral analysis are discussed. An explanation for the origin of the 13 μm feature in spectra of oxygen rich AGB stars is given and the temperature of silicate rich dust in protoplanetary disks is discussed. Therefore, the calculated optical properties are used to derive small-particle spectra of the respective material from the models which have been introduced in the second chapter.
- In the seventh chapter, the final conclusions about the results are given.

2. Theoretical considerations on the optical properties of solids

2.1. Interatomic potential and the energy of crystal lattices

2.1.1. Energetic description of bonds

A bond between two atoms (or ions) can be seen as flexible. The reason is the form of the potential energy distribution over the distance (r) between the two atoms. In principle, there are two forces which define the potential energy in bonds: an attractive and a repulsive force. As attractive forces, Coulomb forces between differently charged ions ($\sim -r^{-2}$) and between atoms sharing electron-pairs, respectively, can account while due to the Pauli principle a further proximity would lead to very strong repulsive forces (approximated by $\sim r^{-13}$). Though, the repulsive forces are short ranged compared to the attractive ones and therefore a minimum in the potential energy can be found which defines the equilibrium distance (r_0) between bonded atoms (or ions). In Fig. 2.1 the principal shape of such a potential energy distribution is sketched. Potentials of those shape are called anharmonic. $E_{lattice}$ describes the minimum of the potential energy. Actually, that is the bond energy which is released by the approach of the atoms/ions from infinity toward each other.

With this simple model in mind, a bonded atom can move around r_0 by giving him kinetic energy. The movement or vibration in such a potential is also called the mode of the respective bond.

In a crystal, the particles are connected over the bonds with their neighboring atoms/ions to the entirety of all particles in the crystal. In particular, the ordering of the atoms/ions is periodic over long ranges so that a lattice of particles is formed: the crystal lattice[1]. The units of periodicity in a lattice are called *unit cells*. The unit cells are chosen to reflect the principal structure of the crystal and some of its properties like isotropy[2]. If different structures or different atoms are a part of the lattice, the smallest unit that builds the

[1] Contrary to crystals, amorphous solids like glasses or sol-gel materials do not show a long-range order of the atoms

[2] In general, unit cells are not the smallest units; that are the *primitive cells*

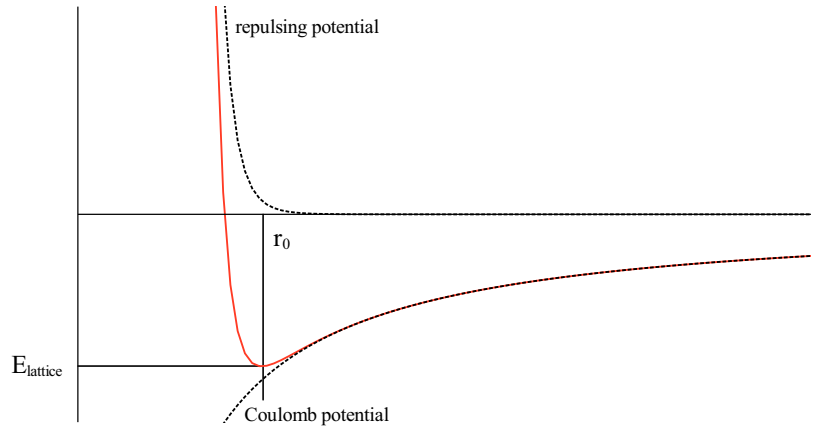

Figure 2.1.: The principle shape of a resulting anharmonic potential (red) between atoms/ions. Presented here is the case of an ionic bond with the attractive Coulomb potential and the repulsive potential of the electron envelope (both black dotted).

crystal structure is called the *base* of the crystal and lies on each lattice point (Ashcroft and Mermin, 2007). Due to the periodic ordering and connection, a vibration of an atom/ion in the crystal is distributed to the whole crystal and includes all other atoms/ions leading to waves which traverse through the lattice. Therefore, not the vibration of single particles but the movements of all with each other coupled particles in the lattice have to be treated for a description of the lattice energy.

In a crystal of N bases with p atoms per base, $3Np$ different possible modes of vibration of the lattice exist. The modes are discriminated by N different wave vectors $\mathbf{k}$ (of the respective reciprocal lattice) each with a polarization[3] $j = 1, 2, ...3p$ (Ashcroft and Mermin, 2007). This influences of course the potential that is seen by an arbitrary particle in the lattice and makes it much more difficult to describe, much less to solve, the exact Hamiltonian (the sum of the overall kinetic and potential energy) for a crystal. Therefore, the contribution to the overall potential energy of a crystal U from pairs of atoms having a potential Φ (e.g. like the one which is described in Fig. 2.1) is approximated by Taylor series in three dimensions for displacement vectors $\mathbf{u}$ of the particles from their equilibrium position vectors $\mathbf{R}$ small compared to their related distance:

$$U = \frac{1}{2}\sum_{\mathbf{RR'}} \Phi(\mathbf{a}+\mathbf{r}) \tag{2.1}$$

$$= \frac{1}{2}\sum_{\mathbf{RR'}} \Phi(\mathbf{a}) + \frac{1}{2}\sum_{\mathbf{RR'}} (\mathbf{r}\cdot\nabla\Phi(\mathbf{a})) + \frac{1}{4}\sum_{\mathbf{RR'}} (\mathbf{r}\cdot\nabla)^2\Phi(\mathbf{a}) + O(r^3), \tag{2.2}$$

with $\mathbf{a} = \mathbf{R} - \mathbf{R'}$ and $\mathbf{r} = \mathbf{u}(\mathbf{R}) - \mathbf{u}(\mathbf{R'})$. Because there is no resulting force on the

[3]The term "polarization" in this context should not be mistaken with the optical polarization. Later on, we will refer to j as branch

particles in their equilibrium positions, the linear term must be zero whereas the first term represents the energy of the particles in the equilibrium positions. The third one is the harmonic term U^{harm} that gives the mean contribution to the movement of the particle in the given approximation. The last term can be seen as perturbation of the harmonic potential and represents the anharmonic contributions. With the assumption that only the relative distances $(\mathbf{R} - \mathbf{R}')$ account, U^{harm} takes a form similar to Hooks law.

$$U^{\text{harm}} = \frac{1}{2} \sum_{\mathbf{R}\mathbf{R}'\mu\nu} K_{\mu\nu}(\mathbf{R} - \mathbf{R}') u_\mu(\mathbf{R}) u_\nu(\mathbf{R}'), \qquad K_{\mu\nu}(\mathbf{R} - \mathbf{R}') = \frac{\partial^2 U^{\text{harm}}}{\partial u_\mu(\mathbf{R}) \partial u_\nu(\mathbf{R}')}|_{\mathbf{u}=0}. \tag{2.3}$$

where μ, ν represent the space coordinates and $K_{\mu\nu}(\mathbf{R} - \mathbf{R}')$ are the force constants for each pair $\mathbf{R}, \mathbf{R}'$ (Escamilla-Reyes and Haro-Poniatowski, 2005; Ashcroft and Mermin, 2007).

2.1.2. Lattice vibrations

In the most simple case of a linear chain of bonded particles each with a mass M where only nearest neighbors can interact and with a potential of the form of (2.3), the equation of motion for a single particle is

$$M\ddot{u}_n = -\frac{\partial U^{\text{harm}}}{\partial u_n} = -K(2u_n - u_{n-1} - u_{n+1}). \tag{2.4}$$

u_n is the displacement of the nth particle from the equilibrium position. The distance to the nearest neighbor is a and the lattice vector $\mathbf{R}$ is in our case given by na for the nth particle, with n being an integer (see Fig. 2.2). u_n is counted twice since there are two bonds to the $(n-1)$th and $(n+1)$th particle. These are the equations of motion for particles which are bonded to each other by equal springs with the force constant K (Hooks law). The solution is a wave that propagates along the chain: $u_n(t) \sim e^{i(kna - \omega t)}$, where ka is the phase difference between neighboring particles and k is the wave number. The frequency ω of this wave, follows a *dispersion relation* given by

$$\omega = 2\sqrt{\frac{K}{M}} |\sin(\frac{ka}{2})|. \tag{2.5}$$

Is there a difference in k in the manifold of $2\pi/a$ (multiple of the vectors of the reciprocal lattice) then the appearing waves are physical equivalent which means that the motion of the particles can be expressed by the one or the other wave. Therefore, it is sufficient to describe the dispersion relation in the interval $[0, \frac{2\pi}{a}]$ or in the interval $[-\frac{\pi}{a}, \frac{\pi}{a}]$ (the first Brillouin zone) as it is commonly used (see Fig. 2.3).

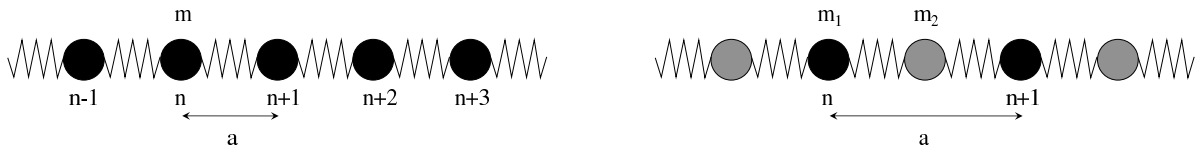

(a) (b)

Figure 2.2.: The linear chain with one atom (a) and two atoms (b).

By using a chain with a base of two different atoms, between particles 1 having the mass M_1 and particles 2 having the mass M_2[4] has to be distinguished. The equations of motion can again be solved by assuming waves as solutions with $u_n^1, u_n^2 = A, Be^{i(kna-\omega t)}$ resulting in a system of equations which can be solved to

$$\omega_{\pm}^2 = \left(\frac{K}{M_1} + \frac{K}{M_2}\right) \pm \sqrt{\left(\frac{K}{M_1}\right)^2 + \left(\frac{K}{M_2}\right)^2 + 2\frac{K^2}{M_1 M_2}\cos(ka)}. \tag{2.6}$$

Obviously, there are now two different branches for ω. ω_- represents oscillations of the bases, whereas within one base the particles are in the same phase, similar to acoustic waves. Therefore, it is called the acoustic branch of vibration. ω_+ describes the contrary vibration of the two particles within the base. It is called the optical branch of vibration. by taking also the other two space dimensions into account, also movements perpendicular to the k-axis (direction of the wave) can appear. Therefore, there are in total six branches in which the modes have to be discriminated: one *longitudinal acoustic* (LA) and one *longitudinal optical* branch (these are the branches which appeared already as solutions of the one dimensional linear chain) and additionally two *transverse acoustical* (TA) and two *transverse optical* (TO) branches.

By changing to a three-dimensional lattice with N equal particles and leaving the nearest neighbor approximation, the principle equations of motion are the same but it becomes necessary now to sum over all particles and directions (Ashcroft and Mermin, 2007)

$$M\ddot{u}_\mu(\mathbf{R}) = -\frac{\partial U^{\text{harm}}}{\partial u_\mu(\mathbf{R})} = -\sum_{\mathbf{R}'\nu} K_{\mu\nu}(\mathbf{R}-\mathbf{R}')u_\nu(\mathbf{R}'). \tag{2.7}$$

The solutions are of the form

$$\mathbf{u}(\mathbf{R}, t) = \mathbf{e}e^{i(\mathbf{kR}-\omega t)} \tag{2.8}$$

where $\mathbf{e}$ is the so called polarization vector of the normal mode. In such a crystal again three

[4]The same conclusions for this case can be achieved also by assuming equal masses but different K.

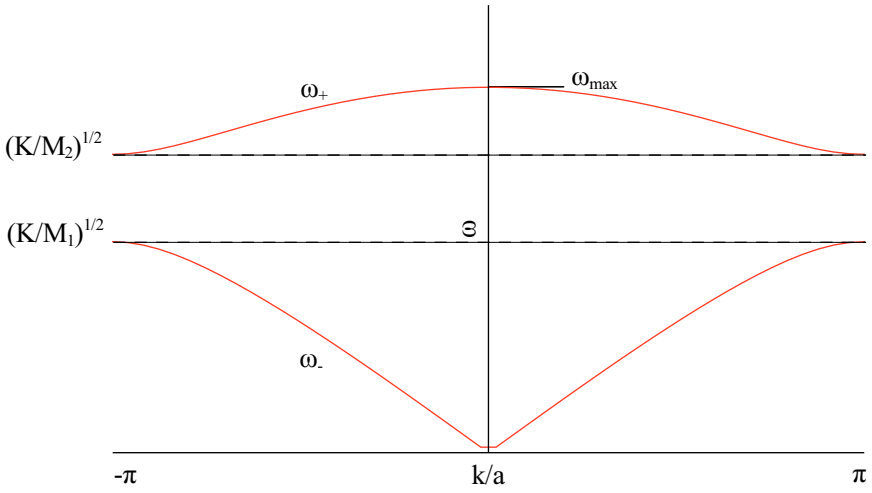

Figure 2.3.: Dispersion curve of a linear chain with two atoms. ω_+ indicates the optical branch, ω_- the acoustic branch. In the limit of equal masses, both branches converge to $\sqrt{\frac{2K}{M}}$ and form two dispersion curves of a linear chain with a particle distance of $\frac{a}{2}$ shifted by π/a.

acoustic branches can be found (2 *TA* and 1 *LA*) but no optical branch. If our crystal gets a base of p particles then (2.8) becomes for the ith particle in the jth branch:

$$\mathbf{u}_j^i(\mathbf{R}, t) = Re[\mathbf{e}_j^i(\mathbf{k}) e^{i(\mathbf{kR} - \omega_j(\mathbf{k})t)}]. \tag{2.9}$$

Now, the polarization vectors are in general complex and fulfill the general orthogonalization relation: $\sum_{i=1}^{p} \mathbf{e}_j^{i*}(\mathbf{k}) \mathbf{e}_{j'}^i(\mathbf{k}) M_i = \delta_{jj'}$. In such a crystal again three acoustic branches but now $(3p - 3)$ optical branches are present.

2.1.3. Quantum mechanical view on the energy of bonds

In quantum mechanics, a particle trapped in a potential can only have discrete energy states $(n = 0, 1, 2, ...)$. In a harmonic potential the energy states of a certain vibration (or mode) have equal distance to each other and an infinite number of states exist. n is the degree of the excitation of a mode but due to the similarities with photons it is rather said that there are n so called *phonons* in the respective mode. In contrast, the anharmonic potential has only a finite number of states (or phonons) per mode and the energetic distance to the next higher state is decreasing (that is why it is called anharmonic). However, considering only small displacements from the equilibrium position, a harmonic potential gives a quite good approximation to an anharmonic potential. Therefore, in a harmonic approximation the overall energy density ϕ of a crystal can be determined with the aid of the eigenstates of a harmonic oscillator which represent the energies of the modes. According Ashcroft and

Mermin (2007), ϕ is therefore given as

$$\begin{aligned}\phi &= \phi^{\mathrm{eq}} + \frac{1}{2V}\sum_{\mathbf{k}j}\hbar\omega_j(\mathbf{k}) + \frac{1}{V}\sum_{\mathbf{k}j}\hbar\omega_j(\mathbf{k})n_j(\mathbf{k}),\\ n_j(\mathbf{k}) &= \frac{1}{e^{\beta\hbar\omega_j(\mathbf{k})}-1}.\end{aligned} \tag{2.10}$$

ϕ^{eq} is the equilibrium energy density, the second therm describes the energy of the modes at 0 K and the third therm specifies the contribution of phonons for $T > 0\,\mathrm{K}$, with $n_j(\mathbf{k})$ being the mean number of phonons at a given temperature T. $n_j(\mathbf{k})$ follows the Bose-Einstein-Distribution[5].

2.2. The influence of the temperature on anharmonic potentials

The calculated expression for the energy density of a crystal has been derived with the assumption of a harmonic potential. But as mentioned above, in real crystals the potential is anharmonic which must be taken into account by calculating the energy density. Unfortunately, with anharmonic terms it is almost impossible to get such a relatively simple description of ϕ as given above. But under the assumption that the anharmonic effects are only small, it is possible to take the results of the harmonic approximation first and to add the effects of an anharmonic potential afterwards. This process is called a *quasi harmonic approximation*.

2.2.1. The mode Grüneisen parameter

From Eq. (2.10), the inner energy of a crystal can be calculated via $U = V\phi$. From the inner energy again, the pressure P can be determined[6] to

$$P = -\frac{\partial}{\partial V}\left(U^{\mathrm{eq}} + \frac{1}{2}\sum_{\mathbf{k}j}\hbar\omega_j(\mathbf{k})\right) + \sum_{\mathbf{k}j}\left(-\frac{1}{\partial V}(\hbar\omega_j(\mathbf{k}))\right)\frac{1}{e^{\beta\hbar\omega_j(\mathbf{k})}-1}. \tag{2.11}$$

To get Eq. (2.11), only the harmonic approximation has been used. However, the second and the third term in Eq. (2.11) are non-zero only for frequencies with an explicit volume dependence but in a pure harmonic potential, the frequencies are constant. Also, since

[5] Phonons are Bosons.

[6] With the aid of $P = -\left(\frac{\partial F}{\partial V}\right)_T$ where F is the Helmholtz free energy, V the volume, and T the equilibrium temperature

a temperature dependent change of the pressure is thermodynamically coupled with the temperature dependent change of the volume in a crystal[7], thermal expansion cannot be explained by a harmonic approximation.

At this point, the quasi harmonic approximation can be taken into account by assuming a volume dependence of the mode frequencies. Eduard Grüneisen determined the temperature derivative of the mode frequencies to (Grüneisen, 1912)

$$\begin{aligned} \frac{1}{\omega_j(\mathbf{k})}\frac{\partial\omega_j(\mathbf{k})}{\partial T} &= -g_{\mathbf{k}j}\frac{1}{V}\frac{\partial V}{\partial T} \quad \text{, where} \\ g_{\mathbf{k}j} &= -\frac{\partial \ln(\omega_j(\mathbf{k}))}{\partial \ln V}. \end{aligned} \tag{2.12}$$

The parameter $g_{\mathbf{k}j}$ gives the volume dependence of each mode and is named *mode Grüneisen* parameter. The thermal expansion α can be expressed thermodynamically with

$$\alpha = \frac{1}{3V}\left(\frac{\partial V}{\partial T}\right)_P. \tag{2.13}$$

Assuming that $g_{\mathbf{k}j}$ is not depending on the temperature and the volume[8] (Grüneisen, 1912), V can be determined to

$$V = V_0\left(\frac{\omega_j(\mathbf{k})}{\omega_0}\right)^{-1/g_{\mathbf{k}j}}, \tag{2.14}$$

at which V_0 and ω_0 are constant. Eq. (2.14) leads, inserted into Eq. (2.13), to an expression of the temperature dependent mode frequency:

$$\omega_j^{\exp}(\mathbf{k},T) = \omega_j(\mathbf{k},0)\cdot e^{-3\int_0^T g_{\mathbf{k}j}\alpha dT'}, \tag{2.15}$$

where $\omega_j^{\exp}(\mathbf{k},T)$ is the mode frequency at temperature T and $\omega_j(\mathbf{k},0)$ is the mode frequency at 0 K that should equal the phonon frequency in the harmonic approximation. It is reasonable to consider only small values (< 1) for the integral since the expected values of $\omega_j^{\exp}(\mathbf{k},T)$ are in the same magnitude as $\omega_j(\mathbf{k},0)$ (Jasperse et al., 1966). Therefore, it is possible to write

$$\Delta\omega_j^{\exp}(\mathbf{k},T) = \omega_j^{\exp}(\mathbf{k},T) - \omega_j(\mathbf{k},0) = \omega_j(\mathbf{k},0)\int_0^T g_{\mathbf{k}j}\alpha dT'. \tag{2.16}$$

[7] $(\partial V/\partial T)_P \sim -(\partial P/\partial T)_V$ (Ashcroft and Mermin, 2007)

[8] Although a temperature dependence of $g_{\mathbf{k}j}$ can generally not be excluded, it should actually be rather small so that assuming $g_{\mathbf{k}j}$ to be a constant seems to be reasonable.

Here, $\Delta\omega_j^{\exp}(\mathbf{k}, T)$ is the frequency shift that would arise only because of the thermal expansion of the crystal. $g_{\mathbf{k}j}$ mostly takes values between 0 and 2 (Gervais and Piriou, 1975) but several models exist to give an estimation of the $g_{\mathbf{k}j}$ values (e.g. Jasperse et al. (1966) present such a model). However, the mode Grüneisen parameter can also be taken directly from Laser pulse measurements.

The estimation of the thermal expansion α has been done in detail by Debernardi and Cardona (1996). It can be shown that in the low temperature limt $\alpha \sim T^3$ whereas in the high temperature limit[9] it is going to be a constant. For intermediate temperatures a linear approximation with the temperature can be done (Fiquet et al., 1999).

2.2.2. Phonon-phonon interaction and the phonon self energy

From the previous subsection the connection between the thermal expansion and the related shift of the mode frequencies of atoms in an anharmonic crystal has been obtained. The mode Grüneisen parameter gives a relatively simple description of the dependence of the mode frequencies on the temperature without knowing any detail of the microscopic properties of the crystal. Within the problem of the thermal expansion this is still reasonable hence the thermal expansion is a measurable macroscopic effect. However, if the Hamiltonian (the sum of kinetic and potential energies) of an anharmonic crystal is analyzed directly, effects of mode coupling will be found which do not appear in a harmonic approximation and are not measurable on a macroscopic scale but influence the frequencies of the modes and give them a finite lifetime (Maradudin and Fein, 1962).

Following Escamilla-Reyes and Haro-Poniatowski (2005); Maradudin and Fein (1962); Ipatova et al. (1967), the Hamiltonian of an anharmonic crystal can be written as

$$\begin{aligned} H = &\sum_{\mathbf{R}\mu} \frac{P_\mu^2(\mathbf{R})}{2M} + \frac{1}{2} \sum_{\mathbf{R}\mathbf{R}'\mu\nu} K_{\mu\nu}(\mathbf{R}, \mathbf{R}') u_\mu(\mathbf{R}) u_\nu(\mathbf{R}') \\ &+ \frac{1}{6} \sum_{\mathbf{R}\mathbf{R}'\mathbf{R}''\mu\nu\xi} K_{\mu\nu\xi}(\mathbf{R}, \mathbf{R}', \mathbf{R}'') u_\mu(\mathbf{R}) u_\nu(\mathbf{R}') u_\xi(\mathbf{R}'') \\ &+ \frac{1}{24} \sum_{\mathbf{R}\mathbf{R}'\mathbf{R}''\mathbf{R}'''\mu\nu\xi\chi} K_{\mu\nu\xi\chi}(\mathbf{R}, \mathbf{R}', \mathbf{R}'', \mathbf{R}''') u_\mu(\mathbf{R}) u_\nu(\mathbf{R}') u_\xi(\mathbf{R}'') u_\chi(\mathbf{R}''') \\ &+ \dots \end{aligned} \tag{2.17}$$

Here, $\mathbf{P}(\mathbf{R})$ is the momentum of the respective particle and the $K_{\mu\nu}$, $K_{\mu\nu\xi}$, $K_{\mu\nu\xi\chi}$ are the force constants in second, third and fourth order of the given approximation. μ, ν, ξ, and χ represent the three spatial dimensions and M is the reduced mass of the atoms/ions in the

[9] Here, high temperature means that $T \gg \Theta_D$ with Θ_D as the *Debye*-temperature, above it all modes are excited (Ashcroft and Mermin, 2007).

crystal. In quantum mechanics, it is possible to make a normal coordinate transformation of the $\mathbf{u}(\mathbf{R})$ and the $\mathbf{P}(\mathbf{R})$ with the aid of phonon creation and annihilation operators ($a^\dagger_{-\mathbf{k}j}$ and $a_{\mathbf{k}j}$ for the respective mode $(\mathbf{k}j)$). Let $M_\mathbf{R}$ be the mass of the particle at the position $\mathbf{R}$, then it is (Maradudin and Fein, 1962)

$$\mathbf{u}(\mathbf{R}) = \left(\frac{\hbar}{2NM_\mathbf{R}}\right)^{1/2} \sum_{\mathbf{k}j} \frac{\mathbf{e}_j(\mathbf{k})}{[\omega_j(\mathbf{k})]^{1/2}} e^{2\pi i \mathbf{k}\cdot\mathbf{R}} \cdot (a^\dagger_{-\mathbf{k}j} + a_{\mathbf{k}j}) \tag{2.18}$$

$$\mathbf{P}(\mathbf{R}) = -i \left(\frac{\hbar M_\mathbf{R}}{2N}\right)^{1/2} \sum_{\mathbf{k}j} \mathbf{e}_j(\mathbf{k}) [\omega_j(\mathbf{k})]^{1/2} e^{2\pi i \mathbf{k}\cdot\mathbf{R}} \cdot (a_{\mathbf{k}j} - a^\dagger_{-\mathbf{k}j}), \tag{2.19}$$

where $\mathbf{e}_j(\mathbf{k})$ is the polarization vector for the mode $(\mathbf{k}j)$. With this transformation and the further simplification that $a^\dagger_{-\mathbf{k}j} + a_{\mathbf{k}j} = A_{\mathbf{k}j}$, Eq. (2.17) becomes

$$H = \frac{1}{2}\sum_{\mathbf{k}j} \hbar\omega_j(\mathbf{k}) + \sum_{\mathbf{k}j} \hbar\omega_j(\mathbf{k}) a^\dagger_{\mathbf{k}j} a_{\mathbf{k}j} + \sum_{n=3}^{\infty} \sum_{\mathbf{k}_1 j_1,\ldots,\mathbf{k}_n j_n} V^{(n)}(\mathbf{k}_1 j_1, \ldots, \mathbf{k}_n j_n) A_{\mathbf{k}_1 j_1} \ldots A_{\mathbf{k}_n j_n}. \tag{2.20}$$

The $V^{(n)}$ coefficients are the Fourier transforms of the nth order atomic force constants and are completely symmetric in the indices $(\mathbf{k}_i j_i)$, $i = 1, \ldots, n$ at which $(\mathbf{k}j)$ is also still an index (Maradudin and Fein, 1962; Tripathi and Pathak, 1973).

To get knowledge for the influence of the interactions of phonons on the mode frequencies, some quantum statistics and quantum field theory have to be applied, respectively. According to Cowley (1963), the spectral density is directly related to a thermodynamic *Green's* function. The thermodynamical Green's function gives a statistical description of the time evolution of a variable for an ensemble in a thermal equilibrium. So it is possible to calculate how long a given property of a system persists until it is averaged by microscopic motion and interaction with its surrounding environment. Therefore, the investigation of the mode frequencies in a perturbed crystal system has to start with the thermodynamical (one phonon) Green's function that is defined as (Tripathi and Pathak, 1973)

$$G_{\mathbf{k}j\mathbf{k}'j'}(u) = \langle T A_{\mathbf{k}j}(u) A^\dagger_{\mathbf{k}'j'}(0) \rangle \tag{2.21}$$

with T here as the so called *time-ordering* operator and $A_{\mathbf{k}j}(u)$ is written in the *Heisenberg* representation[10]. With an anharmonic Hamiltonian as given in Eq. (2.17), the thermody-

[10] $A(u) = e^{uH} A(0) e^{-uH}$

namic Green's function can be written as Cowley (1963)

$$G_{\mathbf{k}j\mathbf{k}'j'}(u) = \langle T\tilde{A}_{\mathbf{k}j}(u)\tilde{A}^{\dagger}_{\mathbf{k}'j'}(0) \sum_{n=0}^{\infty}\frac{(-1)^n}{n!}\int_0^{\beta}\dots\int_0^{\beta}\tilde{H}^{\mathrm{anharm}}(\beta_1)\dots\tilde{H}^{\mathrm{anharm}}(\beta_n)d\beta_1\dots d\beta_n\rangle. \tag{2.22}$$

The 'tilde' on top of the operators indicates the interaction representation[11]. Let $\omega_l = 2\pi l/\beta\hbar$ (l an integer), then its Fourier coefficients are defined as

$$G_{\mathbf{k}j\mathbf{k}'j'}(l) = \frac{1}{\beta}\int_0^{\beta} G_{\mathbf{k}j\mathbf{k}'j'}(u)e^{i\hbar\omega_l u}du. \tag{2.23}$$

$G_{\mathbf{k}j\mathbf{k}'j'}(l)$ is called the *phonon propagator*. It can be evaluated by diagrammatic perturbation theory, which sums up all the contributions of phonon creation and destruction processes whereas only those contributions are to be considered which connect creation and destruction. The contributions can be presented in Feynman diagrams in which each free phonon with $(\mathbf{k}j)$ is entering and a free phonon with $(\mathbf{k}'j')$ is leaving, each represented by the *free phonon propagator* $G^0_{\mathbf{k}j}(l)$ that is defined as (Maradudin and Fein, 1962; Cowley, 1963; Tripathi and Pathak, 1973)

$$G^0_{\mathbf{k}j}(l) = \frac{2\omega_j(\mathbf{k})}{\beta\hbar}\frac{1}{\omega_l^2 + \omega_j^2(\mathbf{k})}. \tag{2.24}$$

The phonon propagator according to Maradudin and Fein (1962); Tripathi and Pathak (1973) can be written as

$$G_{\mathbf{k}j\mathbf{k}'j'}(l) = G^0_{\mathbf{k}j}(l)\delta_{\mathbf{k}j\mathbf{k}'j'} + G^0_{\mathbf{k}j}(l)\sum_{\mathbf{k}''j''} S_{\mathbf{k}j\mathbf{k}''j''}(l)G_{\mathbf{k}''j''\mathbf{k}'j'}(l). \tag{2.25}$$

Here $S_{\mathbf{k}j\mathbf{k}'j'}$ denote the so called *phonon self energy* that is the sum of the contributions of all Feynman diagrams which cannot be separated by cutting a free phonon line (*proper* diagrams, Maradudin and Fein (1962)). Maradudin and Fein (1962) pointed out that the phonon propagator, and therefore also the phonon self energy, is diagonal in $\mathbf{k}$ and $\mathbf{k}'$ and can be rewritten as $G_{\mathbf{k}jj'}(l)$ which it is non-vanishing only when $(\mathbf{k}-\mathbf{k}')$ equals a translation vector of the reciprocal lattice. The same holds true for the phonon self energy, now written as $S_{\mathbf{k}jj'}(l)$ which can be additionally split off into a diagonal and a non-diagonal part by

$$S_{\mathbf{k}jj'}(l) = \delta_{jj'}S_{\mathbf{k}j}(l) + S^N_{\mathbf{k}jj'}(l) \tag{2.26}$$

[11] $\tilde{A}(u) = e^{uH^{\mathrm{harm}}}A(0)e^{-uH^{\mathrm{harm}}}$.

with $S^N_{\mathbf{k}jj}(l) = 0$ (Maradudin and Fein, 1962).

Between an incoming and an outgoing phonon, several creation and destruction processes can happen in a diagram. In principle, the number of creation/destruction pairs which appear in one diagram can be seen as the order of the perturbation theory. To the first order perturbation theory and to the fourth anharmonic Hamiltonian (represented by $V^{(4)}$) only a contribution due to a four-phonon process at one vertex exist, while to the second order, a three-phonon process and a four-phonon process each with two vertexes exist. An additional ordering can be introduced by the approximation of *van Hove* for the anharmonic Hamiltonian. He pointed out that the expectation value of the nth order potential energy term in a crystal Hamiltonian is of the order of magnitude of $\hbar\omega(a/r_0)^{n-2}$ (Maradudin and Fein, 1962). a is a kind of mean atomic displacement and r_0 denotes the nearest neighbor separation. Writing (a/r_0) as λ, the anharmonic Hamiltonian can be written schematically to $H^{\text{anharm}} = \lambda V^{(3)} + \lambda^2 V^{(4)} + \ldots$. Maradudin and Fein (1962) limited their calculations to the order of λ^2 which means that they took into account only the four-phonon process in first order and the three-phonon process in second order perturbation theory.

There are several rules how to sum up all the contributions of the phonon-phonon interactions to $S_{\mathbf{k}jj'}(l)$ (see e.g. Cowley (1963); Maradudin and Fein (1962)). Because they are not relevant for the following conclusions, they shall not be given here. The individual contributions can be quite complex even for relatively simple inter-atomic potentials but a good collection of them up to the sixth anharmonic Hamiltonian and to the second order perturbation theory is given in Tripathi and Pathak (1973). The principal conclusions which arise from the derivations can be summarized as follows:

- By changing the discrete formulation that has been used so far for the phonon self energy and the phonon propagator to a continuous variable ($i\omega_l \to \omega$) it can be found that

$$\lim_{\delta\to 0+} -\frac{1}{\beta\hbar} S_{\mathbf{k}j}(\omega \pm i\delta) = \Delta\omega_j(\mathbf{k};\omega) \mp i\Gamma(\mathbf{k}j;\omega), \tag{2.27}$$

  where $\Delta\omega_j(\mathbf{k};\omega)$ and $\Gamma(\mathbf{k}j;\omega)$ are a frequency shift and a (frequency dependent) damping function[12] of the mode $(\mathbf{k}j)$, respectively. They are both related to the phonon-phonon interactions and therefore to the anharmonic contributions.

- $\Delta\omega_j(\mathbf{k};\omega)$ and $\Gamma(\mathbf{k}j;\omega)$ are temperature dependent. This is due to the fact that the contributions to the phonon self energy contain sums over free phonon propagators which converge to $(2n_j(\mathbf{k})+1)$, whereas n means the known Bose-Einstein distribution. To the order of λ^2, it has been shown that in the high-temperature limit ($k_BT \gg \hbar\omega_j(\mathbf{k})$) both are proportional to T (Maradudin and Fein, 1962; Cowley, 1963). By

[12]The damping function is actually the inverse lifetime of a phonon.

taking higher orders of λ into account, the proportionality is even quadratic in T (Ipatova et al., 1967). For low temperatures, both contributions would not disappear but tend to reach a constant value at 0 K.

According to the above expressions for the principal temperature dependence of the mode frequencies, the frequency shift in a high-temperature limit can be well approximated by a second order polynomial in T. The same holds true for the damping which only appears because of the anharmonic potential and the interaction of phonons[13].

2.3. Interaction of electromagnetic fields with solids

There are mainly three kinds of mechanisms in solids which can lead to an interaction with electromagnetic radiation: excitations of electrons among the (electron-)bands, nuclear excitations[14], and lattice vibrations. For a description of the electronic excitation mostly the models of *Drude* and *Sommerfeld* are applied. Both models are classical models and not as general as the *band*-model but contrary to it, mathematical statements about the energy dependence of the interaction with electromagnetic radiation can be given precisely (this is almost impossible within the band model).

Generally, the ability of electromagnetic radiation to interact with solids and to produce lattice vibrations is based on the change of dipole moments or polarizabilities of molecules or groups of atoms within the solid. The latter is taking place by inelastic scattering of light on the lattice and is important for the *Raman*-spectroscopy. Since in this work measurements done only with IR spectroscopy are presented, the Raman-effect will not be discussed. The vibration frequencies of atoms/ions in a lattice are typically in the frequency range of IR light and therefore, IR light is able to excite lattice vibrations directly. The only condition for a direct excitation of a lattice vibration with light is an already existing or induced dipole moment within the lattice that changes with the incident electric field.

2.3.1. Classical description of external excitations

Classically (and to first approximation), the model of a *Lorentz*-oscillator is taken for a description of the excitation of a lattice vibration with IR light. This model is starting formally with electrically charged particles that are bonded in a harmonic potential, similar to the assumptions which have been made in section 2.1.3 but now with the further simplification

[13] Even at 0 K there will be always a motion of the atoms due to the Heisenberg uncertainty principle. Therefore, the atoms will always 'feel' the anharmonic potential thus the damping never drops to 0.
[14] Since for the energies which are treated here they do not play a role, they will also not be described.

that each particle has its own spring and vibrates independently[15] from the other particles. If x is the displacement of the particle relative to its equilibrium position, E_{local} is the exciting local field in the direction of x, K the force constant of the spring, m the mass and q the electric charge of the particle, then the equation of motion in one dimension can be written as

$$m\ddot{x} + b\dot{x} + Kx = qE_{\text{local}}. \tag{2.28}$$

In contrast to the assumptions from section 2.1.3, now the damping is taken into account. It should be noted that this kind of damping (proportional to $\dot{x}$) is assumed to be originated by dissipative forces. If the applied field is oscillating with the frequency ω, the particle tries to follow the field and the solutions for x should be vibrations of the form $x = x_0 e^{-i\omega t}$:

$$x = \frac{(q/m)E_{\text{local}}}{\omega_0^2 - \omega^2 - i\gamma\omega}, \tag{2.29}$$

with $\omega_0^2 = K/m$ and $\gamma = b/m$. Obviously, ω_0 is the eigenstate of the particle-spring system and represents its vibration mode. It is interesting to note that due to the damping, the amplitude of displacement is in general complex. If a charged particle in an equilibrium position is displaced by an electric field, a dipole moment p_{ind} is induced that is proportional to x. Assuming now that there is a certain density n of the same oscillators, the overall polarization density P is

$$P = np_{\text{ind}} = nqx = \frac{\omega_P^2}{\omega_0^2 - \omega^2 - i\gamma\omega}\varepsilon_0 E_{\text{local}} = \alpha_{\text{pol}} E_{\text{local}}, \qquad \omega_P = \sqrt{\frac{nq^2}{m\epsilon_0}}. \tag{2.30}$$

ω_P is the plasma frequency, ε_0 the vacuum permittivity ($\approx 8.854 \times 10^{-12}\, As/Vm$), and α_{pol} is molecular polarizability of the charged particles. Since P is linear in x and E_{local}, the results are relatively easy expandable to three dimensions ($x \to \mathbf{x}$, $E_{\text{local}} \to \mathbf{E}_{local}, \dots$), whereas it should be mentioned that α_{pol} is in general a tensor of the second order. However, the local electric field $\mathbf{E}_{local}$ cannot be compared with the macroscopic electric field $\mathbf{E}$ which is connected to the polarization $\mathbf{P}$ via

$$\mathbf{P} = \chi\varepsilon_0\mathbf{E}, \tag{2.31}$$

with $\chi = \varepsilon/\varepsilon_0 - 1 = \epsilon - 1$ as the dielectric susceptibility, ε as the overall and ϵ as the relative permittivity in a medium, respectively (ϵ will be written without limiting the universality

[15] This can be assumed for lattice waves with small $\mathbf{k}$ values (long wavelengths) as they are excited by e.g. IR light (see further text).

as permittivity now). The connection between the Eqs. (2.30) and (2.31) is given by the *Clausius-Mossotti* relation

$$\frac{\chi}{\chi+3} = \frac{\epsilon-1}{\epsilon+2} = \frac{n\alpha_{\text{pol}}}{3\varepsilon_0}. \tag{2.32}$$

Combining Eqs. (2.32) and (2.30), a description of the (complex) permittivity to

$$\epsilon = \epsilon' + i\epsilon'' = 1 + \frac{\omega_P^2}{\omega_1^2 - \omega^2 - i\gamma\omega} \tag{2.33}$$

can be determined with $\omega_1 = \sqrt{\omega_0^2 - \omega_P^2/3}$ as the displaced resonance frequency that results from the deviation of the local electric field from the macroscopic one. The complexity of ϵ arises from the complexity of the displacement of the charged particles and is therefore also due to the damping. Since $\epsilon''(\omega)$ yet has local maximums at $\omega = \omega_1$, it is also a good indicator for the resonant interaction between light and matter (absorption). But in practice it is more convenient to use the complex refractive index m to express absorption and propagation of light in a medium:

$$m = n + ik = c\sqrt{\varepsilon\mu}. \tag{2.34}$$

c is the speed of light in vacuum ($= 299,792,458\, m/s$) and μ represents the magnetic permeability[16] of the medium. n and k are called the optical constants of a medium because both are directly related to the wave vector $\mathbf{k}$ of a propagating light wave inside the medium via

$$|\mathbf{k}| = (k' + ik'') = \frac{\omega}{c}m. \tag{2.35}$$

Therefore, they determine the relation between incoming electromagnetic radiation and the properties of the medium/material in which the radiation propagates. n gives the relation between the speed of light in vacuum and the phase velocity of the light wave whereas k is bonded to the absolute value of the *Pointing*-vector[17] $\mathbf{S}$ of the light wave realizing the energy loss in a medium. Therefore, k is usually interpreted as an absorption index. The bond between ϵ and m is given by the equations

$$\epsilon' = n^2 - k^2 \tag{2.36}$$

$$\epsilon'' = 2nk. \tag{2.37}$$

[16] In this work only materials for which the magnetic properties are insignificant will be discussed. Therefore, μ will be set to be 1 in all of the treatments.

[17] If $\mathbf{E}$ and $\mathbf{H}$ are the time and space dependent electric and magnetic field of a light wave, the Pointing-vector is then determined by $1/2 \times Re\,(\mathbf{E} \times \mathbf{H})$.

In a real solid, besides the particle vibrations there are also possible excitations at higher frequencies (like multiphonon interactions; see further sections). In order to account for these additional influences on ϵ, ϵ_∞ is introduced as value for ϵ for frequencies very high compared to those of the one-phonon vibrations.

Usually in crystals, a lot of different vibration modes exist. Especially for the $\mathbf{k}$-values of the lattice waves, the number of contributions is in practice uncountable (number of unit cells in a real crystal $\sim 10^{23}$). Fortunately, the excitation of lattice vibrations with IR light is limited to very low $\mathbf{k}$-values since the wavelength of IR light is of the order of $1-500\,\mu$m which is by far bigger than the interatomic distance in a crystal. Therefore, the possible vibration modes can be limited to all $\mathbf{k}j$ for which $\mathbf{k} \approx 0$. Furthermore, the excitation of acoustic vibrations can be excluded because they are not associated with dipoles at low $\mathbf{k}$ values ($\omega_A \sim |\mathbf{k}|$) so that only optical modes will be excited by IR light. Since now coupled oscillators in a (at least approximated) real crystal are treated, the usage of ω_{Pj} as the plasma frequency for the mode j is not valid (especially due to additional influences from electronic excitations at shorter wavelengths) but can be expressed in terms of LO and TO frequencies.

Assuming only one excitable mode and small values of the damping term, then from Eq. (2.32), it is possible to write ω_{TO} for ω_1. From Eq. (2.33) it can be further shown that $(\omega_{\text{zero}}^2 - \omega_{TO}^2)\epsilon_\infty = \omega_P^2$, with ω_{zero} being the frequency where $\epsilon = 0$. The Maxwell equations show that the zeros of the permittivity are associated with the frequencies of the longitudinal vibrations whereas the poles are given at frequencies of the transverse vibrations of the particles within a lattice. Within the given constraints, it is therefore possible to write $(\omega_{LO}^2 - \omega_{TO}^2)\epsilon_\infty = \omega_{Pj}^2$, which can be further simplified to $\sigma\omega_{TO}^2$ whereas σ means the relative strength (intensity) of the interaction with the IR light around ω_{TO}. ϵ' is negative in the frequency range between ω_{TO} and ω_{LO} which means that the electromagnetic wave cannot propagate through the medium and will be damped exponentially (the wave vector of the radiation becomes imaginary). The strongest damping appears at ω_{TO} because only TO phonons are resonant with a transverse electromagnetic field. For $\omega = \omega_{LO}$, no interaction with the electromagnetic field can be initiated any more because the LO vibrations are non-excitable with transverse electromagnetic radiation. Between these two frequencies, the reflection of the electromagnetic radiation is quite strong (in case of no damping: 100%) because of both a strong absorption index k and a low n (the principal shape of ϵ' and the absorption in a bulk material with a small damping is sketched in Fig. 2.5).

For more than one oscillator in the lattice, each optical branch j contributes to ϵ and although the particular relationship between σ_j, ω_{TOj}, and ω_{LOj} will be much more complex, the simplifications which have been made are in principle still valid. For ϵ, the well known

equation of the Lorentz oscillator model can now be given:

$$\epsilon = \epsilon_\infty + \sum_j \frac{\sigma_j \omega_{TOj}^2}{\omega_{TOj}^2 - \omega^2 - i\gamma_{TOj}\omega}. \tag{2.38}$$

In a first approximation, it is assumed that the mode related damping γ_j is a constant term.

Since crystals are in general anisotropic, ϵ is a diagonal tensor of the second order. The different diagonal elements ϵ_i can be derived each by Eq. (2.38), assuming that in the relative spatial direction linear polarized IR light is exciting an independent set of vibration modes. In relation to the seven different systems of crystals, one can distinguish:

isotropic crystals/solids, $\epsilon_1 = \epsilon_2 = \epsilon_3$. These are the amorphous solids and cubic crystals[18].

uniaxial crystals, $\epsilon_1 = \epsilon_2 \neq \epsilon_3$. Tetragonal, hexagonal, and trigonal crystals. At frequencies for whch the absorption is low, double refraction can appear.

biaxial crystals, $\epsilon_1 \neq \epsilon_2 \neq \epsilon_3$. The orthorhombic, triclinic and monoclinic systems of crystals whereas for the triclinic and monoclinic systems real and imaginary part have different directions.

2.3.2. Quantum mechanical view on external excitations

The notations which have been made so far for the interaction of IR light with crystals are based only on the derivation of the Lorentz-oscillator by a simple assumption of a damped harmonic oscillator. For having a deeper understanding into the whole problem, a look back to section 2.2.2, where the phonon propagator has been introduced, is necessary. Following Cowley (1963), the dielectric susceptibility is represented by the contributions of the changes in the dipole moments and the following creation of phonons situated in a crystal. Those changes can again be written in terms of Feynman diagrams which in the end just have to be summed up. For $\mathbf{k} \sim 0$ and to the order of λ^2 (see section 2.2.2) the first contribution to χ for a crystal that is invariant against inversion in the unit cell gives for ϵ (Gervais and Piriou, 1974)

$$\epsilon = \epsilon_\infty + \frac{4\pi}{v\hbar} \sum_{\mathbf{k},0j} M_{\alpha j} M_{\beta j} \frac{2\omega_j(\mathbf{k};0)}{\omega_j^2(\mathbf{k};0) - \omega^2 + 2\omega_j(\mathbf{k};0)[\Delta\omega_j(\mathbf{k};\omega;T) - i\Gamma(\mathbf{k}j;\omega;T)]}. \tag{2.39}$$

$M_{\alpha j}$ and $M_{\beta j}$ are the dipole moment components in the j optical branch and v is the volume of the crystal. $\Delta\omega_j(\mathbf{k};\omega;T)$ is the frequency shift due to phonon-phonon interaction as

[18] It is interesting to note that also most of the liquids have this property.

given in section 2.2.2 (now, written with an explicit dependence on the temperature) and $\Gamma(\mathbf{k}j;\omega;T)$ is the damping due to phonon annihilation. It is distinguishable that the term in square brackets is the phonon self energy. Eq. (2.39) has the same structure as Eq. (2.38) and both relations are equivalent when (Gervais and Piriou, 1974)

$$\begin{aligned} \omega_{TOj}^2\sigma_j &\equiv \frac{8\pi}{v\hbar}\omega_j(\mathbf{k};0)M_{\alpha s}M_{\beta j} \\ \omega_{TOj}^2 &\equiv \omega_j^2(\mathbf{k};0) + 2\omega_j(\mathbf{k};0)\Delta\omega_j(\mathbf{k};\omega;T) \\ \omega\gamma_{TOj} &\equiv 2\omega_j(\mathbf{k};0)\Gamma(\mathbf{k}j;\omega;T). \end{aligned} \tag{2.40}$$

$\omega_j(\mathbf{k};0)$ is the mode frequency when no phonon-phonon interaction would appear. Again, it should be noted that Eq. (2.39) is only valid for IR light ($\mathbf{k} \approx 0$) and also only by neglecting the additional contributions to χ of the order λ^2 and those of higher orders in λ, respectively. From the relations above, it is obvious that also the damping parameter from Eq. (2.38) carries in general an explicit frequency dependence now.

At this point, it is possible to combine the considerations which have been made regarding the temperature dependence of the vibration frequency of ω_{TOj}. In the form of Eq. (2.40), the temperature dependence of ω_{TOj} is limited to the phonon-phonon interaction. If the thermal expansion is included, $\omega_j(\mathbf{k};0)$ becomes $\omega_j^{\exp}(\mathbf{k};T)$, the frequency of the jth mode left with a dependence on the thermal expansion. Making the substitution $\omega_j(\mathbf{k},0) \rightarrow \omega_j^{\exp}(\mathbf{k};T)$ in Eq. (2.40) and assuming now $\omega_j'(\mathbf{k},0)$ to be the frequency of the jth oscillator at 0 K, Eq. (2.40) becomes

$$\omega_j^2 = \omega_j'(\mathbf{k};0)^2\left(1+\int_0^T g_{\mathbf{k}j}\alpha(T')dT'\right)^2 + 2\omega_j'(\mathbf{k};0)\left(1+\int_0^T g_{\mathbf{k}j}\alpha(T')dT'\right)\Delta\omega_j(\mathbf{k};\omega;T). \tag{2.41}$$

Here, $g_{\mathbf{k}j}$ is the mode Grüneisen parameter and $\alpha(T)$ the thermal expansion coefficient as introduced in section 2.2.1. Assuming $\Delta\omega_j(\mathbf{k};\omega;T)$ to be sufficiently small, Eq. (2.41) can be simplified to

$$\omega_j = \omega_j'(\mathbf{k};0)\left(1+\int_0^T g_{\mathbf{k}j}\alpha(T')dT'\right) + \Delta\omega_j(\mathbf{k};\omega;T). \tag{2.42}$$

2.3.3. The FPSQ model

As mentioned in the previous section, Eqs. (2.38) and (2.39), respectively, are only valid for crystals which have a center of inversion in the unit cell. Actually, all crystals which show a resulting dipole moment in their unit cell, lack such a center of inversion which could make

things much more complex as they already are. But fortunately, for most materials the additional effects which arise due to the polar character of their crystalline state play not an important role in the interaction with IR light. Though, for materials with a strong polar character (e.g. crystals with a distinct ionic bond), the influence of the long wavelength ($\mathbf{k} \approx 0$) longitudinal optic vibration modes (polar longitudinal modes) cannot be neglected any more and more attention to the longitudinal vibrations has to be payed.

As already mentioned, in Eq. (2.38) the ω_{TOj} appear as the poles of the complex permittivity. From the Maxwell equations it is known that in a medium the dielectric displacement field $\mathbf{D}$ is bonded to the electric field $\mathbf{E}$ and the polarization density $\mathbf{P}$ via

$$\mathbf{D} = \varepsilon_0 \mathbf{E} + \mathbf{P} = \varepsilon_0 \epsilon \mathbf{E} \tag{2.43}$$

(here, frequency dependence is assumed for all parameters). Contrary to the permittivity, an inverse permittivity η can be defined via

$$\varepsilon_0 \mathbf{E} = \frac{1}{\epsilon} \mathbf{D} = \eta \mathbf{D}. \tag{2.44}$$

From the previous section it is known that ϵ has zeros at the frequencies of the longitudinal modes which means that at these frequencies η has its poles.

If an investigation of the influence of the longitudinal optic modes is desired, a *factorization* of the expression for ϵ has to be done. Starting with the simple form Eq. (2.38), after multiplying the equation by all resonant denominators (Barker, 1964b) it can be seen that

$$\begin{aligned} \epsilon \prod_j (\omega_{TOj}^2 - \omega^2 - i\omega\gamma_{TOj}) =& \omega_{TO1}^2 \omega_{TO2}^2 \dots \omega_{TOn}^2 (\sigma_1 + \sigma_2 + \dots + \sigma_n + \epsilon_\infty) + \\ & i\omega(\dots) - \omega^2(\dots) - i\omega^3(\dots) + \omega^4(\dots) + \\ & i\omega^5(\dots) - \dots + (-1)^n \omega^{2n} \epsilon_\infty. \end{aligned} \tag{2.45}$$

The coefficients in brackets (denoted only by dots) are mixed terms of σ_j, ω, ϵ_∞ and γ_{TOj}. The right hand side of Eq. (2.45) is a polynomial of order $2n$ where n is the number of modes which can be excited. Therefore, for $\epsilon = 0$ there are $2n$ roots b_i solving the relation. These roots should in general be complex which means that if b_i is a solution so is its negative complex conjugate $-b_i*$ (Barker, 1964b). Now, the mathematical tool of the polynomial factorization can be used. Consider a polynomial of the Nth order with x as the running variable and a_k the kth coefficient. If b_i are the zeros of the polynomial then it is

$$\sum_{k=0}^{N} a_k x^k = a_N \prod_{i=1}^{N} (x - b_i). \tag{2.46}$$

From an investigation of Eq. (2.45) it can be seen that there is indeed a polynomial of the above given form. Therefore, one may write

$$\epsilon \prod_j (\omega_{TOj}^2 - \omega^2 - i\omega\gamma_{TOj}) = (-1)^n \epsilon_\infty \prod_{i=1}^{2n} (\omega - b_i). \tag{2.47}$$

By making use of the complexity of the b_i and the relation $b_i \cdot (-b_i*) = -|b_i|^2$ Eq. (2.47) can be written in the more useful form

$$\epsilon \prod_j (\omega_{TOj}^2 - \omega^2 - i\omega\gamma_{TOj}) = (-1)^n \epsilon_\infty \prod_{i=1}^{n} (\omega^2 - |b_i|^2 + 2i\omega \mathrm{Im}(b_i)). \tag{2.48}$$

According to the works by Gervais and Piriou (1974), Lowndes (1970) and Barker (1964b), a resonance frequency is the absolute value of the complex pole and not its real part. This means that ω_{LOj}^2 can be set as $|b_i|^2$, since the zeros of ϵ are assumed as being the poles of η. Furthermore, it can be shown that the half imaginary part of a complex pole in the inverse permittivity corresponds physically to the damping of the longitudinal mode (Lowndes, 1970). Therefore, the form

$$\epsilon = \epsilon_\infty \prod_j \frac{\omega_{LOj}^2 - \omega^2 - i\omega\gamma_{LOj}}{\omega_{TOj}^2 - \omega^2 - i\omega\gamma_{TOj}} \tag{2.49}$$

is applied. This is the permittivity in its factorized form. There are now four parameters for each mode instead of only three as for the classical Lorentz oscillator, in which the damping parameter of the longitudinal mode has been taken into account only indirectly over the definition of the mode strength (when the poles/zeros of ϵ are assumed as being complex). From now on, both damping parameters can be treated independently[19]. From a classical point of view, Eq. (2.49) compared with Eq. (2.38) gives the identity $\gamma_{TO} = \gamma_{LO}$ for a single mode. If $j > 1$ then γ_{LOj} becomes a function of all other dispersion parameters but the identity between the longitudinal and the transverse damping functions remains approximately verified in the case of well separated infrared bands (Gervais and Piriou, 1974). Therefore, for many materials a description of the permittivity with the classical Lorentz oscillator Eq. (2.38) is still reasonable although the principal assumption of a constant damping function is unphysical as stated above.

For a description beyond the classical model, a comparison of the results of the previous section in form of Eq. (2.39) with Eq. (2.49) is needed. From this comparison an expression for the generalized damping function $\Gamma(\mathbf{k}j;\omega;T)$ can be achieved, that results in a term

[19] This leads to several interesting conclusions, e.g. Eq. (2.49) serves the possibility to derive a generalized *Lyddane-Sachs-Teller* relation just as several sum rules forming the relationship between the different parameters (in Barker Barker (1964b) some of these conclusions are well described).

where all parameters are present. Only to a first approximation and with the constraint that $\gamma_{TOj} = \gamma_{LOj}$, it will equal γ_{TOj} and an expression as given in Eq. (2.40) is gained. Vice versa, the damping functions of both the longitudinal and the transverse vibration mode can be expressed in terms of $\Gamma(\mathbf{k}j;\omega;T)$ and get a temperature and frequency dependence.

Since the frequency dependence of the damping parameters can be seen as only slowly varying (Gervais and Piriou, 1974), the *four-parameter-semi-quantum*(FPSQ)-model is achieved by neglecting also the frequency dependence of $\Delta\omega_j(\mathbf{k};\omega;T)$ in Eq. (2.40) and can be written as

$$\epsilon = \epsilon_\infty \prod_j \frac{\omega_{LOj}^2(\mathbf{k};0) - \omega^2 + 2\omega_{LOj}(\mathbf{k};0)[\Delta\omega_{LOj}(\mathbf{k};T) - i\omega\gamma_{LOj}(T)]}{\omega_{TOj}^2(\mathbf{k};0) - \omega^2 + 2\omega_{TOj}(\mathbf{k};0)[\Delta\omega_{TOj}(\mathbf{k};T) - i\omega\gamma_{TOj}(T)]}. \tag{2.50}$$

This is the FPSQ model that can finally be used for a calculation of the dielectric properties of materials with a polar character when the $\omega_{TOj}(\mathbf{k};0)$ and $\omega_{LOj}(\mathbf{k};0)$ (the frequencies of the related modes without phonon-phonon interaction) are known. If those frequencies are not known, the FPSQ model is given in the form of Eq. (2.49) with the extension of temperature dependent damping functions and relations to ω_{TOj} and ω_{LOj}, respectively, as given in Eq. (2.40).

Although the FPSQ model provides a physical more reasonable approximation to the permittivity, it should be mentioned that in principle the above given formulae contain the possibility to get negative imaginary parts of ϵ if the constraints on the damping parameters are not set in a right manner. Such a behavior is excluded in case of the Lorentz oscillator due to the single damping parameter per mode that is by definition always positive. Therefore, in case of an application (e.g. for fits) the FPSQ model has to be treated carefully to avoid unreasonable results.

2.3.4. Contributions of higher order phonon processes

To this point, it has been assumed that light (or better photons) create single phonons whereas the involved photon will be totally absorbed. Such processes are also called one-phonon-processes in the framework of the interaction with electromagnetic fields. If one would deal with a perfect harmonic crystal, only one-phonon-processes would have to be treated. Processes with more than one phonon involved are a consequence of the anharmonicity of the lattice and the consequential possibility of the interaction between the phonons. Therefore, in real crystals, the influence of multiphonon processes on the spectra have to be considered. They become important especially toward the transparency regimes (Zeidler et al., 2011) at the higher and the lower frequency edge of the main IR vibrations of ionic

crystals. Generally, two main processes have to be distinguished: *phonon difference processes* and *phonon-sum processes*.

In a phonon difference process one or more phonons of certain branches are created while other phonons of other branches are annihilated. The energy and momentum conservation is provided by a photon that is absorbed. Because the phonon density of state is highest at the boundary of the Brillouin-zone where the dispersion curves are flat and comparably close (see Fig. 2.3), phonon difference processes mainly happen there. The energy difference between the modes close to the boundary of the Brillouin-zone is usually quite low. Hence, phonon difference processes play the main role in the absorption at the low-frequency edge of lattice vibrations. Phonon-sum processes, on the other side, are responsible for absorptions at frequencies higher than those of the main lattice vibrations. Here, simply spoken, two or more phonons are created by an incoming photon while the photon that carries the energy of all created phonons is annihilated. Since also the momentum has to be conserved, the sum of the wave vectors $\mathbf{k}_i$ of the created phonons must be equal to the momentum of the incoming photon that is roughly zero compared to the majority of all possible phonon wave vectors. The respective momenta of the annihilated and the created phonons must therefore be the same.

Analogous to the considerations that have been made in the previous section, phonon creation and annihilation operators can be defined which can be used to determine the probability of creating and annihilating a phonon. For the creation of phonons in a certain branch j with the wave vector $\mathbf{k}_j$ in a field with n photons, it is (Schall, 2001)

$$P_{n_j(\mathbf{k})\to n_j(\mathbf{k})+1} = \left|\langle\psi_{n_j(\mathbf{k})+1,n}|H|\psi_{n_j(\mathbf{k}),n'}\rangle\right|^2 \propto n_j(\mathbf{k})+1 \tag{2.51}$$

and for the annihilation

$$P_{n_j(\mathbf{k})\to n_j(\mathbf{k})-1} = \left|\langle\psi_{n_j(\mathbf{k})-1,n}|H|\psi_{n_j(\mathbf{k}),n'}\rangle\right|^2 \propto n_j(\mathbf{k}). \tag{2.52}$$

Here, $n_j(\mathbf{k})$ is the occupation number of the phonons as given in 2.10. H is the Hamiltonian of the photon-phonon interaction and ψ is the combined wave function of photon and phonon.

The probability of a two-phonon difference process at which a phonon of the energy $\hbar\omega_1$ is created and another phonon with $\hbar\omega_2$ is annihilated can therefore be estimated via (Schall, 2001)

$$P_\Delta \propto (n_j(\mathbf{k})_1+1)n_j(\mathbf{k})_2 - n_j(\mathbf{k})_1(n_j(\mathbf{k})_2+1) = n_j(\mathbf{k})_2 - n_j(\mathbf{k})_1. \tag{2.53}$$

For an n-phonon-sum processes, the probability is generally described by[20] (Billard et al., 1976)

$$P_{\Sigma} \propto \prod_{i}^{n} (n_j(\mathbf{k})_i + 1) - \prod_{i}^{n} n_j(\mathbf{k})_i. \tag{2.54}$$

Therefore, in the high temperature limit the probability of a two-phonon difference process increases linearly with the temperature T whereas the probability will vanish for $T \to 0$. Since the creation of phonons under annihilation of phonons is taking place mainly at the boundary of the Brillouin-zone where excited phonons must exist, a decrease of T will lead to a freeze-out of excited states and the trend toward a vanishing P_{Δ} is plausible. Thomas (1991) has stated that for an n-phonon difference process the temperature dependence in the high temperature limit is $\propto T^{n-1}$ while the frequency dependence should be in principle $\propto \omega^2$. On the other side, the probability of an n-phonon-sum process is $\propto T^{n-1}$ in the high temperature and a constant term in the low temperature limit (Billard et al., 1976; Schall, 2001). The frequency dependence follows in principle the phonon density that becomes rapidly Gaussian as the order of the phonon-sum process increases (Thomas, 1991).

It should be noted that in these simple estimations the influence of the thermal expansion and the phonon-phonon interactions due to anharmonicity (see the previous section) have not be included. According to Billard et al. (1976), these additional influences will weaken the temperature dependence at least for the phonon-sum processes.

2.3.5. Crystal field theory/Ligand field theory

For investigations of the optical constants in the NIR–IR wavelengths range, besides the lattice vibrations whose energies are in the IR also electronic transition mechanisms with higher energies (usually in the NIR) are important. In the case of the materials which have been investigated (oxides and silicates) the so called *crystal field interaction* is responsible for such transition mechanisms that are theoretically treated in the *crystal field theory* (CFT) or in the more general formalism, the *ligand field theory* (LFT). In this section, only an outline of these theories will be given due to the complexity of this subject.

If an ionic crystal lattice contains transition metal ions (those elements which have no completed d and f orbitals; like Fe, Mn, Ti, Cr,...) in coordination with anions like O^{2-} (ligands), an energetic splitting of the orbitals of the transition metals takes place due to the influence of the surrounding electric field. In the ground state without any external influences, all 5 d orbitals (in Cartesian coordinates they can be denominated as d_{xy}, d_{yz}, d_{xz}, $d_{x^2-y^2}$, and d_{z^2})

[20] at which it should be clear that in general the probability of an n-phonon process is higher than for a $(n+1)$-phonon process and the given proportionality shall only clarify the temperature dependence.

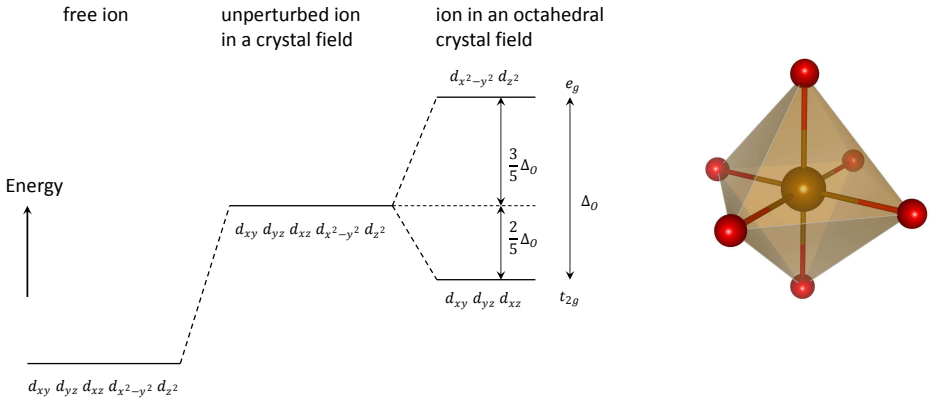

Figure 2.4.: Relative energy levels of a transition metal ion in a free state, in a crystal field with isotropic electric forces, and in a crystal field with octahedral coordination to the ligands after Burns (1993). On the right side, an octahedra of a cation surrounded by anions is drawn with the aid of the software VESTA (Momma and Izumi, 2011).

have the same energy. By applying an external isotropic electric field, the overall energy of the d orbitals is increasing but the orbitals are still degenerated. However, in case of a cubic lattice where the cations are in octahedral coordination by the ligands, there are two solutions for the energy, a twofold degenerated (*Mulliken*[21]-symbol: e_g) and a threefold degenerated (t_{2g}). The energy splitting Δ_0 can be estimated from the expression

$$\Delta_0 \sim \frac{\langle r^4 \rangle}{\langle R \rangle^5}, \tag{2.55}$$

where $\langle r^4 \rangle$ is the mean of the fourth power of the d-electron–core distance and $\langle R \rangle$ is the mean distance from the metal cation to the ligands (Ullrich et al., 2002). The threefold degenerated states have lower energy than the twofold degenerated states (see Fig. 2.4). For a tetrahedral coordination, the five different d orbitals also split into two energy states but now the t_{2g} states have the higher energy.

A further splitting of degenerated states happens when the respective polyhedral symmetry is lowered by distortions along the principal axes (which is the case e.g. in olivine) or by the *Jahn-Teller* effect where a spontaneous distortion is initiated by the lowering of the energy of occupied orbitals with respect to unoccupied or only half occupied orbitals (Burns, 1993). Additionally, there are two selection rules which play an important role for the excitation of the different energy states: the spin-multiplicity selection rule and the *Laporte* selection rule. The first one states that transitions take place only between

[21] This is a notation from group theory where a means a one-dimensional symmetry with respect to the rotation around the principal axis, b a one-dimensional anti-symmetric rotational symmetry, e a two-dimensional and t a three-dimensional symmetry. The related subscripts 1 and 2 mean a symmetry/anti-symmetry with respect to the rotation perpendicular to the principle axis and the subscripts g and u a symmetry/anti-symmetry with respect to inversion.

states of the same spin-multiplicity (Burns, 1993). This selection rule is weakened by the spin-orbit coupling. Thus in some spectra very weak but sharp bands can be associated to spin-forbidden transitions. The Laporte selection rule says that transition between states of the same parity are forbidden. This means that all transitions between the states within an orbital are forbidden but transitions between orbitals with different parity are allowed (e.g. p→d). There are two mechanisms which abrogate at least partly the Laporte selection rule. First, if the environment of the ion lacks a center of symmetry (as in the case of tetrahedral coordination) a mixing between 3d and 4p orbitals may happen which may finally activate a Laporte-forbidden transition (Burns, 1993). The second mechanism happens through the *vibronic* coupling (a coupling between vibrational and electronic wave functions with opposite parities (Burns, 1993)) that leads to a mixing of d and p orbitals even for centrosymmetric positions of the cation (as it is the case for ions in octahedral coordination).

According to Ullrich et al. (2002), the shape of an absorption feature that is due to a crystal field transition, can be well approximated by Gaussians. The width of the respective absorption band gives a measure for the influence of vibrations of both the ligands and the transition metal ions, leading to fluctuations of the crystal field splitting. The integral intensity of an absorption band is proportional to the oscillator strength f of a transition and therefore to its probability of excitation. Finally, the peak position is a measure for the required energy of a transition and therefore for the splitting of the orbitals. According to Huffman (1969), f can be written as

$$f = \frac{\hbar m_e c}{N \pi e} \int \alpha_{\mathrm{Bulk}} d\omega. \tag{2.56}$$

m_e and c are the mass of an electron and the velocity of light, respectively. N is the concentration of ions per unit volume, e is the charge of an electron, α_{Bulk} is the linear absorption coefficient, and ω the frequency of an incoming photon. The integral of α_{Bulk} over ω can be well approximated by the product of the maximum value of α_{Bulk} and the full width at half maximum (FWHM) $\Delta\omega$ of the respective absorption feature (Ullrich et al., 2002):

$$A = \int \alpha_{\mathrm{Bulk}} d\omega \approx \alpha_{\max} \Delta\omega. \tag{2.57}$$

If the temperature of the material is changed, several effects can appear. Due to the dependence of Δ_0 on the inter-ionic distances, an increase of the temperature would lead to a decrease of Δ_0 and thus to a red-shift of the respective crystal field band (CF-band). Furthermore, if the transition is due to a relaxation of the Laporte selection rule, an increase of the temperature will also increase the relaxation due to a stronger vibronic coupling or a stronger deviation from the centrosymmetry. This would lead to an increasing f, following

the dependence (Huffman, 1969; Ullrich et al., 2002)

$$f = f_0 \coth\left(\frac{\hbar\omega'}{2k_B T}\right). \tag{2.58}$$

ω' is here a single effective phonon frequency representing the vibronic coupling. A last effect can be observed in a broadening of the absorption bands with increasing temperature due to a general increase of the influence of vibrations on the crystal field splitting. Following Ullrich et al. (2002),the FWHM $\Delta\omega$ has the principal temperature dependence

$$\Delta\omega \sim \sqrt{\coth\left(\frac{\hbar\omega'}{2k_B T}\right)}, \tag{2.59}$$

with ω' again being an effective phonon frequency.

2.4. Optical properties of small particles

To this point, the considerations of the optical properties have been made by assuming somewhat ideal forms of solids: bulk materials[22]. But for small particles, where small means that the dimensions of the particle are smaller than the wavelength of the incoming electromagnetic radiation (that is the μm range in case of IR light), the influences of the shape of the particle (on e.g. spectra) becomes essential. Thus, some basic inspections on the properties of small particles and their interaction with light is made.

2.4.1. Spherical particles

In an ensemble of particles, absorption and scattering weaken the direct light beam while scattering produces a diffuse light that is radiating in all directions of the medium. The scattering itself depends strongly on the surface conditions of the respective particles and is therefore not easy to determine. A first approximation is done by assuming the shape of the particles to be spherical (Mie-theory). If it is further assumed that the particle is small compared to the wavelength of the incoming radiation, then the *Rayleigh*-solution is achieved.

Considering a small sphere of a certain material, the extinction cross section σ_{ext} is given by

$$\sigma_{\text{ext}} = \frac{P_{\text{ext}}}{J}. \tag{2.60}$$

[22] These are infinitely expanded mediums which have the character of homogenous, with particular properties armed spaces in a macroscopic view.

P_{ext} is the power of the scattered and absorbed light and J is the intensity of the incoming light. Since only a description of the total loss due to the scattering and the total absorption is aimed, it is sufficient to treat the magnitude of the extinction averaged over all spatial directions. If the spherical particles have a cross section $\sigma = \pi a^2$ with a being the radius, then the extinction efficiency is defined as

$$Q_{\text{ext}} = \frac{\sigma_{\text{ext}}}{\sigma}. \tag{2.61}$$

For a homogenous ensemble of N particles in a volume V with the particle density $\rho = N/V$, a volume normalized extinction coefficient (α_{ext}) can be defined which split into a sum of an absorption coefficient (α) and a scattering coefficient (α_{sct}) via

$$\begin{aligned} \alpha_{\text{ext}} &= \rho\sigma_{\text{ext}} = \rho(\sigma_{\text{abs}} + \sigma_{\text{sct}}) \\ &= \alpha + \alpha_{\text{sct}}. \end{aligned} \tag{2.62}$$

Analogous to α_{ext}, a mass normalized extinction coefficient (κ_{ext}) can be defined via $\kappa_{\text{ext}} = \rho_m\sigma_{\text{ext}} = N/M\sigma_{\text{ext}}$, where M is the mass of the whole ensemble[23].

The absorption and scattering cross sections in the Rayleigh approximation are given by

$$\sigma_{\text{abs}} = 2\pi\frac{1}{\lambda}\text{Im}(\alpha_{\text{pol}}), \qquad \sigma_{str} = \frac{8\pi^3}{3\lambda^4}\left|\alpha_{\text{pol}}\right|^2, \tag{2.63}$$

where α_{pol} is the molecular polarizability of the particles as defined in Eq. (2.30). For a spherical particle, it is given by

$$\alpha_{\text{pol}} = 4\pi a^3\frac{\epsilon - \epsilon_m}{\epsilon + 2\epsilon_m} \tag{2.64}$$

(ϵ_m is the dielectric permittivity of the surrounding medium ($\epsilon_m = 1$ in case of vacuum)). Due to its difference in the spatial dimensions, the polarizability is generally a diagonal tensor of the second order and hence is also the absorption cross section having the components $\sigma_{\text{abs j}}$. The absorption cross section is proportional to $1/\lambda$, the scattering cross section goes with $1/\lambda^4$. This means that for sufficiently long wavelengths, the scattering can be neglected compared to the absorption but σ_{sct} strongly increases toward shorter wavelengths. This work deals mainly with the IR properties of materials which can be found as submicrometer sized dust grains in space. Therefore, it is reasonable to focus only on the Rayleigh limit ($a \gg \lambda$) of the scattering and absorption of small particles.

[23]The connection between the absorption in a homogenous medium and α_{ext} and κ_{ext}, respectively, can be established with effective-medium theory (Menella et al., 1998)

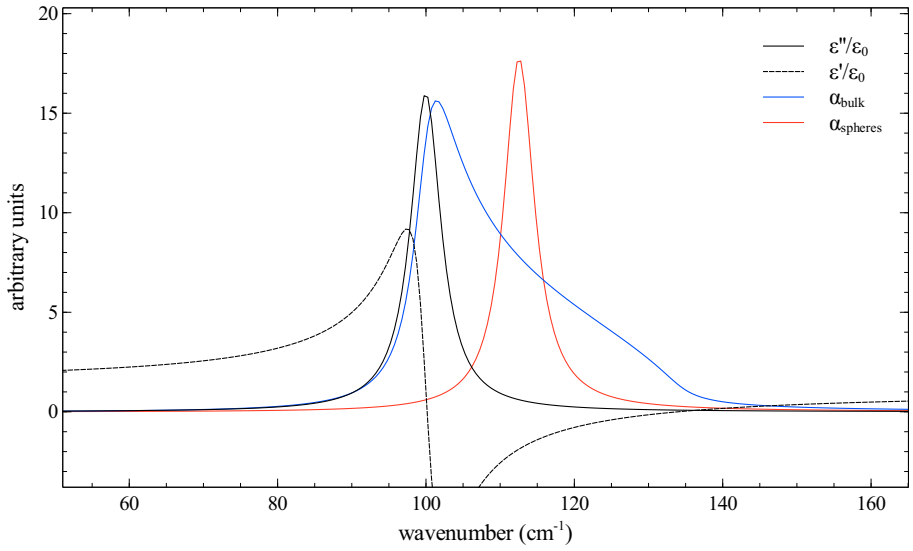

Figure 2.5.: Comparison between the absorption coefficients of a bulk and spheres in the Rayleigh limit of the same material. One mode has been defined for which the resonant frequency is at $100\,\mathrm{cm}^{-1}$ with a damping of $\gamma = 5$. The strength of the presented functions has been set arbitrarily for scaling purposes.

The spectral behavior of an ensemble of small spheres differs from that of a bulk sample of the same material. The linear absorption coefficient of a bulk sample is given by

$$\alpha_{\mathrm{Bulk}} = \frac{4\pi}{\lambda}k = \frac{4\pi}{\lambda}\sqrt{\frac{1}{2}(\sqrt{\epsilon'^2 + \epsilon''^2} - \epsilon')}, \tag{2.65}$$

where λ is the wavelength and k the imaginary part of the refractive index. Obviously, α_{Bulk} has a maximum when ϵ'' has reached its maximum but in case of an ensemble of particles, α increases with $(\epsilon - \epsilon_m)/(\epsilon + 2\epsilon_m)$. Assuming the surrounding medium to be non-absorbing, the absorption cross section is then proportional to $\epsilon''\epsilon_m/[(\epsilon' + 2\epsilon_m)^2 + \epsilon''^2]$ which reached its maximum when the denominator is at a minimum. In Fig. 2.5 the absorption coefficients for a bulk sample and an ensemble of equal and homogenous spheres in the Rayleigh limit of the same material is presented ($\epsilon_m = 1$). The spheres show their maximum in the absorption very close to a frequency where $\epsilon' = -2$ which corresponds to a resonance of the function $1/(\epsilon' + 2)$ that is given for small ϵ'' in Eq. (2.63). The according frequency is called the *Fröhlich*-frequency and the resonant mode the *Fröhlich*-mode.

2.4.2. Ellipsoidal particles

Beside the size effects, the shape of the particles has a big influence on its spectral behavior. However, beside the sphere and the up to infinity elongated cylinder, only for ellipsoids there are analytical solutions for the extinction. For a homogenous ellipsoid the polarizability is

(Bohren and Huffman, 1983)

$$\alpha = \begin{bmatrix} \alpha_1 & 0 & 0 \\ 0 & \alpha_2 & 0 \\ 0 & 0 & \alpha_3 \end{bmatrix} = 3v \begin{bmatrix} \frac{\epsilon_1-\epsilon_m}{3\epsilon_m+3L_1(\epsilon_1-\epsilon_m)} & 0 & 0 \\ 0 & \frac{\epsilon_2-\epsilon_m}{3\epsilon_m+3L_2(\epsilon_2-\epsilon_m)} & 0 \\ 0 & 0 & \frac{\epsilon_3-\epsilon_m}{3\epsilon_m+3L_3(\epsilon_3-\epsilon_m)} \end{bmatrix}. \tag{2.66}$$

The L_i for $i = 1, 2, 3$ are geometrical factors which account for the dimensions of the ellipsoid, the so called form factors, and v is the volume of the ellipsoid. If the material is non-isotropic, ϵ has to be used in each direction separately. For $L_1 = L_2 = L_3 = 1/3$, the solution for the homogenous sphere is achieved. The form factors be derived by the formula:

$$L_i = \frac{x_i x_j x_k}{2} \int_0^\infty \frac{dq}{(x_i^2 + q) f(q)} \tag{2.67}$$

where the $x_{i,j,k}$ are the dimensions of the ellipsoid along the three semi axes i, j, k and $f(q) = (x_i^2 + q)(x_j^2 + q)(x_k^2 + q)$ (Bohren and Huffman, 1983) and q is an ellipsoidal coordinate. The absorption and scattering cross sections can be derived by Eq. (2.63) where the constraint $\sum_i L_i = 1$ must be valid.

A simplification can be obtained by the treatment of spheroids which have two axes of equal length. As a consequence, only one form factor is independent. It can be distinguished between *prolate* spheroids where $x_j = x_k$ and *oblate* spheroids where $x_i = x_j$. For both forms, it is $L_2 = L_3$. The independent form factor L_1 can be derived for prolate particles by

$$L_1 = \frac{1 - e^2}{e^2} \left(\frac{1}{2e} \ln \frac{1 + e}{1 - e} - 1 \right), \qquad e^2 = 1 - \frac{x_j^2}{x_i^2} \tag{2.68}$$

and for oblate particles by

$$L_1 = \frac{1}{e^2} \left(1 - \frac{\sqrt{1 - e^2}}{e} \sin^{-1}(e) \right), \qquad e^2 = 1 - \frac{x_k^2}{x_i^2}. \tag{2.69}$$

e is the eccentricity of the spheroid and ranges in both cases from 0 to 1. The components of the absorption cross section, $\sigma_{\text{abs j}}$, can be added to an averaged absorption cross section of an ensemble of randomly oriented ellipsoids to (Bohren and Huffman, 1983)

$$\langle \sigma_{\text{abs}} \rangle = \frac{1}{3} \sum_{j=1}^{3} \sigma_{\text{abs j}} = \frac{2\pi v}{3\lambda} \text{Im} \left(\sum_{j=1}^{3} \frac{\epsilon_j - \epsilon_m}{\epsilon_m + L_j(\epsilon_j - \epsilon_m)} \right). \tag{2.70}$$

The absorption cross section for an ensemble of non-equal ellipsoids satisfies a certain shape probability function P (Bohren and Huffman, 1983). Since the constraint has been set that the sum of all form factors has to be 1, P depends only on two form factors and the integral of the function over $L_1$and L_2 (without limiting the universality L_1 and L_2 can be set to determine P) must be equal to unity. If it is taken also into account that $L_1 \leq L_2$, the integral of $P(L_1, L_2)$ can be split off into an iterated integral (Bohren and Huffman, 1983):

$$\iint P(L_1, L_2) dL_1 dL_2 = \int_0^1 dL_1 \int_0^{1-L_1} P(L_1, L_2) dL_2 = 1. \tag{2.71}$$

For an ensemble of non-equal ellipsoids, the averaged absorption cross section is therefore

$$\langle\langle \sigma_{\text{abs}} \rangle\rangle = \iint \langle \sigma_{\text{abs}} \rangle P(L_1, L_2) dL_1 dL_2. \tag{2.72}$$

The integral in Eq. (2.72) can be reduced to a single integral over a generalized form factor L (Min et al., 2008):

$$\langle\langle \sigma_{\text{abs}} \rangle\rangle = \frac{2\pi v}{\lambda} \text{Im} \left(\int_0^1 \frac{P(L)(\epsilon - \epsilon_m)}{\epsilon_m - L(\epsilon - \epsilon_m)} dL \right) \tag{2.73}$$

with the form factor distribution function $P(L)$. In the most simple case, all shapes are equally probable which corresponds to a form factor distribution function of $P(L) = 2(1-L)$ (Min et al., 2008):

$$\langle\langle \sigma_{\text{abs}} \rangle\rangle = \frac{4\pi v}{\lambda} \text{Im} \left(\frac{\epsilon}{\epsilon - \epsilon_m} \ln \left(\frac{\epsilon}{\epsilon_m} \right) \right). \tag{2.74}$$

That is the case of the *Continuous Distribution of Ellipsoids* (CDE) which has been introduced in Bohren and Huffman (1983) and that serves a first good approximation to the IR properties of a real dust cloud as it can be found e.g. in space. Note that the particle volume v is now a constant particle volume over the whole ensemble.

2.4.3. Irregularly shaped particles

More realistic form factor distributions can be calculated from a discretization of certain particle shapes, as has been shown by Min et al. (2008). Two of these are illustrated in the small diagram in Fig. 2.6, together with the form factor distribution of the CDE (single spherical particles would produce a single peak at $L = 1/3$). They represent irregular particles and aggregates of homogenous spheres. The corresponding models which are used

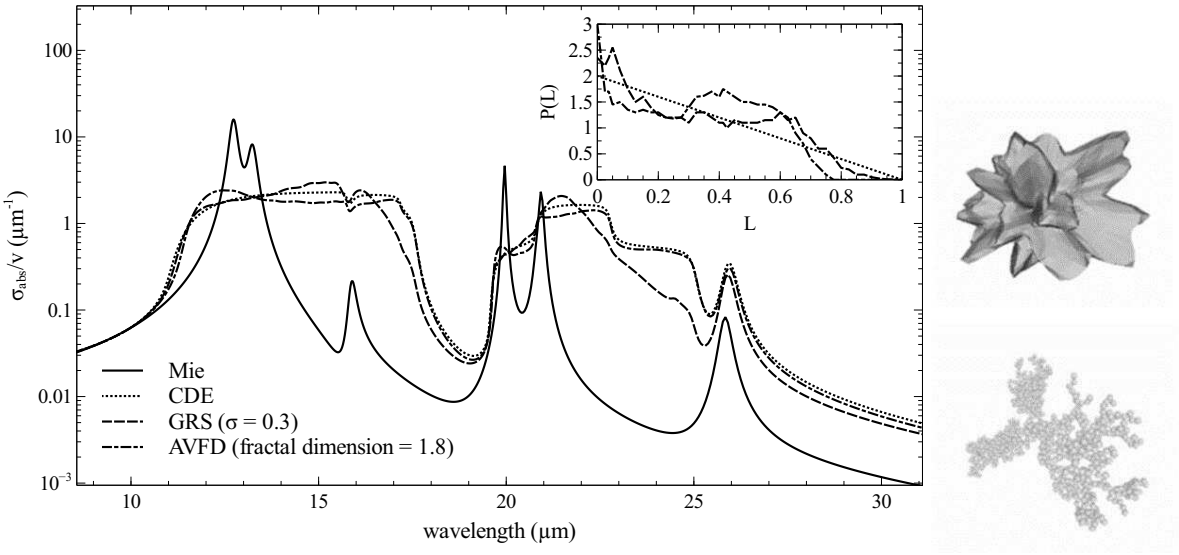

Figure 2.6.: Left: comparison of the different models of the approximation to the averaged absorption cross section of an ensemble of corundum particles. The optical constants which were necessary for the calculation have been obtained via reflection measurements within the scope of this work. Right: sketches of a GRS (top) and an AVFD (bottom), taken from Min et al. (2008)

for the determination of the form factor distribution are the approach of the *Gaussian-Random-Sphere* (GRS) and of the Aggregates with Various Fractal Dimension (AVFD), respectively. For visualization purposes, the principal shape of the respective particles in both models is given as small picture on the right side of Fig. 2.6 (taken from Min et al. (2008)).

Due to the discretization, $P(L)$ becomes a discrete set of numbers for which the integral in Eq. (2.73) turns into a sum over the number of L values. The result in $\langle\langle\sigma_{\mathrm{abs}}\rangle\rangle$ for the two cases is shown in the main diagram in Fig. 2.6, for corundum as example material, in comparison with the CDE and the Mie-model in Rayleigh approximation. The symbol σ in case of GRS is a measure for the degree of irregularity of the particle. The value 0.3 corresponds to the shape of the GRS on the right side (top) of this figure. The same holds true for the AVFD where the fractal dimension is the general shape parameter, ranging from 1 (straight chain) to 3 (homogenous sphere). The absorption features of all models, the CDE, GRS, and AVFD, broaden and decrease in intensity compared to the Mie model. Also, the features tend to broaden toward longer wavelengths. On the other side, both minimum and maximum values are less distinct compared to the Mie-model. The spectra of the CDE and the GRS are quite similar at the short-wavelengths side of the respective absorption feature whereas at the long-wavelengths side the spectrum of the CDE is more similar to that of the AVFD. This effect is owed by the similar development of $P(L)$ in all cases. For the AVFD, the shape of $P(L)$ is slightly more different from that of the CDE which finally leads to the differences on the short-wavelengths side of the features.

3. Experimental setup for temperature dependent in-situ spectroscopy in the IR and NIR

In this work, temperature dependent reflection and transmission spectra of crystalline materials are investigated. The reflection measurements were done in the IR wavelengths range on the synthetic samples of corundum and spinel as well as on the natural samples quartz, olivine, and enstatite. In that range, the optical constants, n and k, undergo significant changes with the wavelength of the incoming radiation while in their magnitude, they become comparable. Therefore, reflection measurements are crucial to determine both n and k which are necessary to calculate the absorption cross section (see section 2.4). With transmission measurements (done on the olivine crystal) in the NIR, only k can be determined which is, however, sufficient because of the only weak interaction of ionic crystals with light in that range leading to an almost constant n. In the following, the spectrometers used for the reflection and transmission measurements in the IR and NIR wavelengths range, respectively, and the devices used for cooling and heating the samples are introduced.

3.1. Temperature dependent IR reflection measurements

3.1.1. The Bruker FTIR spectrometer

The IR measurements which are presented here have been taken with the Fourier-Transform-IR (FTIR) spectrometer Bruker 113v. This spectrometer consists of three main parts. In the first part, non-monochromatic light from a Globar[1] becomes modulated by a *Michelson*-interferometer. The modulated radiation is directed with a rotatable mirror into one of the two sample chambers of the spectrometer; the second part. Parabolic mirrors at the entrances of the respective chambers create a distinct focus of the light onto the sample. The third part of the spectrometer contains the detectors. The outgoing IR beam becomes again focused to a DTGS (deuterated triglycine sulfate) detector with a KBr window for

[1] A SiC rod that is heated to temperatures up to 1600°.

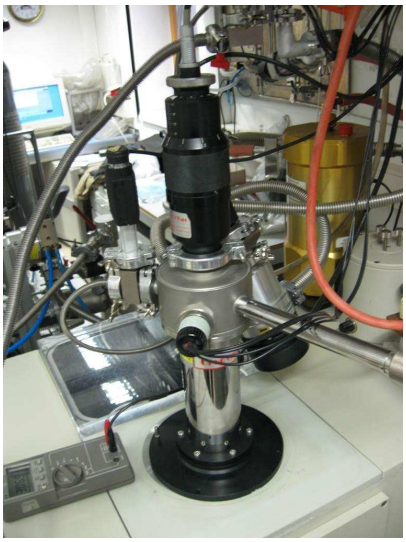

(a) Photograph of the cryostat. On the right, the adapter for the flow of the liquid helium and on the left side the vacuum conductor of the sample chamber can be seen.

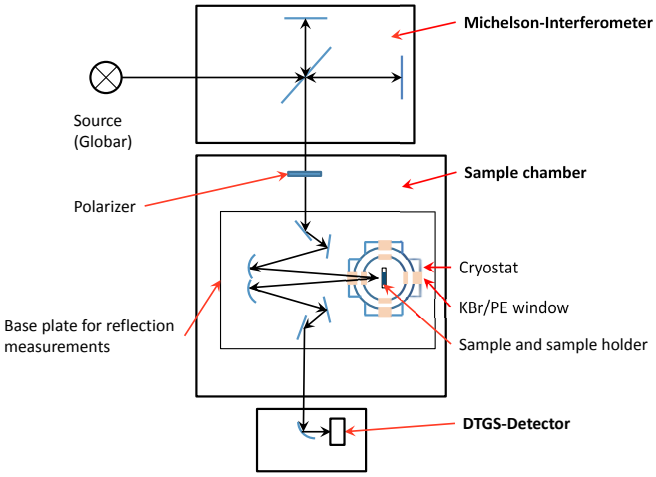

(b) Sketch of the Bruker FTIR spectrometer with the principal setup for the low-temperature measurements.

Figure 3.1.

measurements in the MIR (2-60 μm). A simplified sketch of the setup of the spectrometer can be seen in Fig. 3.1(b) A laser source is necessary for the sampling of the interferogram that is taken by the detectors.

The Bruker spectrometer can be evacuated to pressures of ∼10 mbar (which is maintained by dry air coming from the scanner-air-bearing). Therefore, measurements can be taken almost without any influences from the air. The taken interferograms are recorded by a computer and a special software for taking measurements with the Bruker spectrometer (OPUS). By discrete Fourier transformation, with respect to the sampling signal from the laser, the spectrum can be calculated from the interferogram.

3.1.2. Low-temperature measurements

In the framework of this thesis, low-temperature dependent reflection measurements with the aid of a helium-cooled cryostat (Cryo Vac KONTI Spectro B, see Fig. 3.1(a)) have been done. The cryostat consists of two concentric chambers, an inner chamber that contains the sample holder and an outer chamber in which an isolating vacuum is created. A continuous flow of liquid helium (4.7 K) cools down the wall between sample chamber and isolating chamber. The samples can be cooled down to 10 K by helium gas at a pressure of 10 mbar, providing

thermal contact with the liquid-helium cooled sample chamber walls. The temperatures of sample and wall are controlled by two silicon diode temperature detectors which are connected to an external temperature controller (Cryovac TIC 304-M) that additionally contains a heater for the wall to balance the temperature for the measurements. Heating of the sample mount allows for stabilization of the sample temperature to less than 1 K variation during the 20–30 min measuring time at each temperature. The cryostat has all in all eight windows which let the IR light pass through the cooling and the sample chamber toward the sample, two pairs of PE (for measurements in the FIR) and two pairs of ZnSe windows (for measurements in the MIR). Each pair is built obverse to the respective other pair (see Fig. 3.1). The sample holder is placed in the middle and can be turned to realize measurements either with PE or ZnSe windows. The cryostat itself is built into a chamber of the FTIR spectrometer. To perform reflection measurements, a special base plate for the Bruker spectrometer has been used that carries the cryostat and focuses the IR light through the respective windows of the cryostat onto the sample whereas the reflected light goes through the cryostat windows again and is being directed to the DTGS detector by the mirrors of the base plate. The angle of incidence of the light beam is $\sim 11^\circ$ which results in a relative deviation to a reflection perpendicular to the surface of the sample of $\sim 3\%$. Transmission measurements can be done by using a respective base plate on that the cryostat and the respective sample inside the cryostat stand directly in the focus of the IR beam.

Before the cooling could be started, the inner chamber had to be flooded with dry helium gas and again evacuated several times to rinse the sample chamber from other gases than helium. Because water, for instance, will be in any case a solid at 10 K, it can condense on the sample and thus falsify the results of the measurements. A particular description of the cryostat and the cooling and measurement procedure, respectively, can be found in Henning and Mutschke (2003).

3.1.3. High-temperature measurements

The high-temperature measurements which are presented in this work have been done with a water cooled High-Temperature-High-Pressure (HTHP) cell. With this cell (Specac P/N 585 0) it is possible to heat samples to temperatures up to 1073 K and to take infrared spectra at the same time. The cell is deployed into an aluminum tank that is placed in one of the two sample chambers of the Bruker spectrometer in order to perform IR reflection measurements (see Fig. 3.2). The tank separates the cell environment from the vacuum inside the spectrometer. Therefore, we had to flood the tank with argon gas at atmospheric pressure to minimize the influence of H_2O and CO_2 in the air onto the IR spectra. The IR beam can be applied for the measurements by using two opposite windows in the tank. We

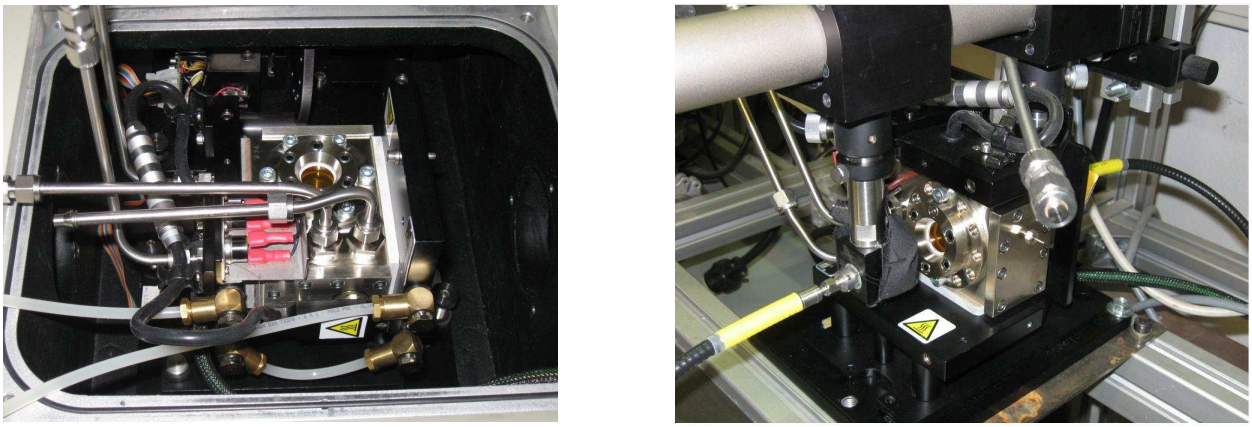

Figure 3.2.: Pictures of the HTHP-cell. Left: the HTHP-cell in reflection mode as it is built into the used Buker FTIR spectrometer. Right: the cell in transmission mode for measurements in the NIR–UV. The yellow-marked cables are the optic fibers and the view is on the second ZnSe window for the out going beam.

used both potassium bromide (KBr) and polyethylene (PE) windows for measurements in the mid infrared (3–25 μm) and far infrared (25–60 μm) wavelength ranges, respectively.

The HTHP cell has been set in reflection mode where a base plate with two adjustable mirrors for the incoming and outgoing IR beam is used. The incident angle of the incoming beam on the surface of a sample in the cell is $\sim$12°. Therefore, the estimated relative error in reflectance to the case of perpendicular irradiation is of $\sim$3%. The cell itself has a closed sample chamber. Windows of ZnSe allow reflection and transmission measurements in the wavelength range 0.5–22 μm and are necessary for measurements at high pressures or under special atmospheric conditions. For the IR reflection measurements, the ZnSe window for the incoming and outgoing beam has been removed to measure spectra also at wavelengths beyond 22 μm and to get rid of the temperature dependence of the absorption features of ZnSe.

The sample holder inside the cell is covered by the heater and has a diameter of 13 mm and a length of $\sim$15 mm. Special rings can be screwed into the holder to carry and/or to fix the sample. There are two kinds of these rings: one with a hole of 12 mm that was used to hold the synthetic samples and one with a hole of 5 mm for the natural crystals.

The HTHP cell is supplied with an external temperature controller by which the heating temperature and the temperature gradient can be set. The controller measures the temperature of the sample holder and of the body of the cell. Since the thermocouple inside the sample holder is calibrated for working without one of the ZnSe windows, we additionally measured the temperature of the sample holder with a NiCr-Ni thermocouple. The externally measured temperatures are only by a few percentage points smaller than the temperatures measured by the temperature controller. All sample temperatures given in the IR results are externally measured ones. For the heating process itself, we used a constant temperature

gradient of 10 K/min to reach the respective measurement temperature. For all samples, we took mid-infrared spectra at 300 K, 551 K, 738 K, and 928 K. For quartz, we also measured at 833 K to derive more information on the development of the spectrum in the vicinity of the phase transition from α- to β-quartz (see Sec. 4.3). We have chosen only these few different temperatures to prevent the heater from stronger abrasion.

3.1.4. Performing reflection measurements

IR reflection measurements with the HTHP cell in reflection mode and with the cryostat in a wavelength range of 5-60 μm have been done. For the measurements, both synthetic and natural samples have been used at which it had to be ensured that they do not exceed a diameter of 13 mm. Otherwise, they would not fit into the HTHP-cell (the cryostat has a wider tolerance).

The reflectance R, indicating the ratio of the intensities[2] between incident (from medium 1) and reflected (on medium 2) light, is proportional to the squared amplitude of the respective electric field vectors and can be written with the aid of Eq. (2.34) for near normal incidence as

$$R = \frac{|E_0^r|^2}{|E_0^i|^2} = \left|\frac{m_2 - m_1}{m_2 + m_1}\right|^2 = \frac{(n_1 - n_2)^2 + (k_1 - k_2)^2}{(n_1 + n_2)^2 + (k_1 + k_2)^2}. \tag{3.1}$$

In all measurements, medium 1 was either vacuum, air or argon gas. Therefore, n_1 and k_1 could be set to be roughly one and zero, respectively. In practice, a spectrum of a polished gold mirror with a diameter of 12.7 mm were used as incident light ($|E_0^i|^2$). This reference spectrum was taken only at temperatures below or equal to 300 K since temperatures higher than 500 K destroy the gold layer. Additionally, infrared reflection spectra have been taken from the empty sample holders[3]. These empty-measurements have been taken also at the respective temperature of the before-measured sample and were necessary to exclude reflections from the whole sample holder setup. The spectra from sample R_S and empty cell R_E, both related to the reference, define the pure reflection spectra (R) via

$$R = \frac{R_S - R_E}{1 - R_E}\,. \tag{3.2}$$

Those crystals which are non-isotropic (corundum, quartz, olivine, and enstatite), had been cut along the principal axes which are determined in case of the natural samples by X-ray diffraction or by the shape of the crystal. The synthetic samples are bought by commercial

[2]The absolute values of the respective Pointing vectors

[3]In case of the HTHP-cell, the sample holder is only equipped with the ring that has been used for the respective sample

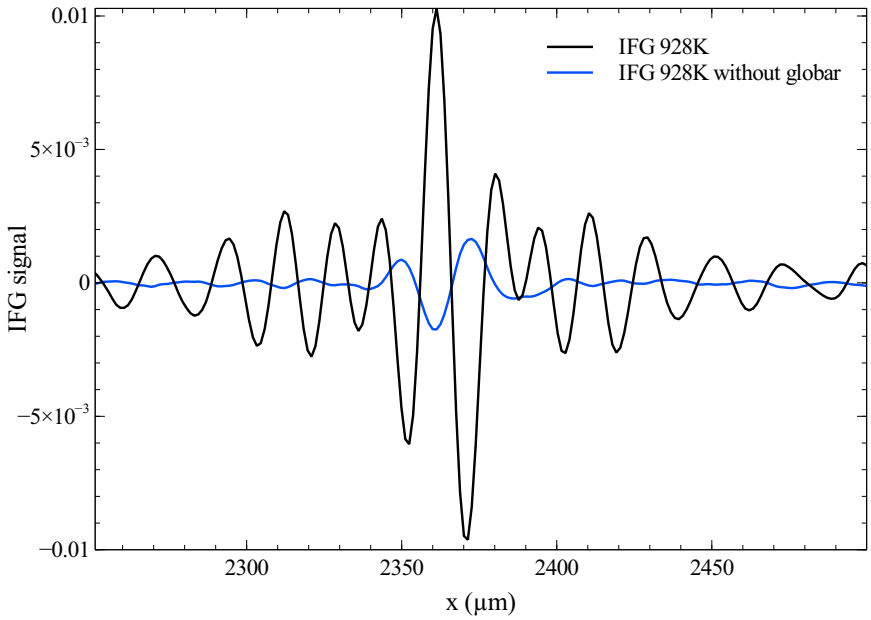

Figure 3.3.: Two interferograms (IFG) of the Bruker spectrometer equipped with the HTHP cell. The heated corundum sample (at 928 K) in the cell radiates toward the interferometer where the radiation becomes modulated (blue curve) and adds to the interferogram of the globar source. The resulting superposition is shown in black.

purchasers with already oriented surfaces. After cutting, the surfaces were polished. A polarizer has been placed in the incoming beam for the cryostat setup and in the outgoing beam for the HTHP cell setup to distinguish between the different crystal orientations. We used two kinds of polarizers: a KRS-5 polarizer for mid-IR measurements (5-25 μm) and a PE polarizer for far-IR measurements (25-60 μm). With the aid of a low-resolution real time spectra shooting in the setup mode of the spectrometer software, the correct polarizer adjustment has been established by finding the maximum of bands or by the disappearance of other bands (Zeidler et al., 2013).

For the HTHP cell, it could be verified that the heated sample and the sample holder themselves serve as additional IR sources whose emissions contribute to the spectra. While the radiation directly emitted toward the detectors gives a DC (direct current) signal and is filtered out, the radiation back to the interferometer of the spectrometer becomes modulated and is superimposed to the modulated IR beam from the globar source of the spectrometer. Therefore, all taken interferograms would be superpositions of actually two sources (see Fig. 3.3). To get rid of the additional influence we simply measured the interferogram of the heated cell alone by decoupling the globar source and subtracted the result from the interferogram with activated globar source. After this, the resulting interferogram is Fourier transformed into the desired *single channel* reflection spectrum ($\sim |E_0^r|^2$) which is used to calculate R_S or R_E.

3.2. Temperature dependent NIR transmission measurements

3.2.1. The Lambda 19 NIR-UV spectrometer

Since reflection measurements in the NIR on ionic crystals are not sensitive to the low absorption between the ranges of the IR vibrations and the UV electronic transitions, all spectroscopic measurements from NIR to the UV have been done in transmission. A Lambda 19 spectrometer from Perkin Elmer has been used. The Lambda 19 is a double-beam spectrometer with a twofold grid-monochromator in *Littrow*-setup which creates a monochrome signal of a wavelength precision of 0.16 nm in the VIS-UV and of 0.6 nm in the NIR. A deuterium lamp (effective wavelengths range 320-175 nm) for measurements in the UV and a halogen lamp (3200-320 nm) for measurements in NIR–VIS served as light sources whereas a PbS (lead-sulfide) detector for the NIR (record range 3200-820 nm) and a side-window photomultiplier for light in VIS–UV (820-175 nm) have been used to record the monochrome signal. Before entering the sample chamber of the spectrometer, the beam is split into two parallel beams at which one beam serves as reference signal and the other one as measurement signal. Both beams are chopped before entering the sample chamber of the spectrometer to get rid of influences of continuous light which may enters the sample chamber. However, if too much external light enters the chamber, frequency-periodic disruptions of the spectra appear (especially in the VIS).

The sample measurements were done externally in the HTHP cell and a closed-cycle cooler (see further subsections). For transferring the monochromatic light from the Lambda 19 spectrometer to the external devices and the transmitted light from back to the spectrometer, NIR fiber optic cables specialized for a wavelengths range from 0.5–3 μm have been used. In the spectrometer, the fibers are fixed on a mirror system which is built into the sample chamber of the Lambda 19 and which couples the monochromatic light into the fibers and back into the Lambda 19 toward the detectors. Owing the losses of energy in the fibers, the difference of the intensities between reference signal and the signal from the fibers is quite high leading to a decreased signal to noise ratio. To decrease the difference in the intensities, a 1 mm aperture was placed into the reference beam of the Lambda 19 which enhanced the signal to noise ratio significantly.

During a measurement, the grids of the monochromators are automatically rotated by the controlling software of the spectrometer ('UVDM', installed on a PC that is connected to the Lambda 19) and the designated wavelength range is screened. The spectrometer itself cannot be evacuated but in the NIR–UV range the influence from water molecules in the air is relatively low and therefore vacuum conditions were not crucial for the measurements.

For taking transmission spectra, via the UVDM software, a calibration to 100% transmission was performed by measurements of the respective empty sample holder and a comparison to the transmission of the reference beam ('auto-zero' measurement).

3.2.2. Low-temperature measurements

We could take low-temperature spectra of our samples in the NIR wavelengths range with the aid of a closed-cycle cryogenic system (APD Displex-series). This system consists of a helium compressor (HC-4) and an expander (CSW-204SL) on which the sample holder is mounted. The expander and the sample holder were covered with a radiation shield and vacuum shrouds (achieved vacuum during the measurements: 10^{-5} mbar). For controlling the temperature, a thermocouple and an electric heater are installed on the expander, both are connected to an external temperature controller. On each side of the vacuum shroud, glass-windows have been mounted for spectroscopic transmission measurements. The windows have diameters of 25 and 10 mm, respectively, and are transparent in the NIR–VIS wavelengths range. The sample is fixed to a sample holder with an aperture of 6 mm.

With the closed-cycle cooler, temperatures down to 10 K can be achieved. If a specific temperature is reached, the heater can be activated and heats against the cooling of the expanding helium gas. This heating-cooling system provides a very stable temperature of the sample holder.

Both ends of the fibers were fixed right in front of the glass-windows on special mounts that contains lenses for focusing and collecting the light from the fibers toward the sample holder and back again into the fibers, respectively. In preparation of the measurements, the fibers have to be adjusted to the aperture and thus to a maximum signal of the detector. Also, auto-zero measurements had to be performed with the empty sample holder.

3.2.3. Transmission measurements with the HTHP cell

In order to take transmission measurements, the HTHP cell has been set on a special base plate on which the cell could be deployed upright in transmission mode (see Fig. 3.2). In this mode, light enters the cell through one of the ZnSe windows, goes through the sample that is fixed by the rings and leaves the cell through the second window. For the transfer of the monochromatic light, again NIR fibers were used, now horizontal adjusted right in front of the ZnSe windows. As in the case of the low-temperature measurements, both fibers had to be well adjusted for providing the optimal transmission through the sample holder. The empty sample holder served as reference for the auto-zero measurement.

Unfortunately, for measurements at high temperatures, the NIR-polarizer could not be used since it is not appropriate for the hot environment of the cell. Therefore, also at low temperatures no polarizer were used to keep the comparability of the measurements.

3.2.4. Performing transmission measurements

Since the transmission spectra of bulk materials have been measured, it is necessary for the calculation of the absorption spectra that the reflection of the incoming light on the surface of the sample is considered. In the NIR, the imaginary part of the refractive index k is usually much smaller than the real part n. Also, n is almost constant in the NIR–VIS wavelengths range. Therefore, it is sufficient to assume the reflection losses R_{loss} on the sample surface to be

$$R_{loss} \approx \left| \frac{n-1}{n+1} \right|^2 . \tag{3.3}$$

n was determined from the value of ϵ_∞ resulting from the fits to the reflectance (see next chapter). To eliminate the losses of reflection from the spectra, the intensity of the radiation that is available for the absorption has to be calculated. Due to the reflection losses at both boundaries, the intensity of the incoming radiation decreases by a factor $(1 - R_{loss})^2$. Let T_{real} be the transmittance of the pure absorbing medium and T_M the measured transmittance with reflection losses, then

$$\frac{T_M}{(1-R_{loss})^2} = T_{real}, \qquad T_{real} = e^{-\alpha_{\mathrm{Bulk}} x}. \tag{3.4}$$

where α_{Bulk} is the linear absorption coefficient of the bulk sample as introduced in section 2.4.1 and x the thickness of the sample[4]. With the aid of Eq. (2.65), the imaginary part of the refraction index k can be derived via

$$k = \frac{-\lambda ln(T_{real})}{4\pi x}. \tag{3.5}$$

[4]The second part of Eq. (3.4) is also known as the *Lambert-Beer* law.

4. Temperature dependent reflection spectra of selected oxides and silicates

In this chapter, the results of the temperature dependent reflection measurements on all samples are presented and discussed. An introduction to the basic properties of each material is given in preparation of each presentation.

In order to determine the optical constants from the reflectance data, each spectrum was fitted with the FPSQ model or the model of the Lorentz oscillators (see section 2.3.3). The respective parameters of the fits are listed in the appendix. To perform the fits, the standard fit procedure of the programing software SCILAB was used (Scilab Consortium, 2011). The mean deviation from the measured reflectance could be estimated for all fits to be in a range from 1–7.5%, depending on the signal to noise ratio.

4.1. Corundum

4.1.1. Properties

Corundum is an aluminum oxide and has therefore the principle chemical composition Al_2O_3 but the distribution of Al cations in an either face-centered cubic or hexagonal close-packed lattice of oxygen anions results in a manifold of polymorphs of Al_2O_3. When heated, all polymorphs carry out phase transitions toward the thermodynamical most stable form, namely corundum (also α-Al_2O_3; Levin & Brandon Levin and Brandon (1998)). The lattice structure of Corundum is rhombohedral. It is sketched in Fig. 4.1. The oxygen anions arrange in a (slightly distorted) hexagonal close-packing whereas the aluminum cations occupy two thirds of the octahedral interstices. Due to the crystal structure, the interaction with light is not isotropic which means that the optical constants n and k (see chapter 2) have to be calculated for polarizations perpendicular (ordinary) and parallel (extraordinary) to the crystal's symmetry (c) axis. In the literature, the IR active modes of vibration perpendicular to the crystallographic c-axis in corundum have the Mulliken symbol E_u and the vibrations parallel to the c-axis A_{2u} (Iishi, 1978).

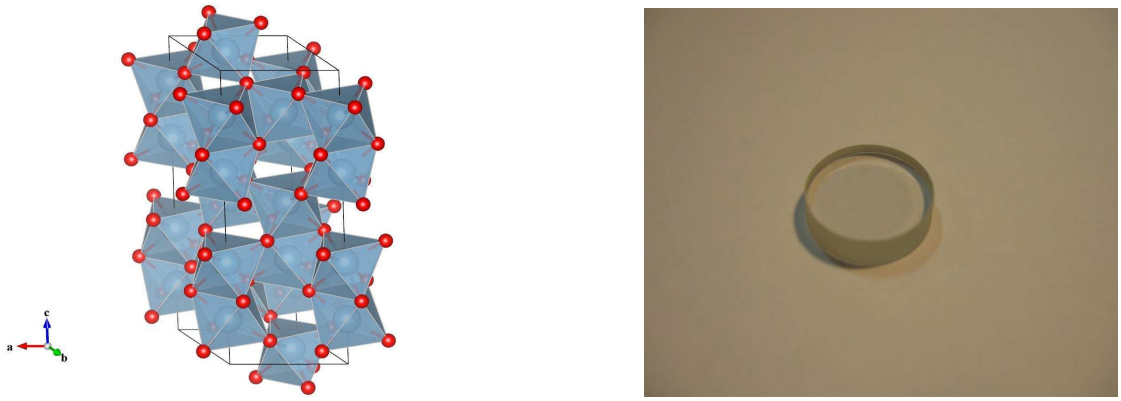

Figure 4.1.: Left: sketch of the unit cell of corundum made with VESTA (Momma and Izumi, 2011). It consists of all in all 12 Al^{3+}-ions (blue spheres) and 18 O^{2-}-ions (red spheres). As can be seen, the oxygen ions surround the aluminum ions as an almost perfect octahedron (blue). Right: photograph of the synthetic corundum window that has been used for the measurements.

Corundum is a highly refractory material. It has a condensation temperature much higher than for most other minerals of astrophysical relevance. At pressures of $\sim 10^{-9}$ bar which typically occur in stellar outflows of evolved stars, corundum is stable already at more than 1400 K, while for example silicates condense primarily below 1100 K (Gail, 2003). Hence, it is thought that corundum should be one of the first condensates to form in the envelopes of M type stars. Quantum mechanical calculations of the condensation rates yet have shown that corundum cannot form under these conditions by homogeneous condensation from the gas phase. Gail and Sedlmayr (1998) write that the formation of Al_2O_3 grains occur more likely via grain-surface-reactions on already existing grain seeds of other high refractory materials such as TiO_2 or ZrO_2. Therefore, the exact circumstances of the formation of corundum in space remains unresolved.

Temperature dependent reflectivity measurements on pure corundum samples have been presented in the past already by Gervais and Piriou (1974) for temperatures up to 1775 K. Thereby, In their work, Gervais & Piriou present a description of the four-parameter semi quantum (FPSQ) model and a comparison with the classical oscillator model. They could show that the FPSQ model is a more effective way to fit the reflectivity of polar crystals in the case of wide reflection bands where equal damping of the longitudinal optical (LO) and transverse optical (TO) mode cannot be expected any more (Zeidler et al., 2013). On the other hand, Thomas et al. (1998) developed a model that does not need a four-parameter description of the dielectric function but is based on adding temperature dependent multi-phonon contributions to a classical oscillator model. Thomas et al. (1998) list the parameters for the oscillators together with their temperature dependence, corresponding to a second order polynomial fit, and compared their model with measured data from several other authors and the FPSQ model. An application of the results of Thomas et al. (1998) on measured emission spectra of corundum in the wavelength range of 2.5-20 μm is presented in the work

of Sova et al. (1998). However, the presented measurements on corundum in all of these papers refer only to the ordinary ray (E⊥c polarization). High temperature infrared reflection spectra also for the extraordinary ray (E∥c polarization) which are necessary to calculate small-particle spectra have been first measured in the Jena laboratory within the scope of this work. The results of these measurements are also presented in Zeidler et al. (2013).

4.1.2. Reflection data and fit results

In Fig. 4.2, the reflectance spectra of the used corundum sample (see Fig. 4.1) taken at four different temperatures directly compared with the respective fit results are shown for both crystallographic orientations. The fits were done with the aid of the FPSQ model introduced in section 2.3.3. The irreducible representation of the vibration modes of corundum predicts four oscillators for the ordinary ray which are IR active (Iishi, 1978). Therefore, we fitted the respective spectra with four oscillators and could reproduce the measured reflectance quite well. On the other side, the spectra for the extraordinary ray should be represented by only two A_{2u} modes but the distinct sharp minimum in the reflectance spectra around 21 μm made it necessary to introduce a third oscillator to get a good fit result. Being not an A_{2u}-type mode, this oscillator might be an indicator for effects of surface polishing or for imperfect polarization.

The main changes due to heating occur in the positions, the maximum values, and the widths of the features (or bands). In general, they tend to shift toward longer wavelengths while the maximum value is decreasing and the width is increasing with increasing temperature. As has been mentioned in section 2.2, this effect is due to the anharmonicity of the atomic/ionic potentials. A detailed list of all oscillator parameters can be found in Table A.1, in appendix A[1]. From the parameters it can be seen that the mode positions move toward longer wavelengths (lower wave numbers, respectively) and the respective damping constants increase with increasing temperature which lead to a decrease of the maximum value and to a broadening of the respective reflectance feature (see also next subsection).

Having a look on the quality of the fits, it is obvious that they are different depending on temperature and wavelength range. In general, the noise is much stronger in the FIR than in the MIR because the intensity of the incoming radiation is decreased by the beam splitter of the spectrometer toward longer wavelengths. Additionally, the influence of water molecules in the air is higher in the FIR. Also, generally the noise seems to increase with increasing temperature. The reason lies probably in the correction of the corresponding interferograms (see section 3.1.4) where two measurements are incorporated. Therefore, the noise of the

[1]Since the fits of the data have been done in wave numbers and not in wavelengths, the presented parameters have all the dimension cm^{-1}.

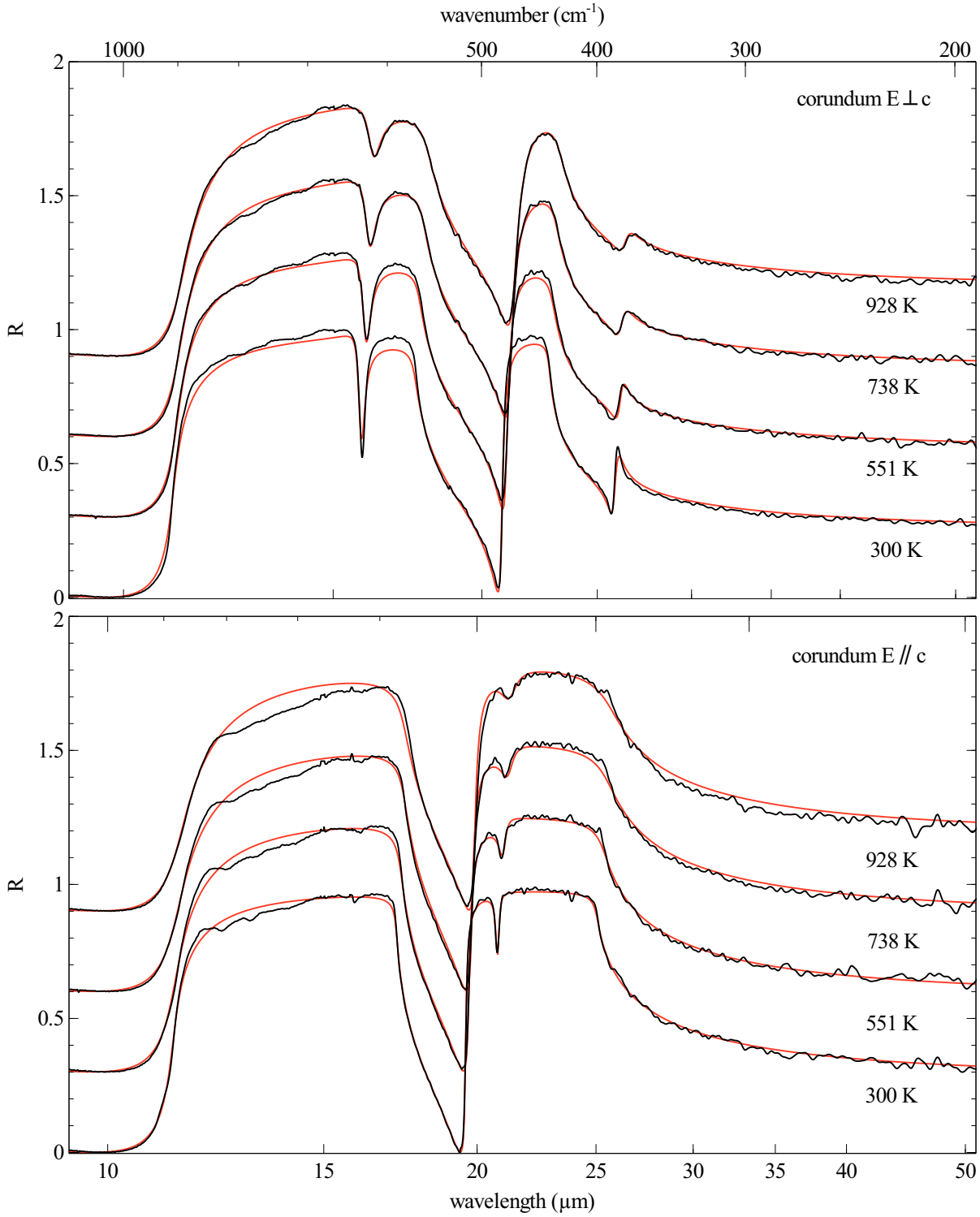

Figure 4.2.: Comparison of the fits (red lines) and the reflection spectra (black lines) for the ordinary ray (E⊥c) and for the extraordinary ray (E||c) of the corundum sample at four different temperatures. The fits were done with four oscillators and three oscillators, respectively. An offset of 0.3 was added between each spectrum for an easier differentiation.

resulting spectrum corresponds also with the influence of the emission on the interferograms which increases with increasing temperature.

As can be also seen, the maximums of the features are not exactly fitted. Either the measured values are too high (for E_u-type modes) or too low (for A_{2u}-type modes). It has been shown by Barker (1964a) that the surface of a sample can have a strong influence on the resulting reflectance spectrum due to additional excited forbidden modes. In the irreducible representation of the modes of vibration, there are also modes which can only be excited by the Raman effect or even neither by Raman nor by IR light. These modes can be said to be forbidden regarding to IR spectroscopy but since a surface always marks the end of an intact crystal lattice, the forbidden modes can become excitable by IR light and depend on the kind of surface treatment. Especially the structures on top of the strongest features measured in both polarization directions give rise to the assumption that they are caused by forbidden modes which finally led to the difference between measurement and fit. The structures seem to become weaker with increasing temperature but at least for the broad feature around 15 μm in the E$\|$c polarization, the deviation from the fit is increasing with increasing temperature. Probably, this effect is due to influences from the other polarization. A tiny structure that corresponds with the distinct minimum at roughly 16 μm in the E$\perp$c polarization, indicates these influences as well. The reason is likely a non-perfectly adjusted polarizer.

4.1.3. Development of the fit parameters with the temperature

The temperature dependence of the complete set of mode parameters for corundum is shown in Fig. 4.3. For the comparison, a plot of the relative changes of the parameters with respect to their respective values at 300 K is chosen, similar to the presentation of the low temperature data of forsterite in Koike et al. (2006). The numbering of the modes is related to the frequency position of the respective TO vibrations, starting with those at lowest frequencies (see also Tables 4.1 and 4.2). It can be seen that the thermal shift of the resonance frequencies ω_{TO} (upper left panel) is relatively similar for all modes. The values change by 1.5–2.5% for 900 K relative to 300 K. The thermal shift for the ω_{LO} modes (upper right panel) has a quite similar development. Here, the values change by 1–2.5%. The difference between ω^2_{LOj} and ω^2_{LOj}, a measure for the strength of each mode (see section 2.3.1), shows only a minor dependence on the temperature. For the parameters which describe the damping, the differences among the modes are considerably larger. It is interesting to note that the damping parameters of the A_{2u}-type modes increase more than for the E_u-type modes. However, no other clear trends (e.g. strong vs. weak modes) can be found.

In the FPSQ calculations of Gervais and Piriou (1974) and Gervais and Piriou (1975) for corundum and quartz as well as in those of Thibaudeau et al. (2006) for spinel, the possible

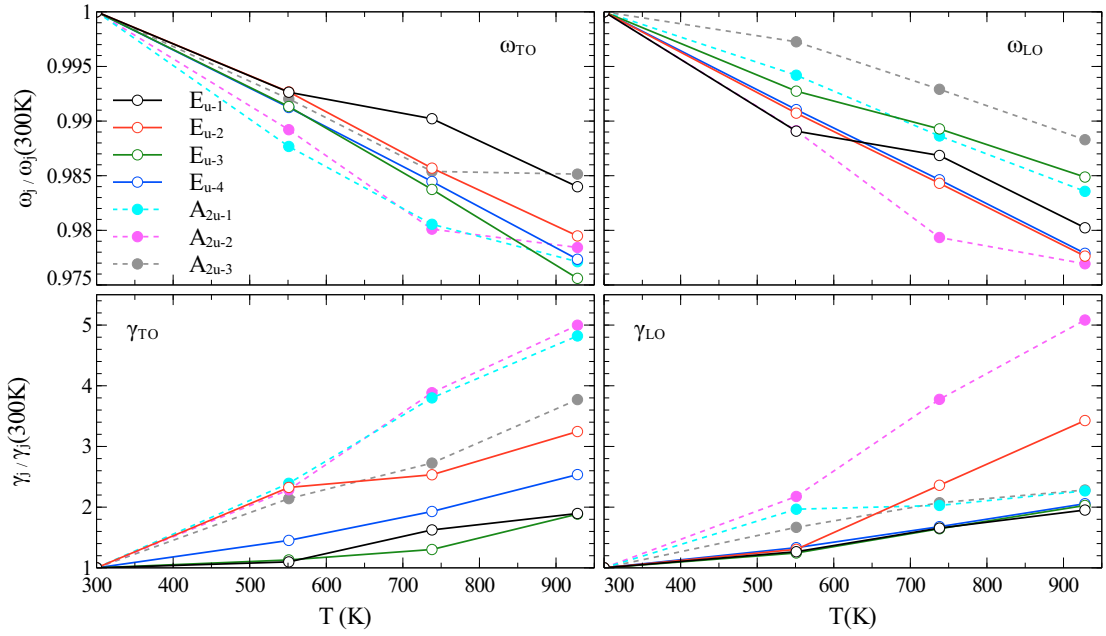

Figure 4.3.: Comparison of the temperature development of the fit parameters of corundum. The parameters have been normalized to their respective value at 300 K and are ordered with respect to *TO* and *LO* mode as well as to frequency and damping.

temperature development of ϵ_∞ has been neglected. However, Cowley (1963) has shown that ϵ_∞ indeed has a temperature dependence when taking multiphonon contributions into account. Therefore, while fitting our data, we generally allowed ϵ_∞ to vary and could indeed verify a certain temperature dependence for corundum, with the general trend of an increase in ϵ_∞ with increasing temperature. For 300 K, we found ϵ_∞ to be 3.05 (ordinary ray) and 2.9 (extraordinary ray) which increases to 3.1 and 2.97 by reaching 928 K, respectively (see also the respective values in Table A.1). This result is supported by the data of Thomas et al. (1998), who compared measured near IR refractive indexes of corundum with their multiphonon model. They found a linear increase of n with increasing temperature, corresponding to a quadratic increase of ϵ_∞. Unfortunately, because of a lack of data at intermediate temperatures, we cannot give any quantitative verification to this dependence.

Because of the limited temperature range and resolution, a fit of the temperature dependence with respect to the theory as given in section 2.2 is quite difficult, especially without having data at lower temperatures. Nonetheless, a fit of both $\omega_j(T)$ and $\gamma_j(T)$ (representative for *TO* as well as for the *LO* modes) has been tried with the aid of the quadratic equations

$$\omega_j(T) = \omega_j(300) + \beta_{j1}(T - 300) + \beta_{j2}(T^2 - 300^2) \tag{4.1}$$

and

$$\gamma_j(T) = \gamma_j(300) + \gamma_{j1}(T - 300) + \gamma_{j2}(T^2 - 300^2), \tag{4.2}$$

respectively. In these, the values at 300 K at both sides have been subtracted which leaves the coefficients β_{j1}, β_{j2}, γ_{j1}, and γ_{j2} unchanged with respect to a 0 K based fit curve. The coefficients have been restricted in the way that $\omega_j(T)$ is ensured to monotonically decrease at least until the melting point of corundum at normal pressure (≈2300 K), while $\gamma_j(T)$ has to monotonically increase. Thus, β_{j1} should be normally negative and β_{j2} is not allowed to be larger than $1 \times 10^{-6}\, cm^{-1}K^{-1}$, whereas γ_{j1} and γ_{j2} are both restricted to positive values.

Table 4.1.: Comparison of the temperature-fit parameters of corundum for the modes in the ordinary ray (E_u-type modes).

j	ω_j cm^{-1}	β_{j1} $(10^{-3}cm^{-1}K^{-1})$	β_{j2} $(10^{-6}cm^{-1}K^{-2})$	γ_{j1} $(10^{-3}cm^{-1}K^{-1})$	γ_{j2} $(10^{-6}cm^{-1}K^{-2})$
1 (TO)	384	-9.84	0.2	0	6.6
2 (TO)	439	-10.67	-3.1	12.02	0
3 (TO)	569	-14.2	-6.5	0	7.9
4 (TO)	634	-19.91	-2.4	2.61	9
1 (LO)	387	-13.62	1	3.38	3.7
2 (LO)	482	-18.39	1	0	8.9
3 (LO)	908	-23.54	1	0	30
4 (LO)	631	-22.72	0.4	6.05	6.8

In the Tables 4.1 and 4.2 the results of the fits are listed together with the frequencies of the respective modes at 300 K as found by the fits. Only the last A_{2u}-type mode (Table 4.2) has a positive β_{j1} which is however compensated by a large negative β_{j2} indicating that the shift of the mode becomes much stronger at high temperature. For some of the E_u and most of the A_{2u}-type modes, β_{j2} reaches the positive limit of $1 \times 10^{-6}\, cm^{-1}K^{-2}$ which indicates that the data imply a significant weakening of the temperature trend at high T. It seems in general that the absolute value of β_{j1} tends to increase with increasing mode frequency, which is due to the fact that we fit here the absolute frequencies, where we have already noted above that the behavior of the relative frequency changes is similar among the modes.

Table 4.2.: Comparison of the temperature-fit parameter of corundum for the modes in the extraordinary ray ($j = 1, 3$: A_{2u}-type modes).

j	ω_j cm^{-1}	β_{j1} $(10^{-3}cm^{-1}K^{-1})$	β_{j2} $(10^{-6}cm^{-1}K^{-2})$	γ_{j1} $(10^{-3}cm^{-1}K^{-1})$	γ_{j2} $(10^{-6}cm^{-1}K^{-2})$
1 (TO)	400	-17.12	1	29.21	0
2 (TO)	482	-19.65	1	15.48	5.4
3 (TO)	582	-17.02	1	15.53	2.1
1 (LO)	511	-9.34	-3.4	3.25	0
2 (LO)	885	-20.59	1	8.25	10.5
3 (LO)	481	3.28	-16.3	47.94	0

As indicated by the fit parameters, the behavior of the $\gamma_j(T)$ with temperature appears to be quite diverse. For the A_{2u}-type modes, where the damping generally increases stronger with the temperature than for the E_u-type modes, the changes can more easily be represented by

a linear fit (large γ_{j1}) and the trend tends to be flattened at larger T (that would result in a negative γ_{j2} but is zero due to our restriction). In contrast, the modes in the ordinary ray (E_u-type modes) show a considerable positive quadratic behavior (γ_{j2} dominating).

If we want to discriminate between thermal expansion effects and the phonon-interaction contribution in the frequency shift, we have to consider Eq. (2.42) and the assumption of a general quadratic temperature dependence of $\omega_j(T)$. We write $\Delta\omega_j(T) = \Delta_{j1}T + \Delta_{j2}T^2$ and set g_j, the mode Grüneisen parameter, as temperature-independent[2]. Then, β_{j1} and β_{j2} can be expressed by

$$\begin{aligned} \beta_{j1} &= \Delta_{j1} - \omega_j(0) g_j \cdot \alpha_0 \\ \beta_{j2} &= \Delta_{j2} - \omega_j(0) g_j \cdot \alpha_1/2, \end{aligned} \tag{4.3}$$

where α_0 and α_1 are the coefficients of the linear thermal expansion $\alpha = \alpha_0 + \alpha_1 T$. Fiquet et al. (1999) determined them for corundum to $\alpha_0 = 2.081 \times 10^{-5}$ and $\alpha_1 = 6.6 \times 10^{-9}\,\mathrm{K}^{-1}$. At room temperature, Lodziana and Parlinski (2003) give an interval for all mode Grüneisen parameters of corundum ranging from 0.4 to 1.8 with an averaged value $\langle g \rangle = 1.14$. They found that the highest values (1.8) are reached by the A_{2u} and the lowest (0.4) by the E_u-type modes. We adopt these values for all temperatures.

Taking $\omega_j(300)$ as an estimate of the $\omega_j(0)$[3], we can derive that for the E_u-type modes (interval of g_j assumed to be [0.4,1.14]) there is a significant Δ_{j1} in the range between -14.63×10^{-3} and $-0.7 \times 10^{-3}\, cm^{-1}K^{-1}$. Similar to the mentioned development of β_{j1}, also the absolute value of Δ_{j1} tends to increase with increasing $\omega_j(300)$. On the other side, Δ_{j2} can be positive or negative depending on the mode and lies between -5×10^{-6} and $3.09 \times 10^{-6}\, cm^{-1}K^{-2}$. It shows no certain development with increasing $\omega_j(300)$. The estimated values of Δ_{j1} for the A_{2u}-type modes in the limits $g_j = [1.14, 1.8]$ are only for $j = 1$ in the same magnitude like the ones for the E_u-type modes. In the case of $j = 3$ they vary between -3.2×10^{-3} and $4.8 \times 10^{-3}\, cm^{-1}K^{-1}$. Though, Δ_{j2} is positive for both modes and lies between 4×10^{-6} and $7.91 \times 10^{-6}\, cm^{-1}K^{-2}$. A general increase of the values for both Δ_{j1} and Δ_{j2} with increasing $\omega_j(300)$ can be found. Since both mechanisms (phonon-phonon interaction and thermal expansion) should have in general negative contributions in their linear coefficients, the calculations confirm that the values of β_{j1} are reasonable.

The particular fits for the temperature dependence and the calculations to estimate the contribution of pure thermal expansion and phonon-interaction to the frequency shift, have been done only for corundum owing its manageable number of modes and the availableness

[2] Since $\mathbf{k} \approx 0$, we disclaimed using the notation of the explicit dependence on $\mathbf{k}$.

[3] As can be estimated from Fig. 4.3, the mode frequency at room temperature will not differ much from its respective value at 0 K

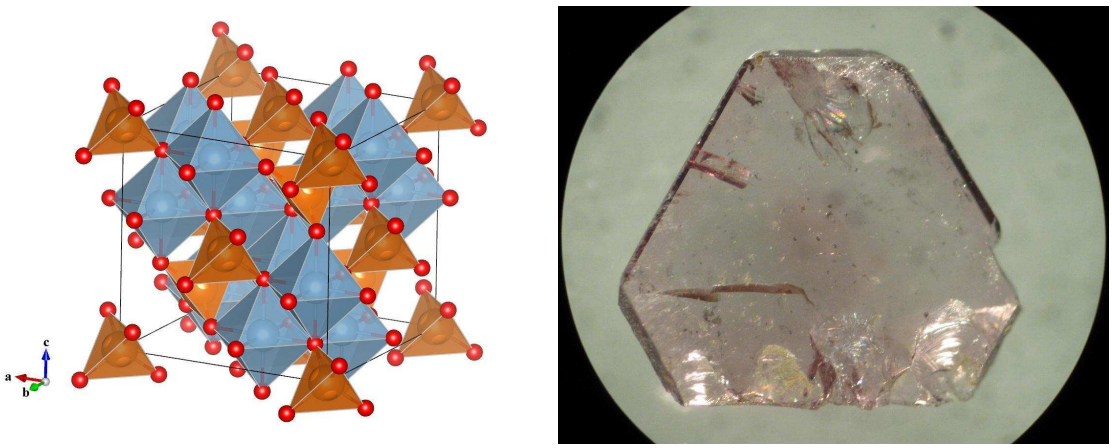

Figure 4.4.: Left: Sketch of the unit cell of a perfect spinel crystal made with VESTA. The blue spheres represent the aluminum cations and the bronze ones the magnesium cations. The small red spheres are the oxygen anions. In a perfect the spinel crystal, the Mg cations form tetrahedra and the aluminum cations octahedra with the oxygen anions. All in all, the unit cell consists of 8 Mg^{2+}, 16 Al^{3+}, and 32 O^{2-} ions. Right: platelet of a natural spinel crystal found in Burma.

of data for the thermal expansion and the mode Grüneisen parameters. Nevertheless, the results are not in all cases distinct, as the values of Δ_{j2} for the E_u-type modes show. Also, to have more significant results, more temperature dependent measurements are necessary and detailed data for the mode Grüneisen parameters (not only intervals) are needed.

4.2. Spinel

4.2.1. Properties

Spinels are minerals with the general composition $(A_{1-x}B_x)[A_xB_{2-x}]O_4$. The cations in parenthesis occupy the tetrahedral sites and the cations in square brackets occupy the octahedral sites of a cubic close-packed oxygen lattice. In this work, we will treat the optical properties of magnesium-aluminum-spinels which are hereafter called spinel in a narrower sense. The sum formula of pure stoichiometric spinel is therefore $MgAl_2O_4$.

Spinel crystals with such compositions have a unit cell consisting of 32 oxygen anions, 16 aluminum and 8 magnesium cations. In a perfect spinel crystal the trivalent Al cations are octahedrally coordinated by oxygen ions, while the bivalent Mg cations are tetrahedrally coordinated which can be also seen from Fig. 4.4. However, it has been found that annealing induces the Mg and Al ions to change their sites, such that a part of the Al ions is occupying the tetrahedral sites and a part of the Mg ions are located in the octahedral sites of the now *inverse* spinel (Tropf and Thomas, 1991; Fabian et al., 2001). This structural transition is

taking place at 1023–1073 K and is apparently irreversible at least at short time scales (Tropf and Thomas, 1991; Fabian et al., 2001). Therefore, because of the high temperatures that are needed for their creation, synthetic spinel crystals are in particular characterized by this deviation from the perfect crystal. In contrast, natural spinel crystals which were exposed to low temperature conditions over long time scales show an almost perfect spinel crystal structure (Zeidler et al., 2013). It seems that at low temperatures and after long time scales the aluminum cations leave the occupied tetrahedral sites and move to the octahedral sites while the opposite is true for the magnesium cations (Fabian et al., 2001). However, in the limiting case of non Mg content 3/8 of the Al cations occupy tetrahedral sites and the spinel transforms into γ-Al_2O_3.

The melting point of spinel lies at about $\sim$2400 K at atmospheric pressure (Tropf and Thomas, 1991) which is even higher than for terrestrial corundum. Though, at the pressures which prevail in the atmospheres of AGB-stars (that is $\sim 10^{-8}$–10^{-10} bar), corundum reaches the stability limit prior to spinel, which then becomes stable $\sim$240 K below the limit of corundum. Therefore, in stellar winds a part of already existing corundum will convert into spinel by consuming Mg from the gas (Gail and Sedlmayr, 1998).

As mentioned above, spinel has a cubic crystal structure (see also Fig. 4.4) and is therefore optically isotropic. In the measurements which have been performed for this work we used a pure synthetic spinel plate (manufactured by SurfaceNet) with a diameter of 12.7 mm and a thickness of 0.1 mm. Like the corundum plate the spinel sample has polished surfaces. Optical data at high temperatures have been obtained already by Thomas et al. (1988) and Sova98. Thomas et al. (1988) have published absorption coefficients in the range of 2.5-10 μm for various temperatures up to 2000 K and a comparison of the results with the multiphonon model. Sova et al. (1998) measured the spectral emission of a pure spinel window over a wavelengths range of 2-12.5 μm at $\sim$2000K and compared their results with the combined model of multiphonon contributions to the classical dielectric function from Thomas et al. (1998). We have taken both low-temperature and high-temperature data, respectively at the temperatures 10, 100, 300, 551, 738, and 928 K (the high-temperature data are presented in Zeidler et al. (2013)). Additionally, we cover the whole wavelength range from 5 μm to 50 μm.

4.2.2. Reflection data and fit results

In Fig. 4.5 the reflectance spectra together with the respective fits at each measured temperature are shown. The fits are in very good agreement with the measured data.

For a normal, non-defective $MgAl_2O_4$ crystal, group theory predicts only four IR active oscillators (T_{1u} modes) whose TO-modes are located at around 15, 18, 21, and 33 μm (Thibaudeau and Gervais, 2002). However, the weak band at 43 μm as well as the weak shoulders at around

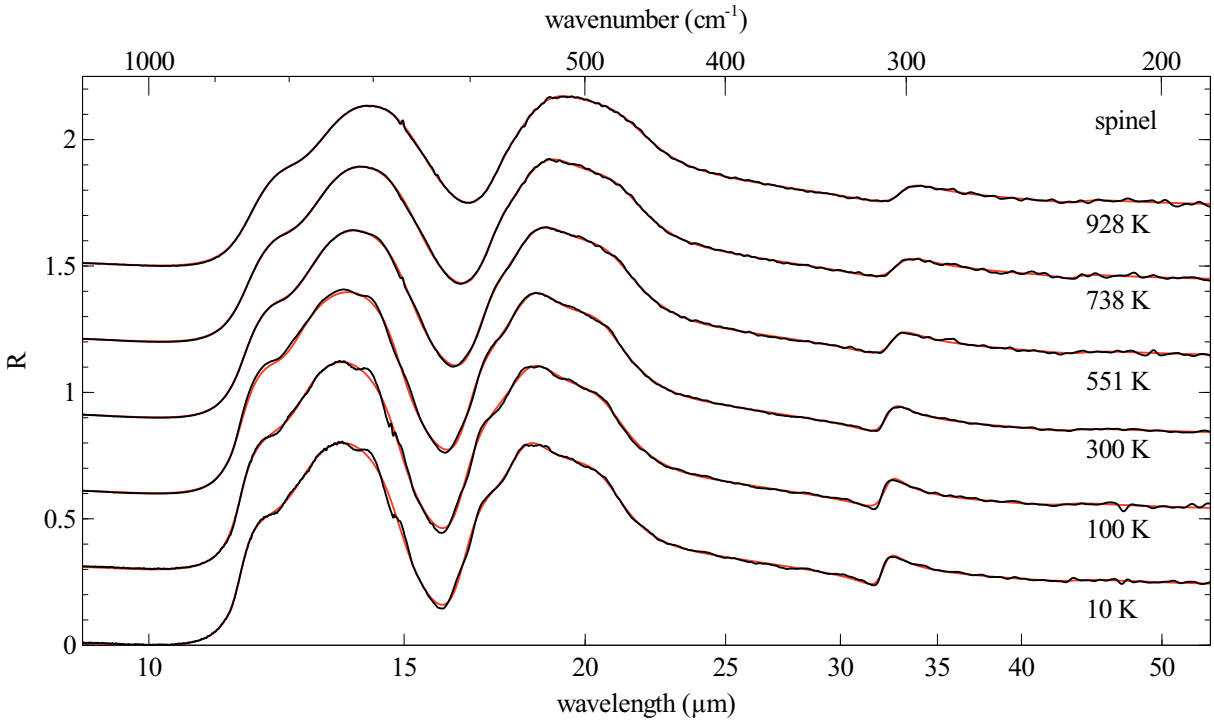

Figure 4.5.: Comparison of the reflectance spectra of spinel from 10 K up to 928 K with the respective fits. There is an additive offset of 0.3 between each spectrum for a clear view.

12 and 19 μm made it necessary to use eight oscillators for the fit procedure (see also Table A.2). These additional modes are forbidden by group theory but can be excited by the mentioned disordered cation distribution in synthetic spinels (Fabian et al., 2001) and by defects in the crystal lattice similar to the case of corundum.

Previous studies of reflection spectra of spinel also made use of additional modes beyond the four predicted ones. Fabian et al. (2001) used a classical Lorentz oscillator model and derived fits with eight oscillators in a wavelength range of 9-35 μm but did not treat the 43 μm feature. Therefore, they used an extra mode at 11.4 μm (S-mode) to fit a weak shoulder on the short-wavelength edge of the broad band between 11-15 μm which they link to the Al/Mg-ratio of their spinel samples and the filling of tetrahedral interstices by Al-ions. In our spectra we could not see any trace of such a shoulder. Thibaudeau and Gervais (2002) applied the FPSQ-model on their spectra with six oscillators. Based on their results, we added two more oscillators to the short- and the long-wavelength edge of the broad 19 μm band to fit the shoulder at 17 μm and the decrement toward longer wavelengths correctly. These extra oscillators have been already found in previous studies (Fabian et al., 2001; O'Horo et al., 1973; Preudhomme and Tarte, 1972) and might be due to the ratio of Mg/Al-cation disorder and defects, respectively.

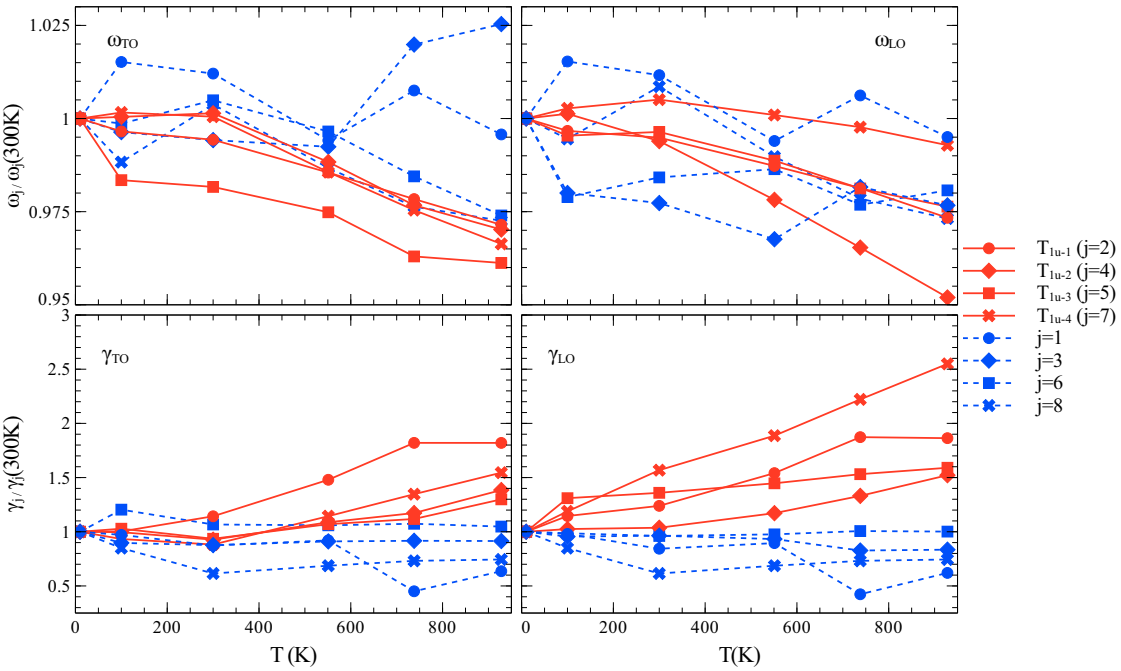

Figure 4.6.: Development of the oscillator parameter with the temperature for spinel. The presentation is similar to Fig. 4.3 but additionally, it is distinguished between the predicted modes for a perfect spinel (T_{1u}) and the added weak modes. The numbering of the modes is regarding to Table A.2.

4.2.3. Development of the fit parameters with temperature

In Fig. 4.6, the temperature development of the fit parameters is given. The presentation is similar to the one given for corundum but here it is additionally distinguished between the T_{1u} and the weak modes (the numbering is oriented on the corresponding *TO* vibration starting with the one at the lowest frequency). Also, all parameters are normalized to their respective value at 10 K. It is noticeable that only the T_{1u} oscillators, which are the strongest, show a relatively clear development with increasing temperature: at low temperatures, the temperature dependence for both frequency and damping is low while at high temperatures it becomes more and more a linear or even a quadratic dependence with the temperature similar to the case of corundum. Again, at high temperatures the frequency is shifting toward longer wavelengths (by a ratio of 1-5%) whereas the damping increases (by a factor of 1.25-2.5). It can be seen in case of the T_{1u-4} mode that the development with the temperature especially at low temperatures is not monotonic for all oscillators. For the T_{1u-4} mode, a maximal *LO* vibration frequency is reached at 300 K (increased by ∼0.5% compared to 10 K) while the damping of the *TO* vibration has a minimum at 300 K (5% below the value at 10 K). Such a behavior is reported already in Thibaudeau and Gervais (2002) for some other oscillators of spinel and might be due to the inverse character of our spinel sample. The weaker oscillators (indicated as $j = 1, 3, 6, 8$; see Table A.2 for the respective parameters) do not exhibit any distinct behavior which might be due to the fact that in general a fit with

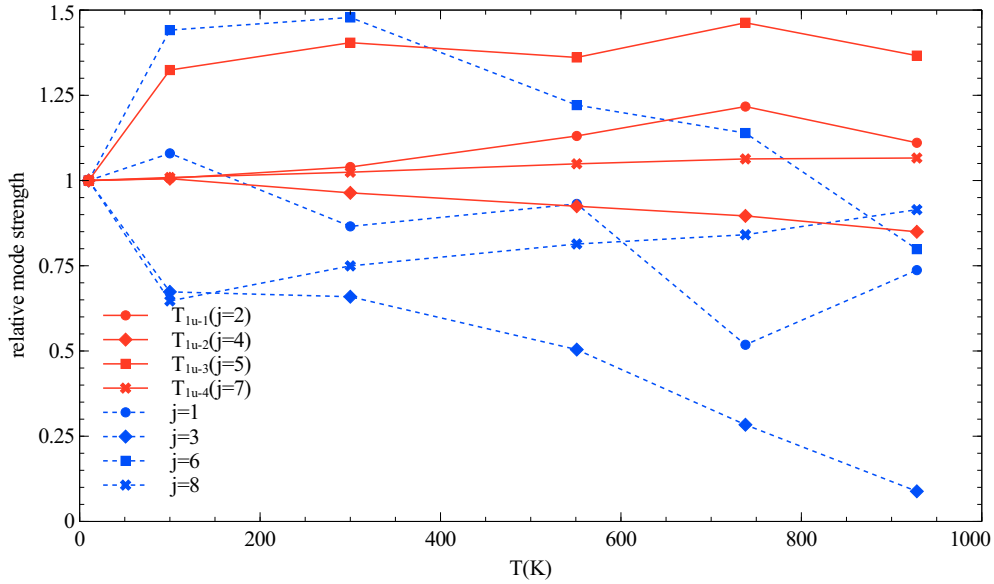

Figure 4.7.: Development of the strength of the spinel modes relative to its respective value at 10 K. Analogous to Fig. 4.6, it is distinguished between the predicted modes for a perfect spinel (T_{1u}) and the added weak modes.

weak modes is strongly depending on the quality of the measured spectra and thus somehow random. In general, the mode positions move toward longer wavelengths as it is expected whereas the damping keeps an almost constant value over the whole temperature range and even lowers for one of the modes to less than 50% of its value at 10 K.

In Fig. 4.7, the mode strengths, estimated by $\omega_{LOj}^2 - \omega_{TOj}^2$, are given relative to their respective value at 10 K. The strong modes (red) show in principle no significant dependence on the temperature, except the 'jump' of the T_{1u-3} mode from 1 to a value of 1.32 when reaching 100 K. This jump corresponds with a sudden increase of γ_{LO} of this mode when reaching 100 K and might be an effect of the fit procedure. Apart from this, the mean change of the mode strength is less than 20% for the strong modes. The weak modes (blue), however, show a general trend of a decreasing mode strength with increasing temperature. The mode indicated with $j = 3$ even seems to be almost vanished when reaching 928 K (compare also Table A.2). The strength of the mode $j = 6$ shows a similar jump like the T_{1u-3} mode at 100 K but is constantly decreasing toward higher temperatures. The strength of the weak mode $j = 8$ shows also a jump by reaching 100 K but to a value of 0.65. With increasing temperature, also the strength increases constantly to a value of 0.92 at 928 K. Thus, it is the only weak mode for which the mode strength has a trend to increase with increasing temperatures. It seems that with increasing temperature, the weak modes become hidden by the strong modes and thus seem to disappear. Interestingly, the fit procedure does not increase the damping for the weak modes but therefore decreases the strength. The trend of the weak mode $j = 8$ can be explained by the fact that this mode marks the boundary of the one-phonon excitations toward shorter wavelengths and can therefore hardly be hidden

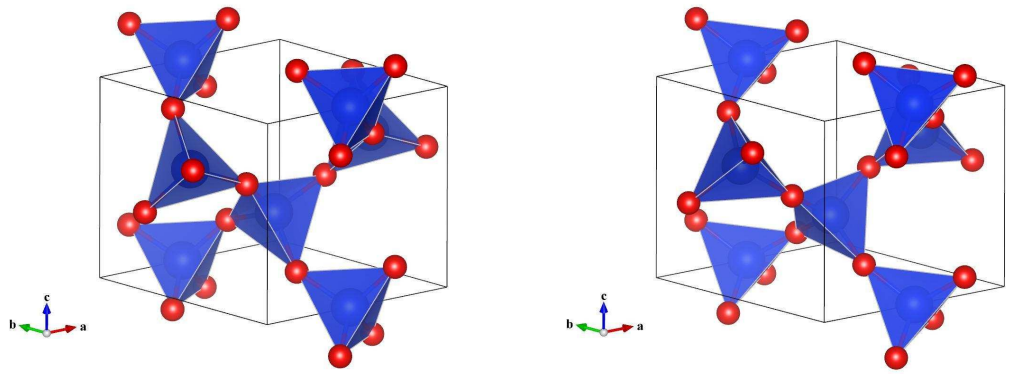

Figure 4.8.: Structure of the unit cells of α- (left) and β-quartz (right) made with VESTA. The silicon cations are the blue spheres whereas the oxygen is represented by red spheres. The whole crystal is made of $[SiO_4]^{4-}$–tetrahedra which are connected to each other by sharing all four oxygen anions with each another tetrahedron.

by the stronger modes.

Having a look on the development of ϵ_∞ as it is given in Table A.2 with the temperature, a relatively clear trend to increase from the value 2.64 to 2.77 with increasing temperature can be seen. The reasons might be similar to the case of corundum.

4.3. Quartz

4.3.1. Properties

Quartz is one of the three low-pressure phases of crystalline SiO_2, the other two are tridymite and cristobalite (see Fig. 4.9). At high pressures, there are three more phases of SiO_2, namely coesite, stishovite, and seiferite. In total there are ten of SiO_2 polymorphs (Klein and Hurlbut, 1999; Goresy et al., 2008). Quartz can be further divided into a lower-temperature lower-symmetry (α) and a higher-temperature higher-symmetry (β) modification.

α-quartz has a trigonal lattice structure. The unit cell contains 3 silicon and 6 oxygen ions. The silicon cations are tetrahedrally coordinated by 4 oxygen anions which creates the $[SiO_4]^{4-}$–tetrahedron, the basic structure of almost all silicates and silica polymorphs. Each oxygen anion is a part of two tetrahedra resulting in a three-dimensional grid of interconnected tetrahedra at which in each case three of them wind along a hypothetical axis parallel to the c-axis (see Fig. 4.8). Together with the coils before and after, a helix-like structure is formed that can be found for every set of interconnected tetrahedra along the c-axis. It should be noted that these structures have no particular influence on the chemical and physical behavior of the crystal, they are just a help for getting an imagination of the basic structure of α-quartz.

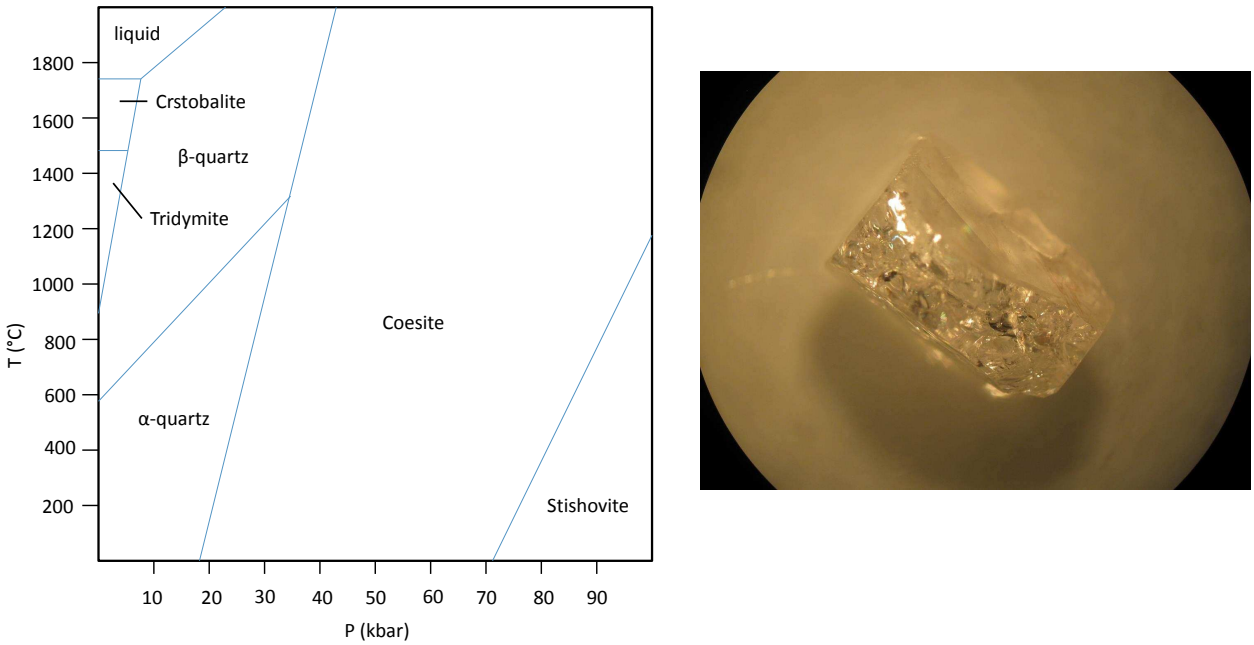

Figure 4.9.: Left: phase diagram of SiO_2. The temperature range in the presented measurements is from 25°-655°. Right: photograph of the quartz crystal that has been used for the measurements.

α-quartz turns to β-quartz at 846-847 K for atmospheric pressure by a displacive phase transition (Lakshtanov et al., 2007). β-quartz has a hexagonal lattice structure and the tetrahedra are ordered almost in the same way as for α-quartz but the alignment of the tetrahedra on their places has a higher symmetry in β-quartz than in α-quartz. By cooling down a quartz crystal in β modification, the opposite transition occurs and the α modification is formed.

Quartz has been the topic of many studies in the past, since it is one of the most important minerals on Earth and with its physical and chemical properties a very important material in science and technical applications. The first which examined the IR reflection properties of α-quartz with respect to classical dispersion theory were Spitzer and Kleinman (1961). They presented very comprehensive room temperature studies on natural and synthetic quartz crystals. Gervais and Piriou (1975) were the first which presented temperature-dependent IR reflection data of quartz. They fitted their data between 295 and 975 K with the in Sec. 2.3.3 introduced FPSQ model (Gervais and Piriou, 1974) and analyzed the changes of the band parameters with temperature especially in the range of the phase transition from $\alpha-$ to β-quartz. In the present work, we did IR reflection measurements on a natural α-quartz crystal from Brazil (see Fig. 4.9). The crystal has a maximum length, height, and width of 11, 7.5, and 8 mm, respectively. Energy dispersive X-ray (EDX) analysis did not reveal any impurities or non-stoichiometries. Because of the crystal structure, the interaction with light is anisotropic and like in the case of corundum one has to distinguish between polarizations parallel and perpendicular to the crystallographic c-axis. Because of the distinct hexagonal

shape of α-quartz crystals, we could easy make conclusions about the direction of the c-axis that lies parallel to the large natural grown surfaces of our crystal. Therefore, spectroscopic measurements parallel and perpendicular to the c-axis could be performed on on one of these surfaces. for measurement purposes, the crystal has been cut (10 mm×5 mm) and the surface for the measurements has been polished with diamond paste of 0.25 μm fineness.

4.3.2. Reflection data and fit results

The spectra of the quartz sample show relatively narrow but distinct bands as can be seen in Fig. 4.10 for the ordinary and the extraordinary ray, respectively. Theoretical calculations predict eight E- (E$\perp$c, ordinary ray) and four A_2-type (E$\parallel$c, extraordinary ray) modes to be IR active in α-quartz. In β-quartz, four E- and only two A_2-type modes should be IR active as analyzed by Scott and Porto (1967). The two A_2 species remain from the α–β-transition of quartz, the other two become forbidden. The same holds true for the E-modes but here the 'lost' modes in β-quartz become only inactive in the IR while they yet remain Raman active (Scott and Porto, 1967). The reflectance spectra have been fitted also with the aid of the FPSQ model although the features in the spectra are narrower than in the case of spinel and corundum. We used the FPSQ model mainly to keep the comparability with the data from Gervais and Piriou (1975) who did FPSQ fits to their high temperature measurements. In our data, we found seven E- and four A_2-type modes for temperatures below the transition point. The predicted eighth E-type mode should be found in a wavelength region around 78 μm that is however beyond our covered wavelength range and therefore has not been measured. The values of the fit parameters are quite consistent with data given by the literature (Scott and Porto, 1967; Gervais and Piriou, 1975) and the resulting fits are very accurate to our measurements (see Fig. 4.10).

By reaching 928 K for the ordinary ray it can be clearly seen that the features at 8.2, 14, 25, and 37 μm (mode number 7, 4, 2, and 1; from top to bottom in Table A.3) disappeared. According to Scott and Porto (1967) these are the four modes which should become IR inactive by the transition to β-quartz. Already at 833 K, the modes 7, 4, and 1 became very weak so that there is almost no evidence for their existence in the spectrum. In the extraordinary ray, the spectra also show the transition to β-quartz. Here, modes at 26 and 13 μm wavelength (number 1 and 3) disappeared by reaching 928 K as predicted by theory. In a very good manner, these results correspond to the data taken by Gervais and Piriou (1975) which have comprehensively investigated the phase transition of quartz with IR spectroscopy between 7.7 and 33.3 μm. At this point, the presented measured data complement their study with data about the temperature development of the E-type mode at 37 μm that has not been treated in their work.

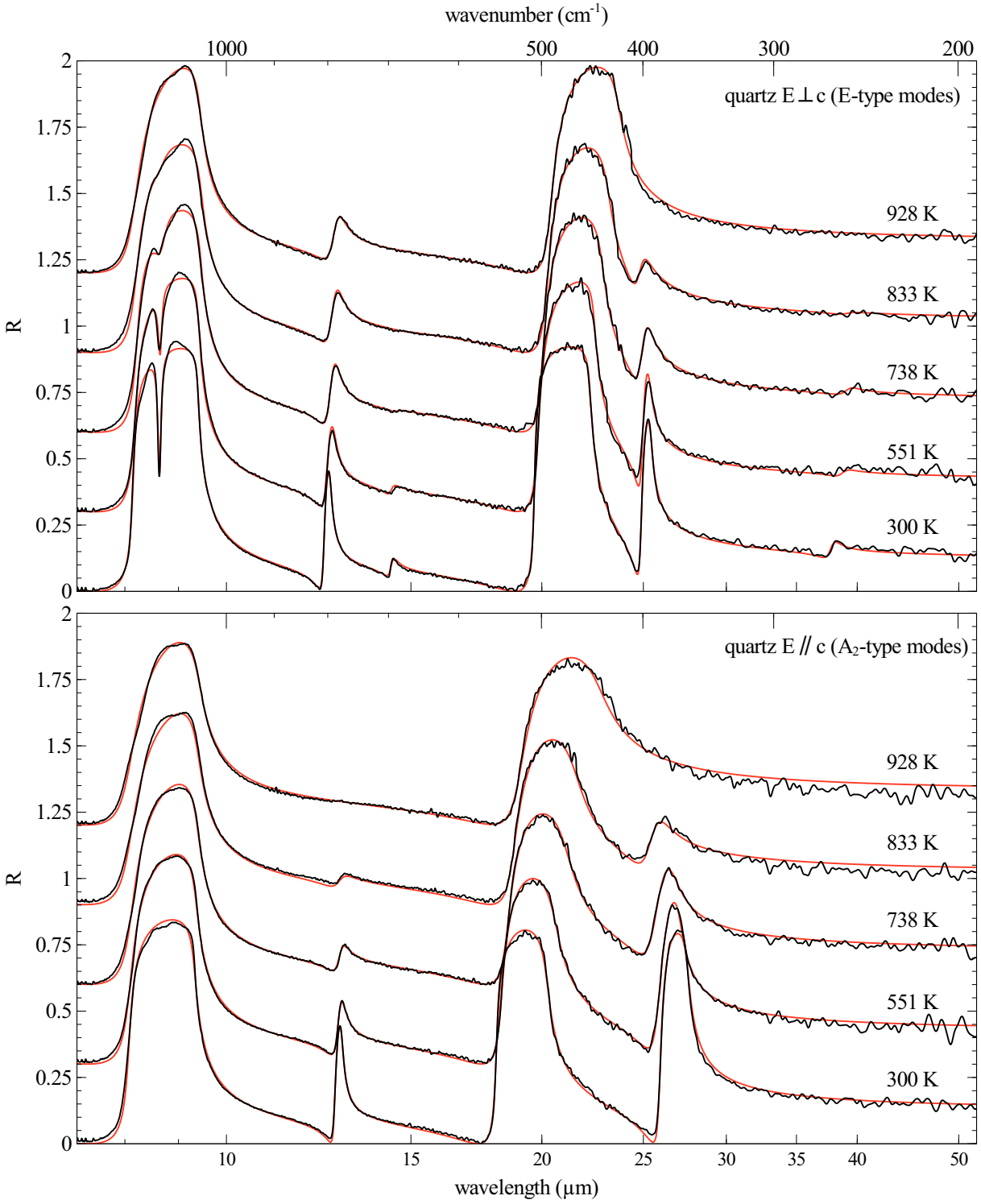

Figure 4.10.: Reflectance spectra at five different temperatures and the respective fits for the quartz crystal. Due to the phase transition from α- to β-quartz, some distinct features in the spectra at temperatures <928 K, totally disappeared in the spectrum at 928 K. An additive offset of 0.3 is set between each spectrum.

4.3.3. Development of the fit parameters with temperature

For those modes which do not disappear by the transition from α- to β-quartz, the development with the temperature, relative to their respective value at 300 K is given in Fig. 4.11. The numbering of the modes again corresponds to their appearance in the spectra starting at long wavelengths. Obviously, the development with the temperature follows not a linear function for most of the modes which holds true especially for the A_{2-2}- and the E_3-type mode (corresponding features at 21 and 22 μm wavelengths, respectively). This is contrary to the mode development of corundum and spinel in that temperature range where a linear rather than a quadratic dependence has been found. Additionally, the dependence on the temperature is stronger for TO frequencies (maximal deviation at 833 K from the value at 300 K is 6% while for LO frequencies it is 3.5%). Apparently, the individual curves follow a smooth development also at the point of the phase transition (indicated by dashed lines in the figure) but actually, as shown by Gervais and Piriou (1975), toward the point of transition the development of the mode frequencies is exponential (owing to a break of the thermal expansion) which can not be shown in particular in the figure due to a lack of data in that range but which can at least be reconstructed for lower temperatures. However, the lines that combine the points at 833 K with those at 928 K should be treated carefully since they do not represent the real development of the mode frequencies in that range. Nevertheless, for temperatures below the point of transition, the development is well represented by the combining lines and consistent with the data of Gervais and Piriou (1975). It is interesting to note that the modes at longer wavelengths (e.g E_3) show a stronger dependence on the temperature than the modes at shorter wavelengths (e.g. E_6; corresponding feature at 9 μm). This point will be further discussed at the end of this chapter. For the damping, no significant changes in the temperature development could be observed which is likely due to the lack of data around the point of transition. Therefore, the damping will be not discussed.

An interesting development with the temperature is also shown by the relative mode strength, given in the lower diagram in Fig. 4.11. For temperatures below the point of transition, the dependence of the mode strength on the temperature is relatively weak (in maximum $\sim$12% at 833 K for the A_{2-2}-type mode) for all modes, except E_6. The E_6-type mode follows a nearly quadratic temperature dependence down to 60% of its value at 300 K. By passing the point of transition, the strengths of the E-type modes show completely different developments. At 928 K, the strength of the E_6-type mode suddenly increases to 157% relative to its value at 300 K. The E_3- and E_5 (12.5 μm)-type modes decrease to 80 and 13%, respectively. The A_2-type modes do not show such a strong change in the development of their strength. They keep their monotonic increase with the temperature.

For a good fit performance, ϵ_∞ had to be kept at a constant value of 2.38 at 551, 738, and 833 K for the E$\|$c polarization. Therefore, no statement about the particular development

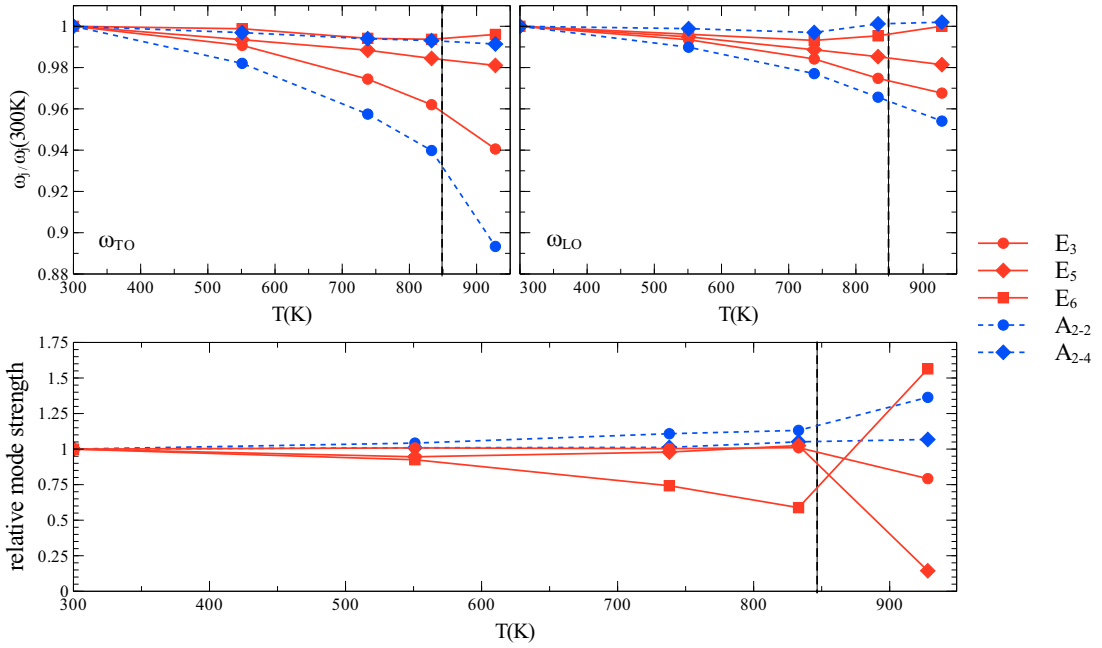

Figure 4.11.: Top panel: development of the mode frequencies ω_{TO} and ω_{LO} of quartz which 'survive' the phase transition with the temperature, in both polarizations: E⊥c (E-type modes, red) and E∥c (A_2-type modes, blue). Bottom: development of the mode strengths with the temperature. All values are given relative to their respective value at 300 K. The dashed line indicates the phase transition temperature. The numbering of the modes is regarding to Table A.3.

can be given. For the E⊥c polarization of α-quartz, ϵ_∞ is increasing with increasing temperature from 2.34 to 2.39 at 833 K. In the β phase, values of 2.36 and 2.44 for the polarizations E⊥c and E∥c, respectively, could be found.

4.4. Olivine

4.4.1. Properties

Olivine is, together with pyroxene, the most abundant crystalline silicate in space. Its prominent bands are observed in many spectra of accretion disks around young stars and in the outflows of AGB stars (Henning, 2003a,b). Olivine also occurs in our solar system in the form of cometary dust (Hanner, 2003), as interplanetary dust particles (Bradley, 2003), and on planetary surfaces (Hartmann, 2005) and has the general sum formula $(Mg,Fe)_2SiO_4$ with its Mg end member forsterite and the more rare Fe end member fayalite. On Earth, olivine is the most abundant material in the upper lithosphere. In general, more Mg–rich and less Fe–rich olivines are found. Olivine belongs to the group of the nesosilicates (island–silicates) and crystallizes in orthorhombic symmetry with isolated $[SiO_4]^{4-}$ tedrahedra surrounded by metal cations (mostly Fe^{2+}, Mg^{2+}), each in coordination to six oxygen atoms. There are two

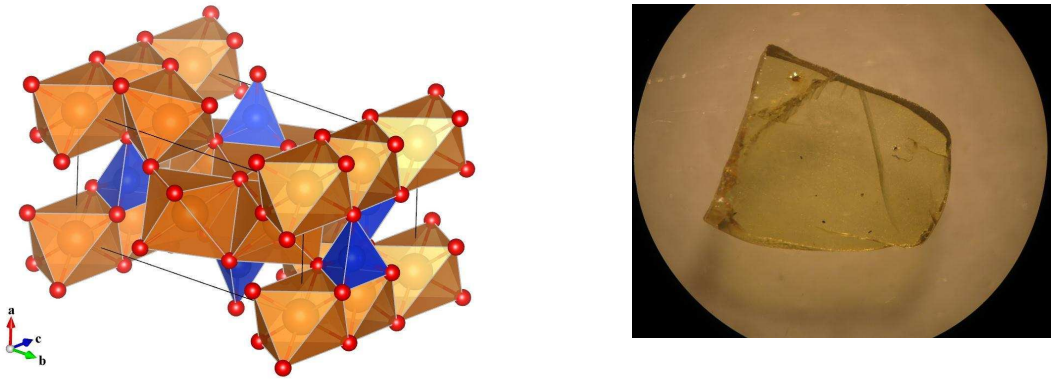

Figure 4.12.: Left: Sketch of the principal structure of the unit cell of forsterite (Mg_2SiO_4) made with VESTA. The blue, isolated tetrahedra represent the $[SiO_4]^{4-}$ component whereas the bronze octahedra represent the Mg–O bonds (oxygen: red spheres). Right: photograph of sample D1, view onto the c–b–plane.

different types of these coordination, both slightly distorted from the octahedral symmetry. One is centrosymmetric and elongated along one of the O-O axes (such cation sites are called 'M1'), and the other is non–centrosymmetric and irregular (the cation sites in this coordination are called M2 (Burns, 1993)).

Especially when Fe is a constituent of the crystal lattice, olivine is not by implication a stoichiometric compound. Since the sum formula is based on Fe^{2+} cations only, the existence of cations in different oxidation states (Fe^{3+}, Fe^{4+}) leads to voids within the oxygen lattice which realizes the charge equalization.

Olivine crystals usually have a greenish to yellowish color, which can turn into brown when it contains traces of Fe^{3+} ions. The greenish coloring is caused by crystal field bands of Fe cations around 1 μm wavelength, leading to an increased opacity for red light and an increased transmittance of yellow and green light. The brownish coloring comes from charge transfer processes between Fe cations in different oxidation states which lead to increased absorption throughout the visible wavelength range towards the ultraviolet. As stated in Zeidler et al. (2011), the strength of the crystal field bands is directly related to the amount of Fe cations in the lattice (see also chapter 5).

In the past, several temperature dependent reflection and absorption measurements on olivine in the IR have been done. Suto et al. (2006) have taken low-temperature reflection data of a single forsterite crystal down to 50 K and fitted the curves with a Lorentz oscillator model in a wavelength range from 8 - 100 μm. Koike et al. (2006) measured the absorption of small particles of synthetic forsterite and fayalite, and a natural olivine (San Carlos) with ∼10% Fe^{2+} in a wavelength range of 9 - 100 μm and for temperatures down to 8 K. Fabian et al. (2000) presented optical constants of an olivine single crystal from Austria with a relative Fe^{2+} content of 5%. Here, for the first time, temperature dependent

reflectance data and optical constants (n, k) of a similar olivine for temperatures higher than 300 K are presented.

For the measurements in the IR, we have used two crystal platelets of olivine from San Carlos (Arizona, USA), denominated as C1 and D1 and with the respective thicknesses of 1410 μm and 1115 μm, respectively. These samples were used already in the measurements of Zeidler et al. (2011) and are also used for the transmission measurements which are presented in this work (see chapter 5). They have been cut along the a–c- (C1) and c–b-plane (D1), respectively, whereas the orientation has been proven by X-ray diffraction[4]. Additionally, the surfaces of the crystals have been polished with diamond paste (0.25 μm fineness) to reduce diffuse reflection. The stoichiometry the San Carlos olivines has been determined by EDX analysis to $Mg_{1.72}Fe_{0.2}SiO_4$.

4.4.2. Reflection data and fit results

The results of the reflection measurements for both crystals C1 and D1 and all three polarization directions, directly compared with the respective best fits at four different temperatures are shown in Figs. 4.13. Apparently, the decrease in the intensity with increasing temperature leads to a disappearance of some of the features or even a merging with other ones. For example, the weak features in the 300 K spectra of the E‖c polarization (B_{3u} modes) of the D1 crystal at around 18 and 21μm cannot be seen anymore in the spectrum at 928 K. The same holds true for the feature at 20μm in the E‖b spectra (B_{2u} modes) or the feature at around 21μm in the E‖a spectra (B_{1u} modes) of the C1 crystal.

In case of forsterite, group theory predicts 35 modes to be IR active (Iishi, 1978). We could resolve 28 and 29 modes, respectively (depending on the sample) which is three and two modes less than presented in Fabian et al. (2000). For the fit procedure, we have used the Lorentz oscillator model given by Eq. (2.38) instead of the FPSQ model since the spectral reflection features of olivine are narrow enough to get a good fit result also with only three free parameters. Again, all fit parameters can be found in appendix A, in Table A.4.

For the E‖a spectra, we found 8 modes (B_{1u}) including the small but distinct band at the short wavelength side of the strong 10 μm feature. While the latter is due to an asymmetric stretch vibration of the $[SiO_4]^{4-}$ tetrahedra (Fabian, 2002), the former has no equivalent in the theoretical predictions on the modes of forsterite. This feature has been indicated as an overtone (two-phonon absorption) of the 20 μm vibration mode by Fabian et al. (2000). However, it seems that it becomes slightly weaker with increasing temperature whereas the damping increases. The weak mode at 24.8 μm (403 cm^{-1}) appears only as a shoulder of the 24.2 μm feature in the reflectance spectra at 300 K. The E‖b polarization has been fitted with

[4]I'm grateful to Dr. Wehrhan who did the orientation in the Institute of Quantum Optics of the university of Jena.

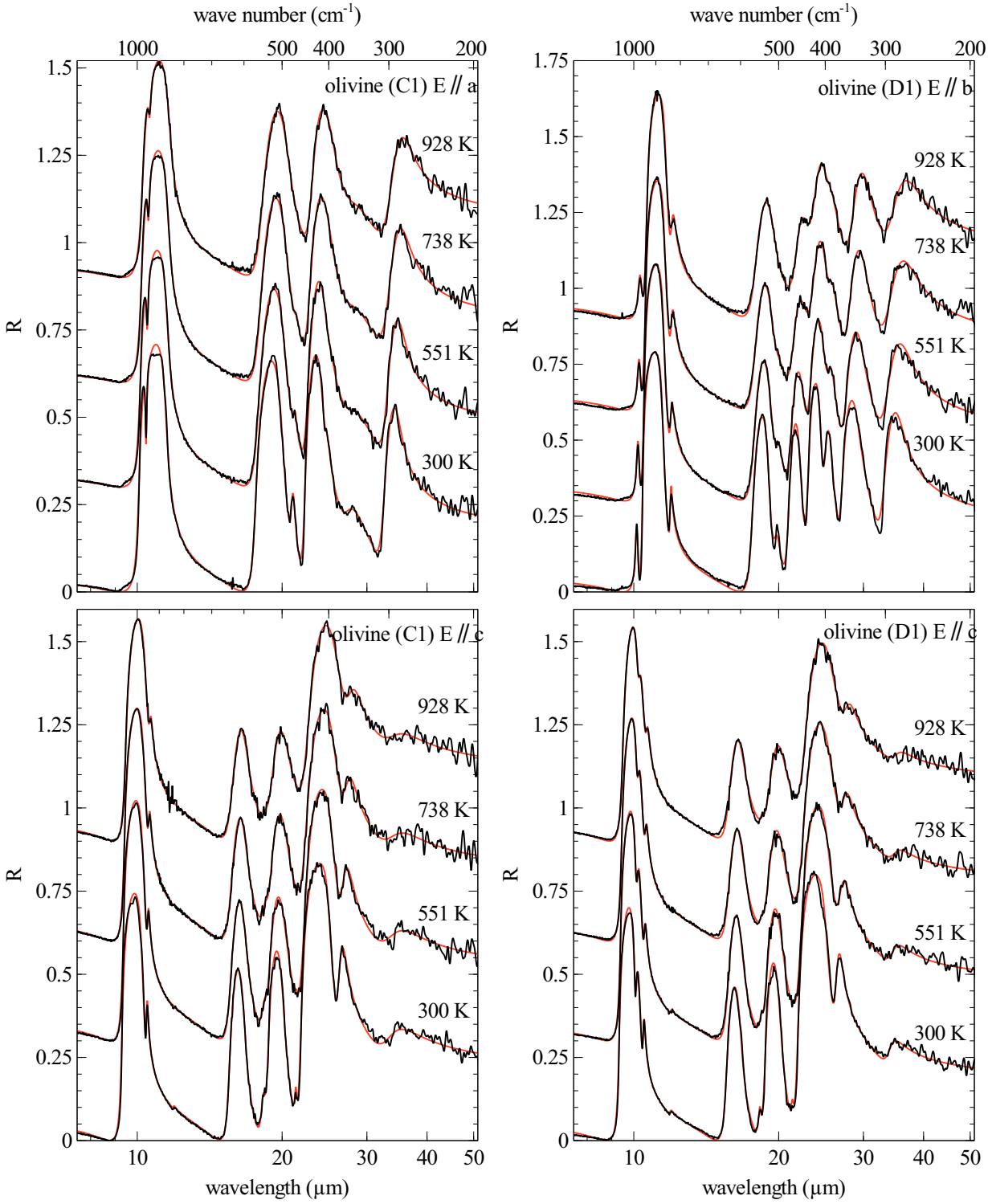

Figure 4.13.: Comparison of the measured reflectance spectra of the polarizations E||a (sample C1), E||b (sample D1), and E||c (C1 and D1) with the respective best results of the fit procedure. For all diagrams, between the spectra an offset of 0.3 has been added.

10 oscillators (B_{2u}-type modes). 13 modes have been found in the theoretical calculations of Iishi (1978). There, one mode should be at $\sim$69 μm (144 cm^{-1}) which is beyond our covered wavelengths range. The two other modes are very weak and should have their excitation frequencies at $\sim$45 and $\sim$35.7 μm (224 and 280 cm^{-1}), respectively, which cannot be confirmed in our case because of strong noise in that range[5]. The E$\|$c polarization for the D1 crystal could be fitted with 11 oscillators (B_{3u}-type modes). 13 modes have been found by the measurements of Fabian et al. (2000) and by the calculations of Iishi (1978). Again, three modes could not be resolved from our spectra due to noise but instead we discovered a small feature at $\sim$10 μm (996 cm^{-1}) which again could be an overtone. But interestingly in the same polarization of the second sample (C1) this feature cannot be seen in the respective spectra. The small 10μm feature in the sample D1 is yet too strong to explain its non-existence in the sample C1 by noise and if it is an overtone than it must appear also in the spectra of C1. Since the other polarization in D1 is E$\|$b, one might think that a non-perfect polarization might be responsible for this feature but other features that could belong to the E$\|$b polarization were not found in the E$\|$c spectra of D1.

In the Fgs. 4.14 and 4.15, the from the oscillator parameters (given in Table A.4) calculated optical constants n and k are presented. They have been calculated for the temperatures 300 and 928 K. For convenience, n and k in E$\|$c polarization are only calculated for the C1 sample. Both, n and k, show a shift of their features toward longer wavelengths with increasing temperature while the width is increasing and the maximum values of the features are decreasing. The positions of the features of k are equal to the respective oscillator frequencies found by the fits. In general, the temperature related decrease of the maximum values for k of all modes is relatively uniform. Comparing the maximum values at 300 K with those at 928 K, we estimated a mean decrease of roughly 33%. Obviously, the temperature dependent shift is stronger for modes at longer wavelengths than for modes at shorter wavelengths (e.g. in E$\|$a polarization, the shift for the mode at 11.4 μm wavelength is $\sim$0.1 μm while for the mode at 34.3 μm it is $\sim$1 μm). Many weak modes seem to be merged with neighboring strong modes at 928 K. E.g. the weak 21 and the strong 19.8 μm features at 300 K merge to a single feature at 20 μm by reaching 928 K. Therefore, it is difficult to give quantitative statements for the broadening only from the spectra. However, in the k spectra, distinct single modes broaden roughly 20 to 40% whereas it seems that the relative broadening is independent from the spectral position of the modes. The 300 K data correspond quite well with those for the olivine from Austria presented in Fabian et al. (2000). Small differences appear in the maximum value of k in some of the B_{1u}- and B_{2u}-type modes (e.g. the B_{2u} modes at 28.7 and 35 μm wavelengths are roughly 20% less intensive while the mode at 11.4 μm is 18,% more intensive than in Fabian et al. (2000)).

[5]Due to the small diameter of the hole in the sample holder, the noise for low intensities and long wavelengths became quite high.

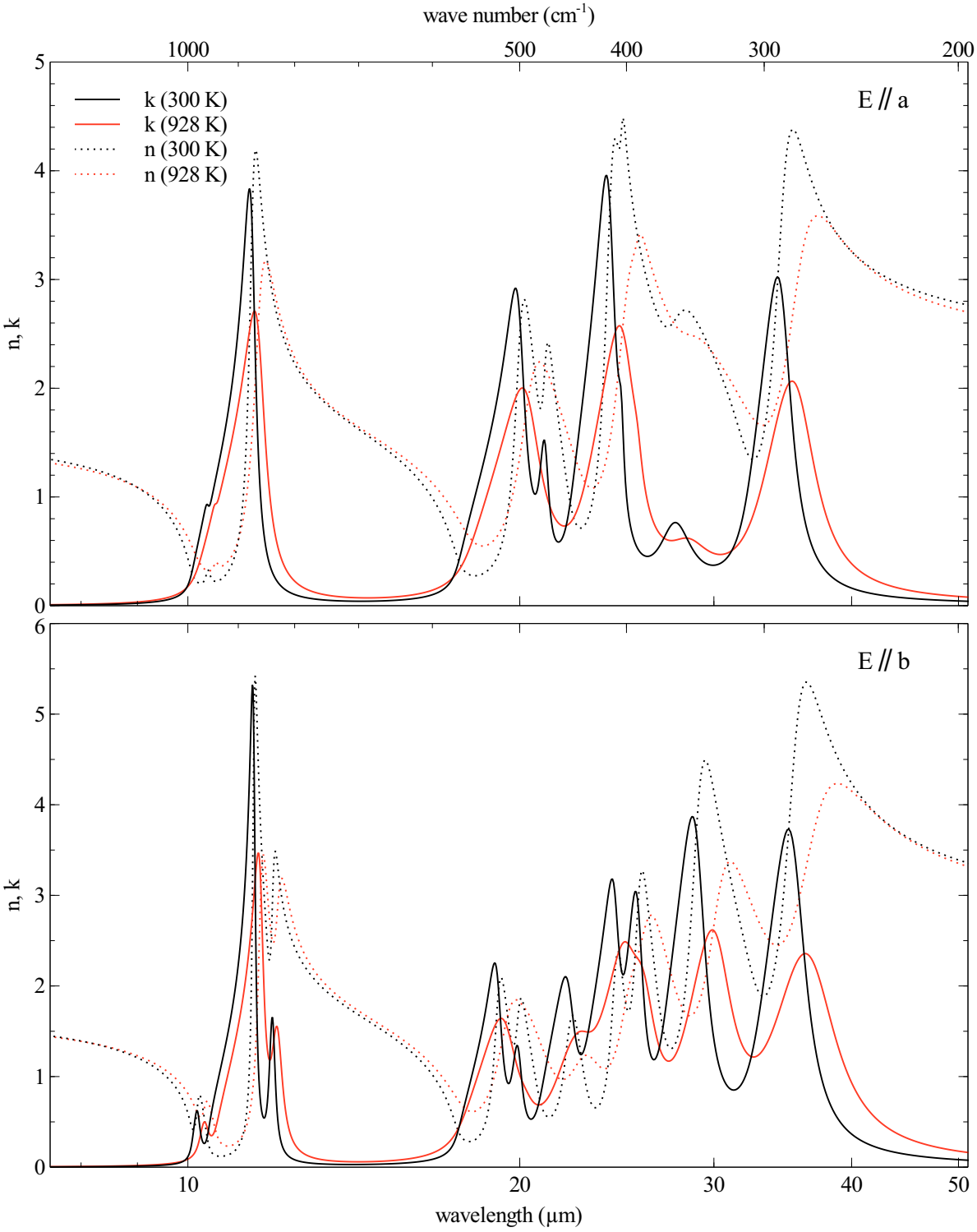

Figure 4.14.: Calculated optical constants n and k for the polarizations E‖a (B_{1u}-type modes) and E‖b (B_{2u}-type modes) from the samples C1 and D1, respectively, at two different temperatures.

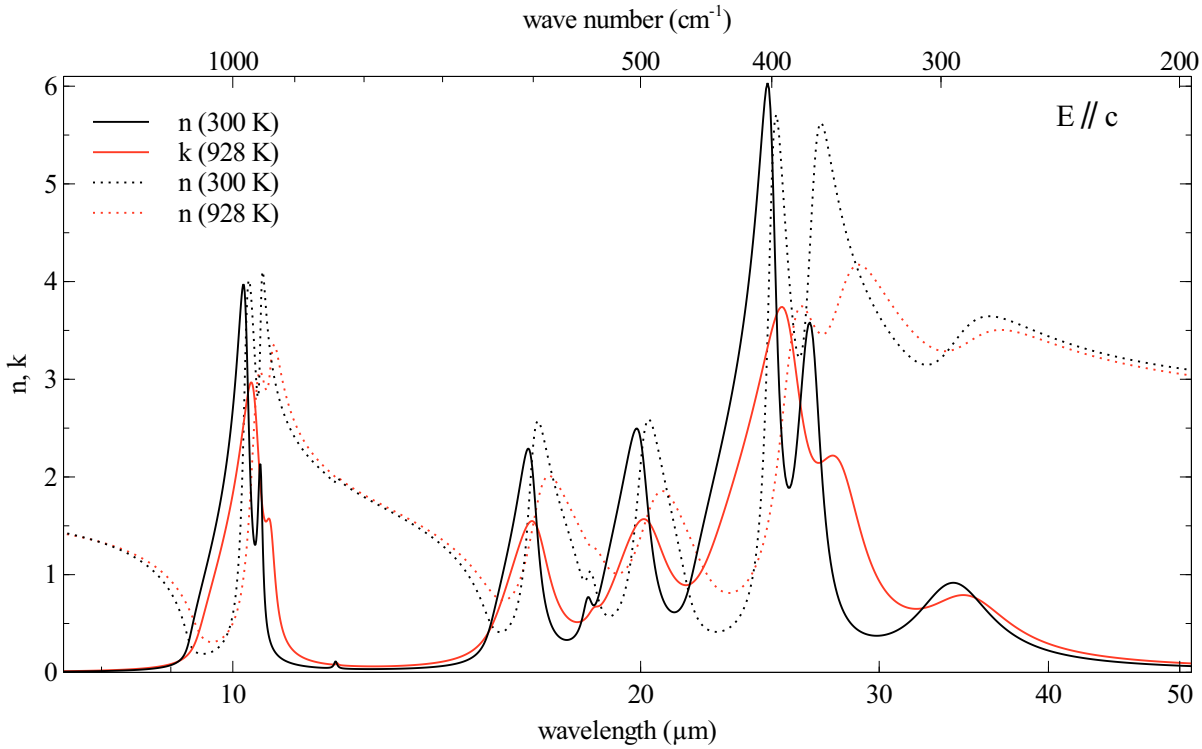

Figure 4.15.: Calculated optical constants of the E‖c (B_{3u}-type modes) polarization of the sample C1 at two different temperatures.

4.4.3. Development of the fit parameters with temperature

Exemplarily for the other polarizations, in Fig. 4.16 the temperature development of the oscillator parameters for the modes in the polarization E‖c (C1) are presented. The spectra could be fitted with 10 oscillators where three of them are extremely weak (indicated by dashed lines in the figure). Analogous to the presentations of the oscillator parameters for corundum and quartz, they are given relatively to their respective value at 300 K (for the absolute values see also Table A.4). The numbering of the modes corresponds to their spectral position from long toward short wavelengths. As can be seen, the frequency shift decreases almost linear with the temperature and ranges from almost 1 for the (very weak) mode $j = 4$ (21.4 μm wavelength) to roughly 0.95 for $j = 2$ (26.9 μm). Also almost linear with the temperature is the development of the damping. In principle, the damping increases with increasing temperature for all modes. The relative damping terms reach values from 1.05 to 2.6 at 928 K. The lowest dependence with the temperature shows the damping of the mode $j = 1$ (34 μm), the highest shows the damping of the mode $j = 3$ (25 μm). The linear dependence of both the frequency and the damping, hints for a domination of cubic terms in the anharmonic contributions of the corresponding Hamiltonian (Gervais and Piriou, 1974; Maradudin and Fein, 1962; Ipatova et al., 1967). The relative strength of the modes, given in the lower diagram of Fig. 4.16, shows a minor, linear dependence on the temperature for most of the modes. We excluded the very weak modes $j = 4$, 6 (18.3 μm), and 8 (11.9 μm) from

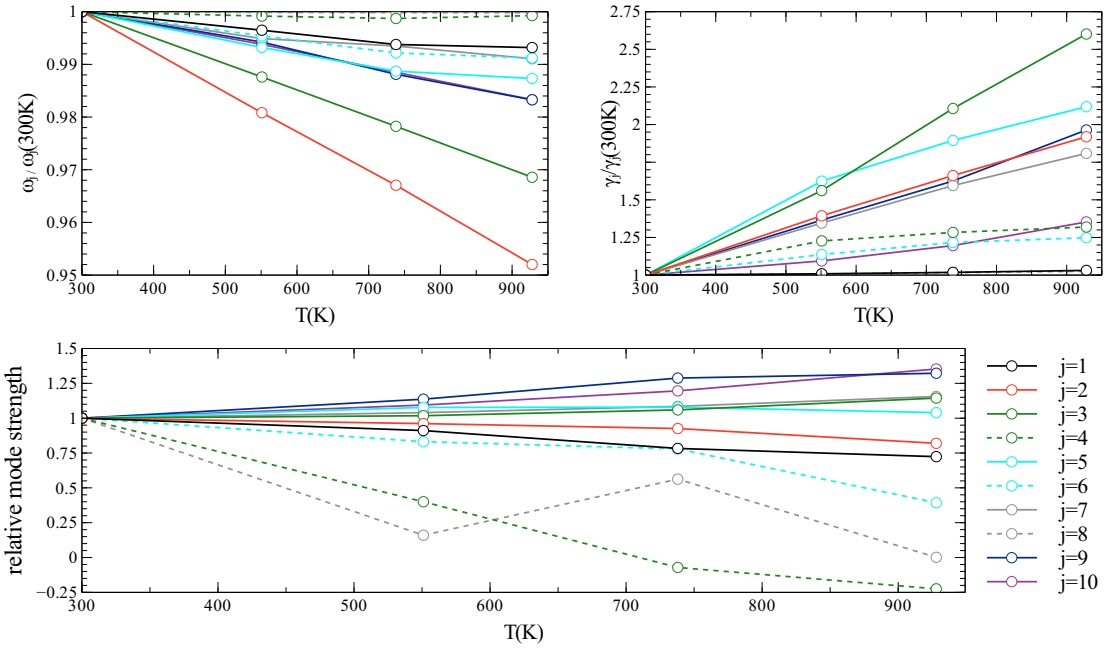

Figure 4.16.: Top panel: development of the mode frequencies (ω_{TO}) and the damping (γ_{TO}) of the olivine sample C1 for the polarization E||c with the temperature. Bottom: development of the mode strengths with the temperature. All values are given relative to their respective value at 300 K. The numbering of the modes is regarding to Table A.4

the analysis since the fits of these modes are not unambiguously. The relative change of the values of the other modes by reaching 928 K ranges from 0.74 to 1.36. No general tendency toward increasing or decreasing values can be seen so that the mean relative mode strength can be seen as almost constant. The minor dependence on the temperature indicates that the difference between ω_{LO} and ω_{TO} for each mode does not change too much over the whole temperature range.

4.5. Enstatite

4.5.1. Properties

Enstatite belongs to the group of the inosilicates (chain-silicates) and is the magnesium end member of the magnesium-iron(II)-pyroxenes which have the general formula $Mg_xFe_{1-x}SiO_3$. Enstatite itself has the sum formula $MgSiO_3$ but even when Mg is exchanged by a small content of Fe^{2+} of <10% the pyroxene can still be called enstatite (Matthes, 1990). Contrary to olivine, pyroxenes can have two different crystal structures depending on the conditions of condensation: a monoclinic (*clinopyroxene*) and an orthorhombic (*orthopyroxene*) crystal structure. In nature, Mg-orthopyroxenes are much more abundant than Mg-clinopyroxenes (Matthes, 1990).

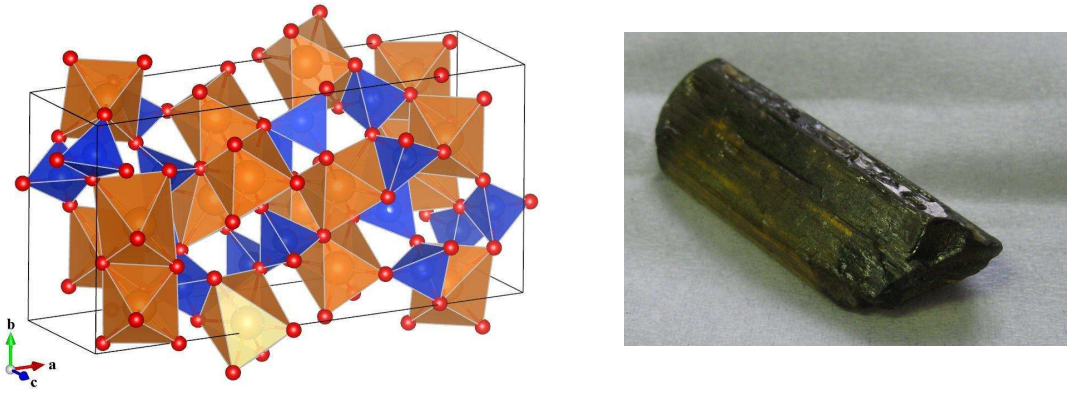

Figure 4.17.: Left: Sketch of the principle structure of the unit cell of enstatite ($MgSiO_3$). As in Fig. 4.12, the blue tetrahedra represent the $[SiO_4]^{4-}$ and the bronze octahedra the $[MgO_6]^{10-}$ components. The $[SiO_4]^{4-}$ tetrahedra built infinite chains along the c–axis. The same holds true for the 'M1–octahedra' but not for the 'M2–octahedra' with less regularity. Right: picture of the enstatite crystal from Burma before the preparation for the measurements.

Orthoenstatite is characterized by $[SiO_4]^{4+}$ tetrahedra which share two oxygen anions with two other tetrahedra. Out of these bonded tetrahedra, a chain along the crystallographic c axis is created (chain silicates). Three vertices of the $[SiO_4]^{4+}$ tetrahedron define a plane that is almost parallel to the plane created by the crystallographic axes b and c (Demichelis et al., 2012). On the other side, the metal cations form two differently distorted octahedra together with the oxygen anions (the two possible sites of the metal cations are denominated M1 and M2 like in the case of olivine). M2 has less regularity compared with M1 (Demichelis et al. (2012) determined the Mg–O distances in M2 to be in a range from 1.99 to 2.46 Å, while in M1 the distances are ranging from 2.01 to 2.16 Å). The M1 octahedra share an equally used edge and form also chains along the c axis whereas each M2 octahedron shares three edges with three different M1 octahedra but none with another M2 octahedron. Since clino- and orthoenstatite have a very similar IR spectrum and clinoenstatite is hardly available as a natural single crystal, we have focused on orthoenstatite for the measurements.

Like olivine, enstatite is a very abundant mineral in space (Molster and Waters, 2003). Its spectral features have been detected in many PPDs around Herbig Ae/Be stars (Juhasz et al., 2010) but also in the outflows of AGB stars (Molster and Waters, 2003). It is thought that clino- and orthoenstatite are relatively equal abundant in space but for some stars with a very high mass loss rate orthoenstatite seems to be more abundant (Molster and Waters, 2003). Juhasz et al. (2010) found that enstatite in PPDs exists rather in the inner and hotter part of the disk whereas forsterite is more abundant in the outer and cooler parts. This outcome is contrary to the predictions made by Gail (2003) who stated that the abundance of enstatite in a chemical equilibrium is increasing with increasing distance to the

host star. Juhasz et al. (2010) claimed that their finding must be due to a non-equilibrium formation of crystalline silicates in a PPD and proposed annealing via shock-heating in the mid-plane of the disk although this process would not explain the enstatite abundance there. More information about the IR features of enstatite at different temperatures would give help in understanding the distribution and the formation of enstatite in PPDs.

One of the first who did low temperature spectroscopic measurements on enstatite in an astrophysical context was Day (1976). He compared the IR absorption spectra of grains at RT of both olivine and enstatite with their respective spectra at 80 K and found that the absorption features in the 20 μm wavelength range increase more than four times stronger than the features in the 10 μm wavelength range but he did not measure the size of the enstatite particles and therefore scattering could have influenced his findings. More recently Chihara et al. (2001) and Bowey et al. (2001) did low temperature spectroscopic absorption measurements on small grains and thin films of enstatite, respectively. Both authors were especially interested in the absorption features in the far-IR to sub-mm wavelength range (20–100 μm and 15–85 μm, respectively) of ortho- and clinoenstatite. Low-temperature mass absorption coefficients of enstatite annealed from amorphous precursors have been taken by Murata (2009) in the wavelength range 15–100 μm. However, as in the case of olivine, high temperature spectroscopic measurements of the reflectance in the IR have apparently not been done so far.

For the measurements, we have used a single (ortho-)enstatite crystal from Burma purchased from a commercial mineral dealer ("Crystal-Treasure") (a picture of it can be seen in Fig. 4.17) with the stoichiometry $Mg_{0.92}Fe_{0.09}SiO_3$, as found by EDX analysis. Because of the orthorhombic symmetry of enstatite, we had to take spectra for polarizations parallel to all three crystallographic axes a, b, and c. Since it is given already by the direction of growth of the crystal, the c-axis was easy to identify and determined by visual judgment. Therefore, we cut the crystal perpendicular to the determined c-axis into two pieces, a small one (ca. 10×5×5 mm) and a bigger one (20×10×5 mm). Perpendicular to the c-axis, the axes a and b can be found (orthorhombic symmetry) which could be identified by IR spectroscopic analysis with a polarizer and comparison of the polarized reflectance spectra with data given by Demichelis et al. (2012). The a–b-plane of the big piece, by the cutting obtained, and the planes of the small piece have been polished with diamond paste (0.25 μm fineness). Due to the polishing of the planes containing c-axis, the existing a–b-plane of the small piece were not used for the high-temperature measurements because the diameter of the surface just became smaller than the diameter of the hole in the used sample holder ring of the HTHP cell.

As in the case of spinel, also low-temperature measurements of the IR reflectance were done. Therefore, the small crystal were used for all measurements in all orientations since the big crystal fits not to the sample holder of the cryostat. The crystal and the reference gold

mirror were fixed on the sample holder of the cryostat with an aperture of 3 mm diameter, for measurements on the a–b-plane, and with an aperture of 6 mm, for measurements on the plane containing the c-axis. Measurements have been taken at 200, 100, an 10 K. In case of the polarization E‖c , we were able to perform measurements at wavelengths longer than 60 μm, owing the bigger aperture. Therefore, we decided to enhance the wavelengths range for the measurements of the polarization E‖c to 90 μm in order to get knowledge about the development of the 70 μm feature of enstatite that shows up in this polarization.

4.5.2. Reflection data and fit results

In Figs. 4.18 and 4.19 the measured reflectance spectra at seven different temperatures in a wavelength range 7.5–60 μm and 7.5–90 μm, respectively, are shown in comparison with the result of the respective fit. Enstatite has a lot of relatively narrow IR features. Group theory predicts all in all 87 modes which should be IR active. For the possible polarizations E‖a, E‖b, and E‖c, $29B_{2u}$, $29B_{3u}$, and $29B_{1u}$ modes should exist, respectively (Demichelis et al., 2012). In this study 24, 18, and 20 modes could be found for the three different polarizations. Four predicted modes are not in the covered wavelengths range. Demichelis et al. (2012) have measured the reflectance of a synthetic enstatite crystal ($MgSiO_3$) in the wavelength range 8–100 μm and found for the different polarizations 22, 22, and 21 modes, respectively. They have fitted their results with a Lorentz oscillator model and compared the parameters with the theoretical predictions. We have taken the predicted values as presented in Demichelis et al. (2012) as initial parameters for the fit procedure of the visually recognized modes. The fit model was again the Lorentz oscillator model since the huge amount of small and relative distinct features indicated that the damping parameter for *LO* modes differs not significantly from those for the respective *TO* modes. A fit with the FPSQ model has been tried also for the 300 K spectrum of the E‖a polarization but no relevant differences to the Lorentz model could be found.

As can be seen from the figures, some weak spectral features seem to disappear: the B_{3u} (E‖b) modes 2 and 14, at 41.8 μm (10 K) and 13.4 μm (10 K) wavelength, respectively; the very weak B_{2u} (E‖a) mode 24 at 8.6 μm (10 K) wavelength; the B_{1u} (E‖c) mode 1 at 52.6 μm (10 K) wavelength[6]. For the B_{2u} mode 1 at 56 μm (300 K) wavelength it cannot be surely said how the feature will developed with increasing and also with decreasing temperature because the noise in that range is just too strong (see Fig 4.18). For the low temperatures, the increased noise is due to the smaller aperture that has been used for the measurements of the polarizations E‖a and E‖b in the cryostat. In Fig. 4.19, the low-temperature spectra for the E‖c polarization are shown for wavelengths up to 90 μm. The feature at about 70 μm wavelengths is relatively prominent. The corresponding oscillator frequency shifts from 140 cm^{-1}

[6]Again, the numbering of the modes corresponds to the parameters as given in Table A.5, starting with the mode at the longest wavelength (lowest wave number)

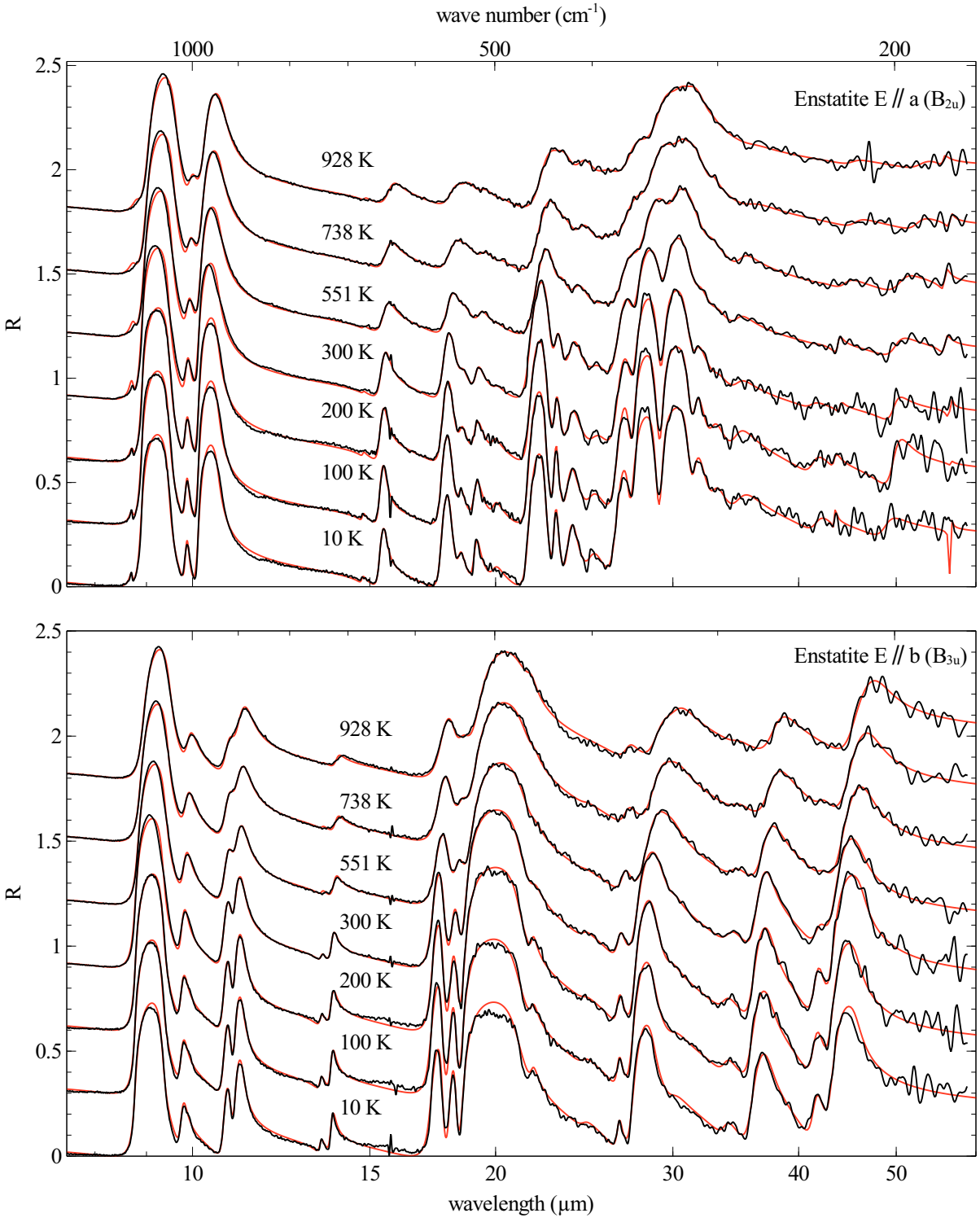

Figure 4.18.: Comparison of the measured reflectance (black) with the results of the fits (red) of the enstatite crystal for polarizations E||a (top) and E||b (botom). An offset of 0.3 has been added between each spectrum.

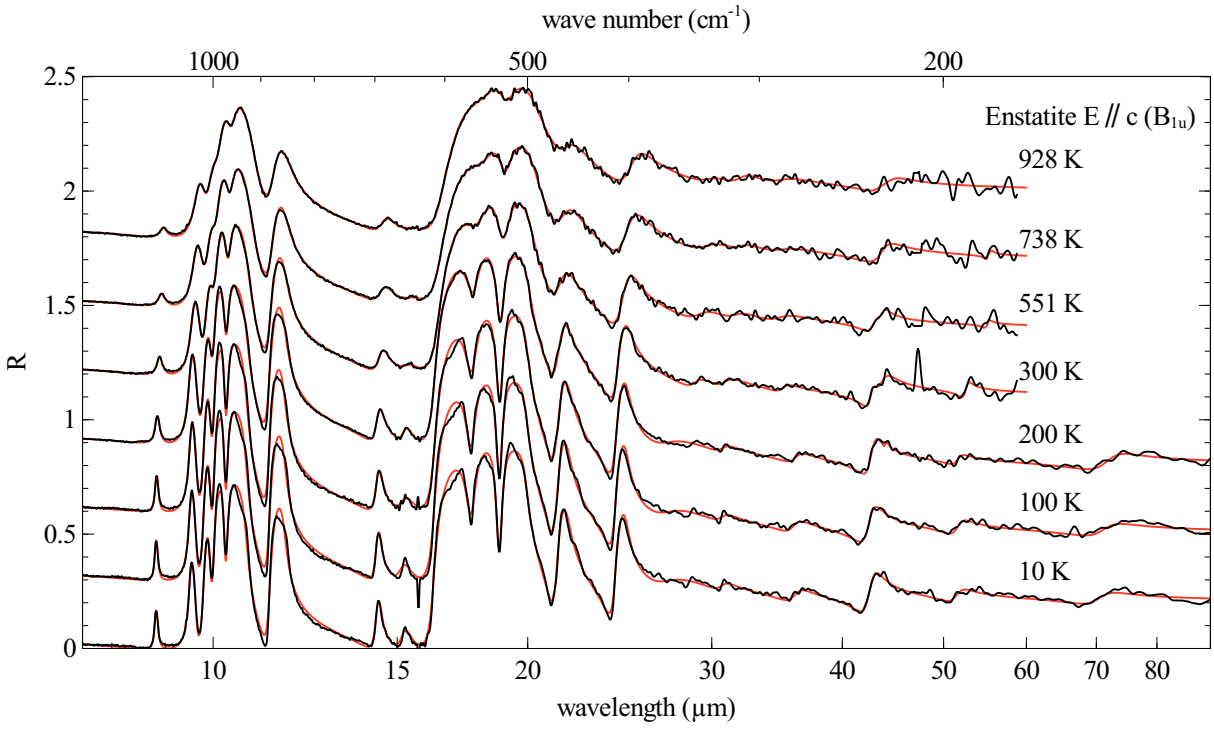

Figure 4.19.: Comparison of the measured reflectance (black) with the results of the fits (red) of the enstatite crystal for the polarization E‖c. An offset of 0.3 has been added between each spectrum.

(71.4 μm) at 10 K to 138 cm^{-1} (72.5 μm) at 200 K. As for all the other presented spectra, most of the features shift toward longer wavelengths with increasing temperature while the intensity of the features is decreasing and the width is increasing. Due to the huge amount of small features which are also relatively close to stronger ones, some features seem to merge into a single broad one at high temperatures (e.g. the B_{2u} features at around 30 μm in the E‖a polarization and the B_{1u} features at around 20 μm wavelength in the E‖c polarization).

4.5.3. Development of the fit parameters with temperature

In Fig. 4.20, the temperature development of the oscillator parameters for the B_{3u}-type modes (E‖b polarization), normalized to their respective value at 10 K, is shown. It is distinguished between weak (blue) and strong (red) modes. Therefore, four weak modes ($j = 4, 13, 16, 17$ at 34.4, 13.8, 10.9, 9.8 μm wavelength, respectively) and four strong modes ($j = 1, 3, 10, 18$ at 46, 37.5, 21, 18.7 μm wavelength, respectively) are exemplarily chosen to represent the general development of all modes in the enstatite sample. As in the case of spinel, the wavelengths-shift is increasing with increasing temperature. While for low-temperatures the shift is quite low (almost zero), for temperatures higher than 300 K, it follows an almost linear dependence with the temperature (as expected from the theoretical considerations in chapter 2). The strong modes show also a stronger temperature dependence of their wavelengths-shift

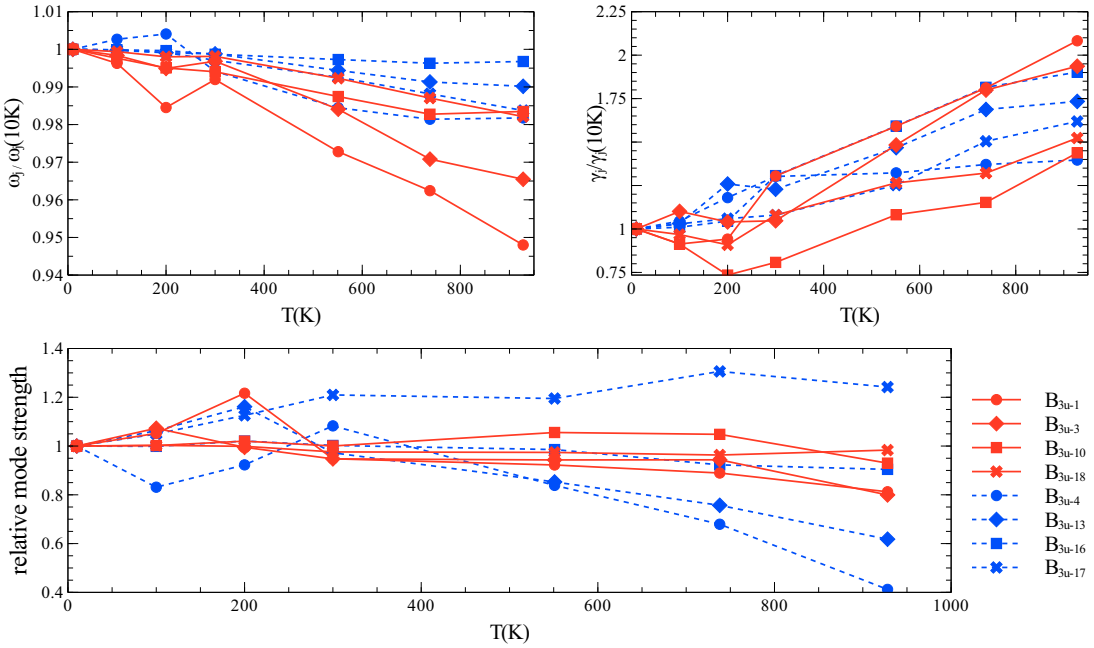

Figure 4.20.: Development of the oscillator parameters for four strong (red) and four weak (blue) modes in E||b polarization (B_{3u}-type modes) relative to their respective value at 10 K. The presentation is similar to the one shown for olivine. The numbering of the modes is regarding to Table A.5

(left diagram in the upper panel of Fig. 4.20) compared to the weak modes. The decrease of the shift at 928 K ranges in case of the strong modes between 0.98 and 0.95 while for the weak modes, it ranges from roughly 1 to 0.98. Contrary to spinel, the temperature development of the damping (right diagram of Fig. 4.20) shows no significant differences between the development of the weak and the strong modes. Both increase almost linearly with the temperature whereas for temperatures up to 200 K, the damping of the strong modes slightly decreases first with increasing temperature. Beyond 200 K, the damping is increasing again and follows an almost linear temperature dependence (this behavior is not shown by the weak modes). From 200 to 300 K for the mode $j = 1$, a sudden increase in the frequency and the damping and a sudden decrease in the strength can be observed, contrary to the respective developments at lower and higher temperatures. A similar 'jump' in the development of the damping is obtained for the mode $j = 10$. The behavior of these modes is likely due to the different setups of both high- and low-temperature measurements. The development of the mode strength, however, is similar to the case of spinel where the strong modes show only a minor temperature dependence in their strength. The weak modes, on the other side, show a much stronger dependence in the temperature but no general trend can be seen. The increased temperature dependence for the strength of the weak modes is likely due to the fact that the features become more and more hidden by stronger features with increasing temperature and thus it becomes more and more difficult to fit the weak modes correctly.

Compared to the data of Demichelis et al. (2012) of a pure enstatite, except some modes, the positions of all TO vibrations are shifted toward longer wavelengths which is likely due to the content of Iron in the crystal from Burma. Fe cations are heavier than Mg cations and therefore vibrations should have lower frequencies. In principle, the oscillator strength of the modes found in this study are similar to those found by Demichelis et al. (2012) but tend to become weaker toward longer wavelengths (up to 20 times weaker for some modes at wavelengths longer than 40 μm) which might be also due to the Fe content or even to the measurement setup which is by no means comparable to that of Demichelis et al. (2012) who used synchrotron radiation for their measurements.

4.6. Concluding remarks

In this chapter, we presented the results of the temperature dependent IR measurements on corundum, spinel, quartz, olivine, and enstatite. Fits with the aid of Eqs. (2.50) and (2.38) were applied for all spectra. As it was shown for all samples, the frequencies of almost all oscillators shift toward longer wavelengths with increasing temperature while the damping is increasing. It is remarkable that the dependence of the mode strength on the temperature is in the most cases not very significant. An exception for this purpose is quartz which experiences a phase transition at 846 K. It is further noteworthy that in the spectra of the SiO_2-containing minerals quartz, olivine, and enstatite the shift of the features is stronger for those at longer wavelengths. As for instance the feature at 9.2 μm at 10 K in the E$\|$a polarization of enstatite shifts only to 9.3 μm at 928 K while the strong but distinct feature at 22.1 μm shifts to 23 μm and the feature at 28.2 μm even to 30 μm. This behavior can already be seen in the reflectance spectra of all materials and is quantitatively summarized In the respective diagram of the relative change of the mode frequency in the Figs. 4.11, 4.16, and 4.20. A reason for this effect may be that the contributions of both thermal expansion and phonon-interaction, to the frequency-shift abrogate each other for modes at shorter wavelengths more than for those at longer wavelengths in these materials.

5. Temperature dependent transmission spectra of olivine

5.1. Multiphonon absorption in the NIR

5.1.1. ϵ_∞ at high temperatures

In order to account for multiphonon contributions on the IR spectra of olivine and enstatite, we also allowed ϵ_∞ to vary with the temperature in the fits with the Lorentz model. A temperature dependent ϵ_∞ in the oscillator parameters of the IR vibrations can be also seen as a first hint for the existence of temperature dependent multiphonon excitations in the NIR. In the case of olivine, the E‖a polarization shows a general decrease of ϵ_∞ with increasing temperature. The steepest decrease (2.43→2.39; see also Table A.4) appears between 300 and 551 K but the further decrease in ϵ_∞ at higher temperatures is negligible. It seems that also for the E‖a (C1) and E‖c (D1) polarization the fitted values of ϵ_∞ at 300 K are slightly too large compared to the values at higher temperatures. The reason is unclear but maybe due to the non-regular shape of the natural crystal, a small displacement caused by thermal expansion either by the cell or by the crystal could have been appeared that finally led to this 'jump' in ϵ_∞. The most distinct increase is obtained for E‖b (2.67 (300 K) →2.78 (928 K)). Since we expect mainly multiphonon contributions as being responsible for the development of ϵ_∞, a general increase should have been obtained but an unambiguous temperature dependence for ϵ_∞ in all polarizations could not be verified.

5.1.2. Multiphonon absorption at low temperatures

With the FTIR spectrometer and the helium-cooled cryostat in transmission mode, spectra of olivine have been taken in a wavelengths range of 3–7.5 μm. In this range, one-phonon processes are no more active and multiphonon processes can be directly observed. As already mentioned, for crystals with a distinct ionic character such as olivine, the absorption index compared to the IR vibrations and the electronic excitations in the UV is very low and therefore reflection spectra are not significant to investigate the behavior of the (weak)

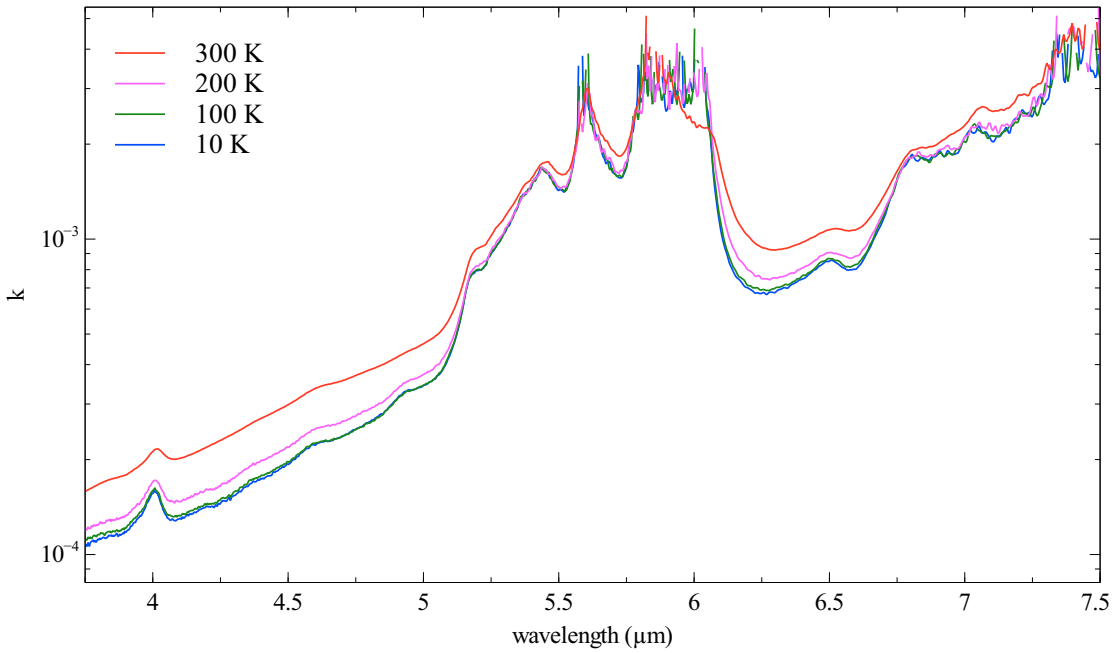

Figure 5.1.: Spectra of k for the olivine sample C1 in a wavelengths range from 3.75–7.5 μm at different temperatures. The dominant absorption feature in this range is the two-phonon band between 5 and 6 μm.

multiphonon contributions. The spectra have been taken for a polarization E‖a on the sample C1[1]. According to Eq. (3.3), the loss of transmitted intensity due to reflection has been determined to $R_{loss} = 0.048$ with $n_{NIR} = \sqrt{\epsilon_\infty} \approx 1.56$ resulting from the fit of the respective 300 K IR spectrum (see also Table A.4).

In Fig.5.1, the results of the calculated k values at four different temperatures are presented. There is a general decrease of the absorption toward shorter wavelengths owed by the short-wavelengths edge of the IR absorption features. However, several distinct absorption features can be seen. The most prominent feature is a relatively broad and strong absorption in the wavelengths range from 5.1–6.1 μm. Due to the strength of the absorption, the transmission in that range became almost zero which means that the detector of the FTIR spectrometer was not able to detect signals from the sample in that wavelengths range any more (saturated absorption spectrum). Therefore, the top of this feature is characterized by a strong noise at a mean value of k of roughly 3×10^{-3}. This strong absorption feature is mainly an overtone (two-phonon excitation) of the strong 10-12 μm mode of the sample C1 in E‖a polarization that consists actually of two separate excitations at 10.4 and 11.5 μm wavelengths (960 and 873 cm^{-1}; see Table A.4 and Fig. 4.13). They are likely responsible for the sub-features at 5.6 and 5.9 μm wavelengths[2]. The origin of the small sub-features at 5 and 5.2 μm remains unclear. Around 7 μm, a broad absorption feature can be seen which can have its origin

[1]The results from the measurements are exemplary also for the other polarizations.
[2]Because of the anharmonicity, the two-phonon excitations are not exactly at the half wavelength of the one-phonon excitations but more shifted toward longer wavelengths.

in carbonates on the surface of the sample and possibly the three-phonon excitations of the 20 and 21.1 μm one-phonon modes. The small but relatively distinct feature at 4 μm is likely due to a three-phonon excitation of the 11.5 μm one-phonon mode. Actually, this feature is also visible in the spectra of a very recent paper presented by Pittman et al. (2013) who investigated the absorption of forsterite and olivine (with an Fe content of 10%) single crystals in the UV–NIR spectral range. They show also the overtone at 5–6 μm wavelengths but with a spectral resolution that allows not to observe the sub-features which occurs in our spectra. Shankland and Nitsan (1979) presented high-temperature spectra in the UV–NIR range but also in their spectra, the resolution seems too low to investigate potential sub-features.

The spectra of the multiphonon excitations show no significant change with decreasing temperature which may be an indicator for a relatively strong anharmonicity of the respective modes and a consequently strong phonon-phonon interaction even at low temperatures. The background absorption, on the other side, shows a relatively strong decrease with decreasing temperature, probably due to the increased sharpening of the one-phonon excitations with decreasing temperature. Since there is no evidence for a significant temperature dependence of the multiphonon modes at high temperatures neither from the high temperature investigations in the NIR done by Shankland and Nitsan (1979) nor from ϵ_∞, we disclaimed on direct high-temperature measurements of the multiphonon excitations in the HTHP cell.

5.2. Crystal field bands in the NIR-VIS

In order to investigate the influence of the temperature on crystal field (CF) bands, NIR spectra of the olivine sample D1 in the range 0.7–2 μm have been taken at high and low temperatures. From the transmission spectra, k has been calculated for each temperature and the results are shown in Fig. 5.2. Since no polarizer were available, only non-polarized measurements could be taken to show the principle development of the CF bands with the temperature. Spectra of the sample were taken at 10, 100, 200, 300, 573, and 773 K. Unfortunately, because of the thickness of the sample D1 (1115 μm), the maximum in absorption became saturated at temperatures higher than 773 K, leading to a strongly decreased signal to noise ratio. Therefore, spectra are taken only for temperatures below or equal to 773 K. The cooling and the heating were provided by the Displex refrigerator and the HTHP cell, respectively. In the spectral ranges 0.81–0.87, 0.97–1, and 1.4–1.6 μm wavelength, it has become necessary to interpolate the low-temperature spectra due to a sudden decreases of the transmission signal. For the 0.81–0.87 μm wavelengths range, the decrease is due to the change of the detectors in the Lambda 19. For the other two ranges, the sudden decrease is likely due to the change of the optical filters inside the spectrometer which seemed to have a bigger influence on the resulting spectrum for the low-temperature setup than for the

high-temperature setup. In the high-temperature setup (the 300 K spectrum has been taken also in this setup), only the change of the detectors had such a big influence on the spectra that an interpolation became necessary.

The CF bands of olivine are due to the d orbital splitting of the Fe^{2+} cations in the M1 and M2 positions of the crystal lattice and lie in the spectral wavelength range of 0.7–1.5 μm (Burns, 1993; Shankland and Nitsan, 1979; Zeidler et al., 2011). In Fig. 5.2, they can be seen as the broad absorption feature in that range. Due to the small distortion of both positions, M1 and M2, from a perfect octahedral symmetry, the t_{2g} and e_g states are further split. In case of the M1 site, the t_{2g} state is split into a twofold degenerated state (e_g) of slightly lower and a single state (b_{2g}) of slightly higher energy. The e_g state splits into two single states a_g and b_g. In case of the M2 site, the t_{2g} state splits into three single states (a_1, a_2, b_2) and the e_g state again into two (a_1, b_1). Owing to these further splittings, additional CF excitations in both sites (M1 and M2) are accessible which lead to the very prominent feature in the NIR. The maximum of this feature is located at roughly 1.06 μm wavelength with a value of k of about 2.1×10^{-4} (at 300 K). Two broad shoulders on both sides of the maximum are observable: one at 1.25 and another one at roughly 0.87 μm wavelength which is also consistent with earlier measurements on olivine (Zeidler et al., 2011; Ullrich et al., 2002; Burns, 1993). The shoulders are due to the transitions $e_g \rightarrow b_g$ and $e_g \rightarrow a_g$ in the M1 sites while the maximum is owed by the transition $a_1 \rightarrow b_1$ and $a_1 \rightarrow a_1$ (Ullrich et al., 2002). The M1 transitions are Laporte forbidden while the M2 transitions are allowed due to the absence of an inversion center in this site (Ullrich et al., 2002) (see also 2.3.5).

As can be seen from Fig. 5.2, the prominent feature becomes rapidly broader and the intensity increases strongly for temperatures higher than 300 K. Also, the whole feature shifts toward longer wavelengths with increasing temperature. For lower temperatures than 300 K, still the feature becomes narrower and the intensity decreases with decreasing temperature but the overall changes of width, intensity and positioning of the band are less extensive. At 573 K, a small but distinct feature at around 0.99 μm becomes prominent that could, however, not be seen in the spectra at lower temperatures. This feature becomes also broader and more intense with increasing temperature as the spectrum at 773 K shows. Since the taken spectra are an overlap of the two polarizations E$\|$c and E$\|$b of the D1 sample, it is reasonable to assume that this feature is due to an excitation in one of these polarizations. However, the CF splitting that is shown e.g. in Burns (1993) in both octahedra predicts no excitation in that wavelengths range. Therefore, the origin of this feature remains unresolved but in the further general considerations on the temperature development of the CF bands, it plays no important role.

To give an estimation of the quantitative temperature dependence of the transitions in the M1 and the M2 sites, a fit with three Gaussians (four Gaussians in case of the high-temperature spectra with the feature at 0.99 μm) with the calculated (see Eq. (2.65)) spectra of α_{Bulk} of

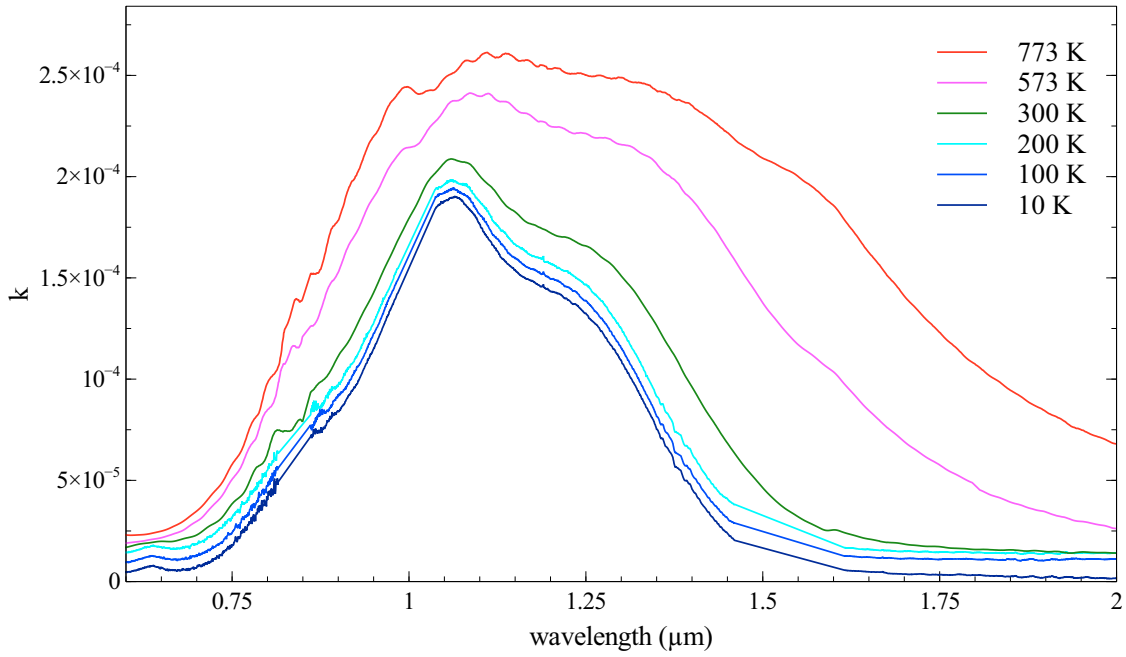

Figure 5.2.: Unpolarized spectra of k of the olivine sample D1 in the wavelengths range 0.6–2 μm at different temperatures. The broad feature between 0.7 and 1.5 μm is a crystal field band due to Fe^{2+} in the lattice.

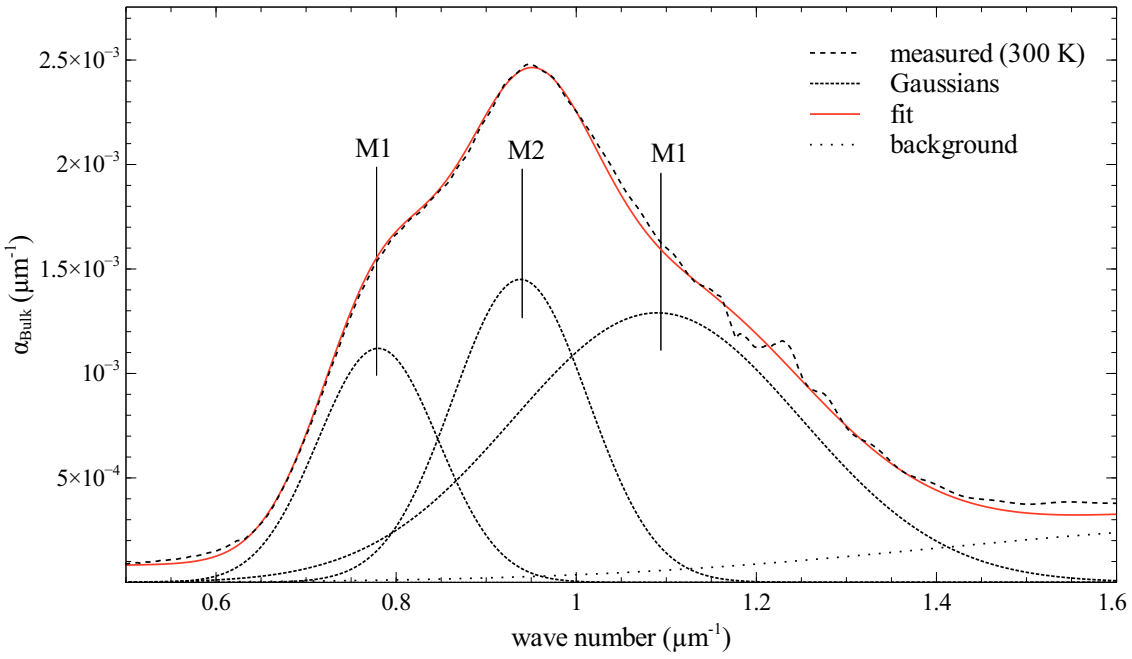

Figure 5.3.: Example of the curve fitting with three Gaussians representing transitions in the M1 and M2 sites of olivine. The fit were done with the linear absorption coefficient α_{Bulk} of the olivine sample over the wave number in μm^{-1}.

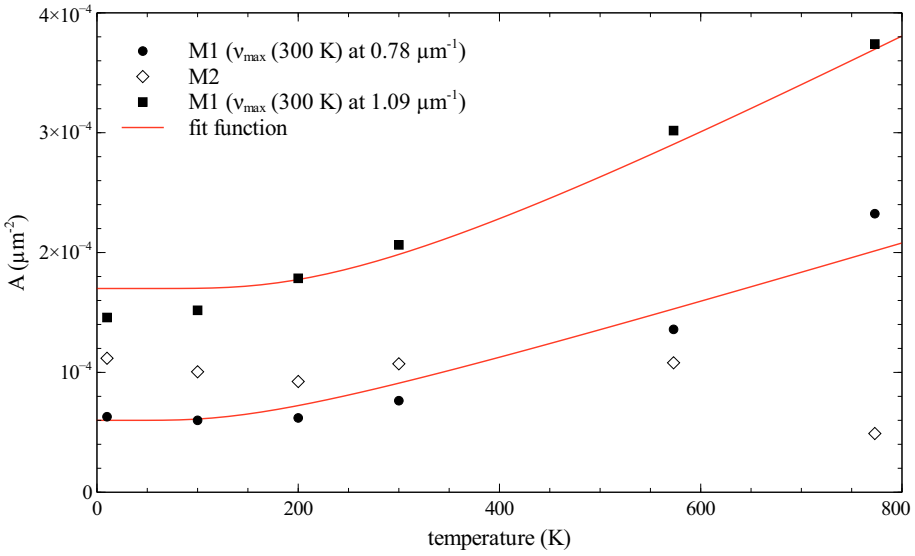

Figure 5.4.: Development of the band strength of the Gaussians with the temperature. In red, the fit functions, according to Eq. (2.58) are drawn.

olivine in dependence on the wave number ν was done, according to Ullrich et al. (2002). As Gaussian, the function

$$\alpha_{\mathrm{Bulk}} = \sum_{i=1}^{3} \alpha_{i\,\mathrm{max}} e^{-\frac{\nu_{i\,\mathrm{max}}^2}{2c_i^2}} \tag{5.1}$$

was taken, with $\nu_{i\,\mathrm{max}}$ as the wave number at the maximum $\alpha_{i\,\mathrm{max}}$ and c_i as parameter defining the width of the ith Gaussian. Although the spectra are non-polarized, it is reasonable to take only three Gaussians since the respective contribution to the feature in a certain polarization is not so different in position, strength and shape from that of another polarization (Ullrich et al., 2002).

The result of the fit for the 300 K-spectrum is shown in Fig. 5.3. Toward higher wave numbers (shorter wavelengths), the absorption becomes increased due to possible charge transfer processes from the Fe^{2+} to the ligands or even to Fe^{3+} that is likely produced by oxidizing in the heated HTHP cell and that leads to a brownish coloring of the crystal. However, a comparison of the polarized NIR spectra of the D1 crystal in the Lambda 19 with spectra of the yet unheated sample, showed no significant difference of the CF feature. Therefore, the influence of the Fe^{3+} on the spectra is assumed to be negligible. Anyway, to account for the increased absorption toward higher wave numbers, a weak, monotonously increasing function has been added (indicated by the dotted line in the figure). Temperature dependent spectra of the CF bands of olivine have been already taken by Ullrich et al. (2002) and Shankland and Nitsan (1979) but only at high temperatures. In this work, we will show for the first time the results of both high temperature and low temperature transmission measurements on olivine in the NIR. Anyway, at least for the high-temperature measurements, we could

Table 5.1.: Table for the fit parameters according to Eq. (5.1). The values for a are given in $10^{-3}\mu\mathrm{m}^{-1}$, for c in $10^{-2}\mu\mathrm{m}^{-1}$, and for $\nu_{\max}$ in $\mu\mathrm{m}^{-1}$.

	M1			M2			M1			0.99μm-feature		
T(K)	$\alpha_{\max}$	c	$\nu_{\max}$	$\alpha_{\max}$	c	$\nu_{\max}$	$\alpha_{\max}$	c	$\nu_{\max}$	$\alpha_{\max}$	c	$\nu_{\max}$
10	1.05	6	0.798	1.62	6.9	0.943	1.08	13.5	1.11		-	
100	1	6	0.8	1.5	6.7	0.943	1.1	13.8	1.11		-	
200	1	6.2	0.8	1.4	6.6	0.943	1.19	15	1.08		-	
300	1.14	6.7	0.78	1.41	7.6	0.94	1.29	16	1.09		-	
573	1.51	9	0.748	1.35	8	0.922	1.84	16.4	1.09	0.25	4.4	1.04
773	1.83	12.7	0.744	0.7	7	0.922	2.2	17	1.08	0.39	5	1.03

lean on the results of Ullrich et al. (2002) and Shankland and Nitsan (1979) in the analysis and the discussion of our results. We found that the M1 Gaussians (representative for the respective transitions in the M1 sites) increase in intensity and FWHM with increasing temperature while the M2 Gaussian decreases in intensity and FWHM (see Table 5.1). This result is in total agreement of the findings of Ullrich et al. (2002). The reason for this lies in the fact that the M1 transitions are Laporte forbidden and thus grow in their strength with increasing temperature while for the M2 transition an increase in the temperature leads rather to a decrease of the strength. The reason for this effect is that the M2 transition is not Laporte forbidden and thus the temperature dependence is decreased compared to Laporte forbidden transitions. Additionally, it seems that an increase of the temperature slightly weakens the M2 transition probably due to the increased mean distance between cation and ligand. The temperature development of the calculated band strength A of all three Gaussians is illustrated in In Fig. 5.4. Additionally, a fit function according to Eq. (2.58) was calculated with an effective phonon frequency of 0.0534 and $0.0330\,\mu\mathrm{m}^{-1}$ for the upper and the lower curve, respectively. This result is also in a good agreement to Ullrich et al. (2002) which give a value of roughly $0.06\,\mu\mathrm{m}^{-1}$ as effective phonon frequency for both M1 bands. As value for A_0, 1.7×10^{-4} and $0.6\times10^{-4}\,\mu\mathrm{m}^{-2}$, respectively, has been found which can be also seen as being in a good agreement to the findings of Ullrich et al. (2002) who give 2.2 and $2.4\times10^{-4}\,\mu\mathrm{m}^{-2}$.

6. Applications on the astronomical spectral analysis

A direct comparison of the absorption/emission properties of a material with astronomical spectra of dust around stars is only possible with a calculated absorption cross section σ_{abs}, corresponding to one of the presented models from section 2.4 (Mie, ellipsoidal particles of certain shapes,CDE ,...) or by direct measurements of the absorption of dust (Tamanai et al., 2006). As has been shown in chapter 4, with the results of the fits on the reflectance spectra, the optical constants for each spectrum can be calculated which again determine the dielectric function ϵ. With these, we are able to calculate σ_{abs} for particles within the Rayleigh regime (small-particle spectra).

In this chapter, the calculated absorption cross section of corundum, spinel, olivine and enstatite are used for comparisons with astronomical spectra of AGB stars and PPDs, respectively. In the former case, we will concentrate on a distinct feature around 13 μm wavelengths, periodically observed in spectra of oxygen rich AGB stars and attributed usually to either corundum or spinel. We outline a way of how our data can be used to decide which of these materials is responsible for the astronomical 13 μm feature. For the PPDs, we show that temperature dependent absorption cross sections can be used as thermometer for particular dust species by comparing individual features of small-particle spectra with emission spectra of cosmic dust.

6.1. The 13 μm feature of oxygen rich AGB stars

As has been mentioned already in chapter 1, until the present day there is a debate about the responsible mineral of an often quite prominent feature in the spectra of oxygen rich AGB stars. In all related spectra, this feature is located at around 13 μm wavelength whereas its intensity is varying depending on the state of evolution of the star on the AGB. Lebzelter et al. (2006) and Blommaert et al. (2007) have investigated different AGB stars in different evolutionary stages (Lebzelter et al. (2006) investigated AGB stars from the globular cluster 47 Tuc with masses up to 5 $M_{\odot}$ whereas Blommaert et al. (2007) observed a homogeneous sample of AGB stars in the galactic bulge with initial masses of 1.5 $M_{\odot}$). They found that

with the development on the AGB, and the connected increase of the luminosity of a star, the mass outflow increases and with increasing outflow the composition of the dust envelope around the star changes. Lebzelter et al. (2006) have shown that first with a luminosity of $\sim$2000 $L_\odot$ the dust production becomes such efficient that dust features can be seen in the spectra and with these first dust features also the 13 μm feature appears and dominates the spectra for such luminosities. Together with the 13 μm feature, usually a broad emission at $\sim$11.5 μm appears that has been assigned to amorphous Al_2O_3. With increasing luminosity and pulsation period, the 11.5 μm and a 9.7 μm feature become stronger while the 13 μm feature becomes weaker. The 9.7 μm feature is assigned with amorphous silicates which seem to dominate the spectrum in the very end of its development when the star becomes a Mira star (Lebzelter et al., 2006).

To compare the derived small-particle spectra with astronomical emission spectra, each $\sigma_{\rm abs}(\lambda,T)$ spectrum has been multiplied with the corresponding black-body function $B_\lambda(T)$ (with λ as wavelength of the emitted radiation). The result has been normalized to the maximum of the respective 13 μm feature[1]. We refer to the resulting curves, as 'normalized emissivities'. Additionally, selected spectra of AGB stars showing the 13 μm features have been reduced to the pure contribution of this feature to derive 'residual dust emissions'. Therefore, a polynomial has been used to represent all other dust components between 12–14 μm wavelengths than the carrier of the 13 μm feature[2], as sketched in Fig. 6.1. These spectra have also been divided by their respective maximum at the 13 μm feature. To broaden the empirical basis of our investigation, a mean emission spectrum out of 23 such residual dust emissions taken with the *Infrared Space Observatory* (ISO) (Zeidler et al., 2013) has been used for the comparisons with our normalized emissivities (see Fig. 6.1). All AGB-star spectra are kindly provided by Dr. Th. Posch.

As mentioned above, spinel and corundum are the most promising candidates which could explain the 13 μm feature. In the last years, several authors (Posch et al., 1999, 2003; Fabian et al., 2000) compared the emissivity spectra of small spherical particles of both minerals with emission spectra of AGB stars and concluded that spinel must be preferred as origin of the 13 μm feature because its spectra fit this feature much better than those of corundum which feature is much narrower and also shifted too much to shorter wavelengths. Additionally, small-particle spectra of spinel show an increased emissivity close to 32 μm which could explain a feature in that range seen in some spectra of AGB stars. However, spinel shows also a feature at $\sim$17 μm that yet could not be seen in the spectra of AGB stars. Around 21 μm also corundum particles show additional features which are quite weak but sharp. Another problematic point is the fact that all fits to the respective AGB-star spectra which have been made so far are done with 300 K data of n and k. Speck (1998) suggested

[1] Using the spectral emissivity is necessary for the comparisons because not only the spectral position of the features are investigated in this section but also their width which changes significantly by using the emissivity instead of just $\sigma_{\rm abs}$.

[2] in particular, this procedure is outlined in Posch et al. (1999) and Fabian et al. (2000)

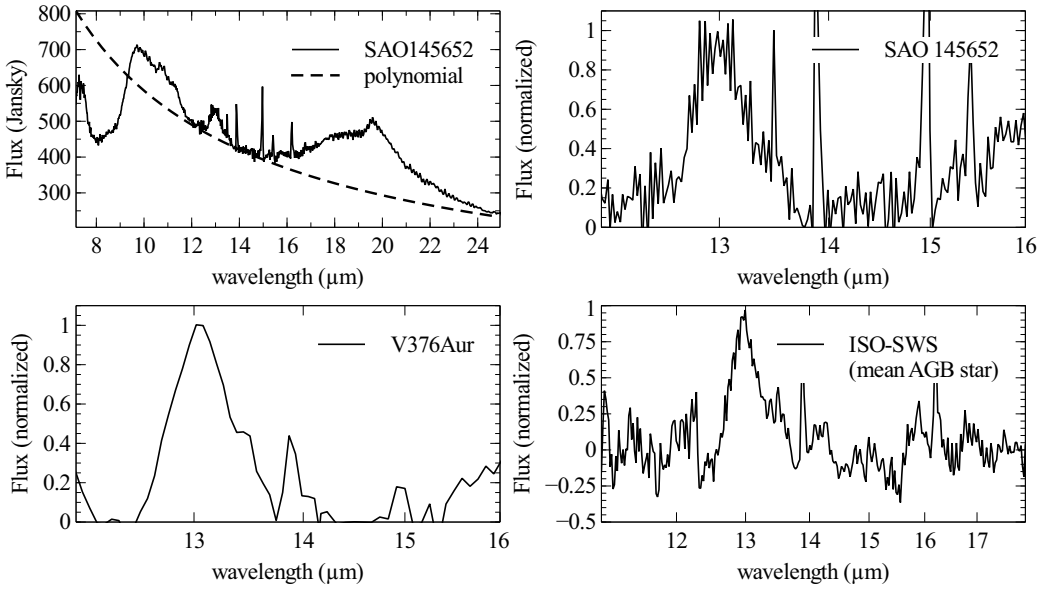

Figure 6.1.: Plots of emission spectra of different AGB stars. In the upper panel on the left, the spectral energy distributions (SED) of the star SAO145652 is shown together with the polynomial that is subtracted to get the residual dust emission of the 13μm feature (shown on the right side in the upper panel). In the lower panel on the left, a normalized residual dust emission of the 13μm feature of the S-star V376Aur is shown (taken with the Spitzer-Space-Observatory). On the right side, a normalized spectrum of the mean contribution of the 13μm feature to the SEDs of 23 AGB stars (taken with ISO-SWS) is plotted.

SiO_2 particles as being responsible for the 13 μm feature and indeed, SiO_2 particles show an emissivity feature at $\sim$12.5 μm (300 K). However, due to the very strong feature at $\sim$9.4 μm wavelength (1064 cm^{-1}, see Table A.3), the AGB spectra must show in either case together with the 13 μm feature the strong feature at $\sim$9.5 μm which is not observed[3].

6.1.1. The influence of the grain-shape on the 13 μm feature of corundum and spinel at RT

We calculated emissivity spectra of small spherical particles of corundum and spinel from σ_{abs} according to Eq. (2.65) at 300 K. The results are plotted in Fig. 6.2 compared to the 13 μm feature of the mean AGB-star emission from Fig. 6.1 in a wavelength range from 11.7 - 18 μm. In our case neither corundum nor spinel gives a good representation of the 13 μm feature. In the case of corundum, a double peak appears between 12.5 - 13.5 μm due to the two resonances perpendicular and parallel to the c axis. This double peak has no pendant in the astronomical spectra showing the 13 μm feature. Additionally, the main peak is shifted $\sim$0.3 μm toward shorter wavelengths compared with the astronomical feature. In contrast,

[3]For example, the AGB star V21 in 47 Tuc shows a strong 13 μm feature but no signs of an enhanced emission in the range 9-10 μm wavelength.

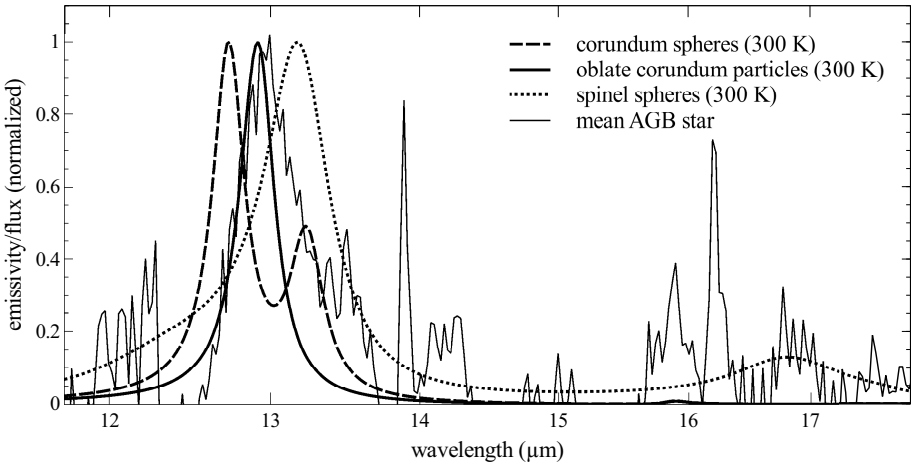

Figure 6.2.: Comparison of the mean AGB-star spectrum of the 13 μm feature with the normalized emissivities of small spherical particles of corundum and spinel and of small oblate particles of corundum with r_c/r_a=0.79 as investigated by Takigawa et al. (2012). All spectra are normalized to unity.

the peak of spinel is shifted toward longer wavelengths by $\sim$0.2 μm but seems to represent at least the shape of the astronomical 13 μm feature quite well. At 16.8 μm the above-mentioned weak feature of spinel can be seen.

It has been shown in chapter 2 that the shape of the particles can have an enormous influence on the resulting emissivity spectrum. Therefore, it is reasonable to answer the question about the shape of condensed particles in the outflow of oxygen rich AGB stars first before the problem of the temperature is treated. Since especially corundum is a non-isotropic material and natural single crystals are elongated along the crystallographic c axis, it is by no means reasonable to assume them to be spherical, also not in a freshly condensed state.

In their condensation experiments under conditions which are comparable to those in the atmospheres of oxygen rich AGB stars, Takigawa et al. (2012) found that the condensation rates of corundum are different for different crystallographic axes, which for a freshly condensed particle results in a flattening along the crystallographic c-axis. They derived an axis ratio of r_c/r_a=0.79 for condensed corundum and note that for small (r_a <0.1μm) oblate spheroidal grains with a slightly lower ratio of r_c/r_a=0.70, the position of the 13 μm feature could be well reproduced with room-temperature optical constants. For oblate corundum particles, σ_{abs} has been calculated with Eq. 2.70. The double peak in the emissivity spectrum disappears and a single peak is produced that in case of the experimentally derived axis ratio r_c/r_a=0.79 for r_a <0.1 μm would be still positioned at slightly shorter wavelengths than the 13 μm feature (see Fig. 6.2). When the size of the oblate spheroids is increased to values which become comparable to the wavelength, the peak will be further shifted toward longer wavelength and becomes broader. Aki Takigawa found that for oblate spheroids with r_a =0.5 μm the astronomical 13 μm feature is well reproduced with the experimentally found

axes ratio of 0.79 (Takigawa et al., 2012).

In the case of spinel, no experiments are known that give rise to the assumption that non-spherical grains should be formed. Therefore, the derivations of the emissivity have been solely made with spherical grains.

6.1.2. Temperature dependent spectral properties of small corundum and spinel grains

In Fig. 6.3, the temperature dependence of the emissivities of small spherical corundum and spinel grains compared with the 13 μm feature of the mean ISO spectrum is shown. With increasing temperature the peak position of the strongest resonance of spherical corundum grains shifts to longer wavelengths, until a position of almost exactly 13 μm is reached for temperatures close to 1000 K. However, also the bandwidth increases significantly with the temperature. The width of the 13 μm corundum feature becomes too large at T=928 K compared to the mean AGB-star spectrum. For spinel an increase of the temperature would lead to an increased mismatch with the mean AGB-star profile owed by the shift and the broadening of the 13 μm feature of spinel. For low temperatures (not shown in the figure), the peak is again shifting toward longer wavelengths so that spinels 300 K spectrum comes closest to the mean ISO profile (see also the temperature development of the oscillator parameters of spinel in section 4.2).

The position of the 13 μm feature of spinel, on the other side, is also shifting toward longer wavelengths with increasing temperature but departs from its astronomical counterpart. Also, the width of the feature becomes broader leading to an increased mismatch with the 13 μm feature of the mean AGB-star spectrum.

In Fig. 6.4, the emissivities of oblate spheroidal grains derived with the experimental axis ratio found by Takigawa et al. (2012) (r_c/r_a=0.79) are plotted together with the mean AGB-star spectrum and the spectrum of the star V376Aur. Keeping the grain size small, for T=551 K a very good representation of the observed 13 micron band profile with the mean AGB-star spectrum is achieved. With the data at 300 K, the calculated 13 μm feature of the oblate particles is at shorter wavelength and also narrower than that of the mean AGB-star spectrum. For higher temperatures, the corundum peak shifts further to longer wavelengths which leads to a discrepancy with the 13 micron band. However, the star V376Aur (on the right side of Fig. 6.4) shows a slightly broader 13 μm feature that is also a bit more shifted toward longer wavelength (for $\sim$0.1 μm) than in the mean spectrum which may be an indicator of higher (mean) dust temperatures. Actually, emissivities of oblate spheroidal corundum grains at 928 K give a good representation of the emission spectrum of this star.

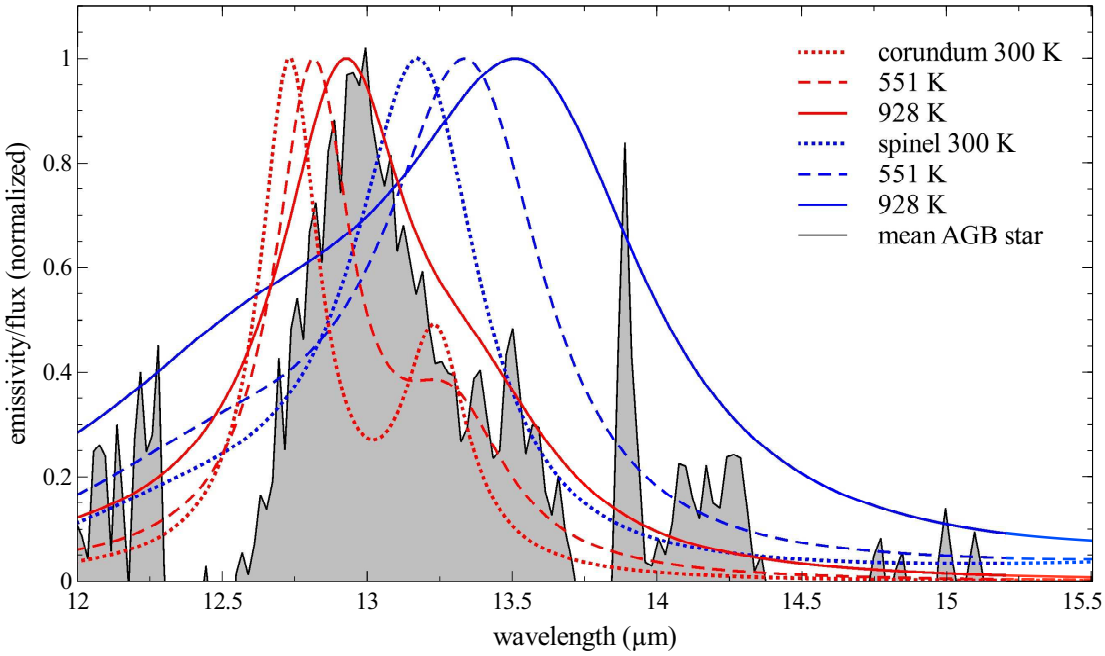

Figure 6.3.: Calculated normalized emissivities of small corundum and spinel spheres between 12 and 15.5 μm wavelength at different temperatures and normalized to unity. The emissivities are compared with the (normalized) Flux of the 13 μm feature of the mean AGB-star spectrum.

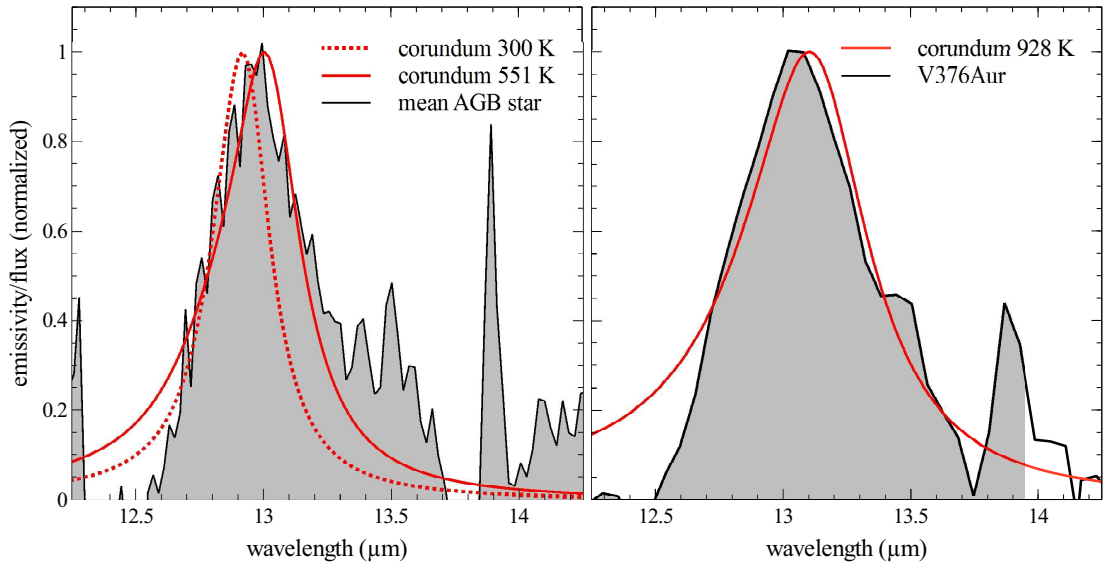

Figure 6.4.: Calculated normalized emissivities of small oblate corundum particles as prognosticated to form around AGB stars by Takigawa et al. (2012). The normalized Flux of the 13 μm feature of the mean AGB-star spectrum (left) and the one of the star V376Aur (right) that is broader than the feature in the averaged spectrum are shown.

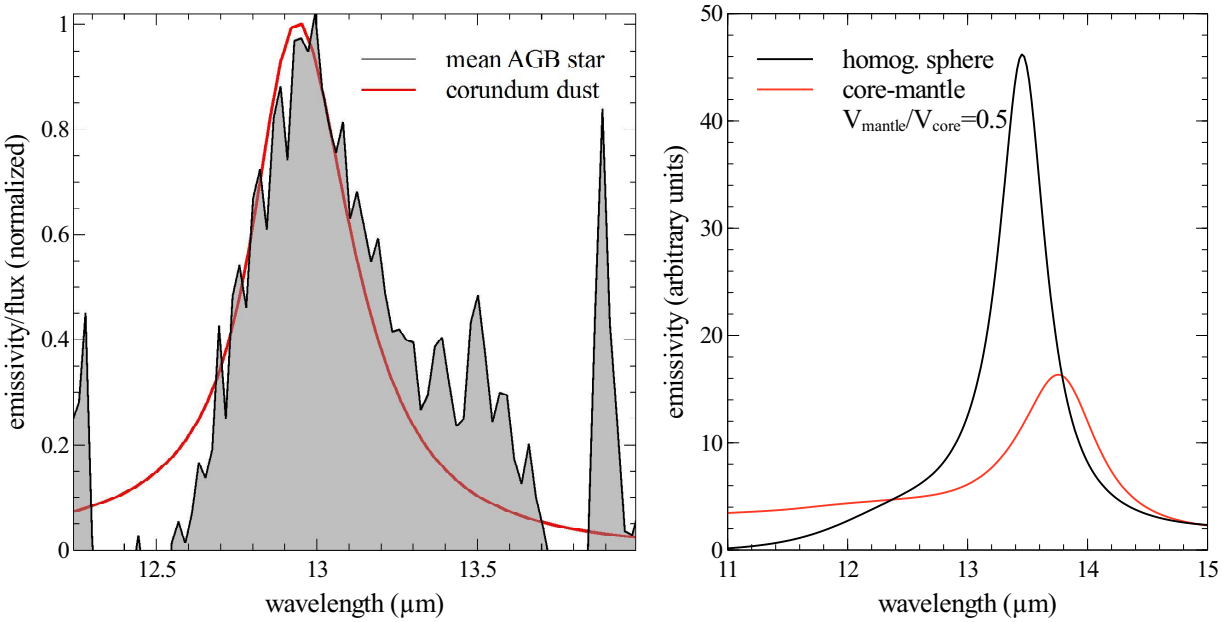

Figure 6.5.: Left: the estimated normalized emissivity of corundum dust based on the T^{-4} distribution in comparison with mean AGB-star spectrum of the 13 μm band. Right: diagram that shows the influence of a mantle of astrosil around a small spinel particle on the emissivity (calculated with the DDSCAT model).

Therefore, if corundum condenses as small oblate particles with an axis ratio of r_c/r_a=0.79 than it seems that hot corundum dust grains are more likely to be the origin of the 13 μm feature in the spectra of oxygen rich AGB stars with low to intermediate luminosities. In this context, it should be noted that only 1% of corundum in the circumstellar shell of an AGB star is sufficient to account for the strength of the 13 μm feature (DePew et al., 2006).

6.1.3. Temperature distribution

Concentrating on corundum as the most promising candidate that is responsible for the 13 μm feature in spectra of AGB stars, we can start to think about more realistic conditions of the dust in stellar outflows. Of course, it is not reasonable for the dust grains to assume that they have only a specific temperature, shape, and size. It is more likely to have a certain distribution of these parameters. Anyway, assuming that the corundum grains are all within the Rayleigh regime, we will concentrate on the idea of having only oblate particles with a defined axis ratio of r_c/r_a=0.79 to give at least a rough estimation for the effects of a temperature distribution of corundum particles on the emissivity spectra.

Gail, Nowotny and Posch (in preparation) calculated the development of the temperature and condensation rate of the corundum dust in an outflow of an AGB star (T_{eff}=2800 K; $L = 6740 L_\odot$) with increasing distance R to the star. The calculations were done under the assumption that the dust development is interaction-free and without condensation of

other materials on the corundum dust. They obtained the condensation rate of corundum grains to follow a saturation-function at which the condensation is initiated at $R \approx 3R_{\odot}$ and reaches saturation at $R = 10R_{\odot}$. The temperature of the corundum dust is decreasing with increasing distance to the star following in principle a polynomial of the order R^{-3}. We derived from these data a rough estimation of the principal distribution of the number of corundum particles in dependence of the temperature and obtained a polynomial of the order T^{-4}. With this result, ∼90% of the corundum particles around an AGB star would have a temperature of less than 200 K. For the 13 μm band of small, oblate corundum particles, this would imply a feature that is shifted too much toward shorter wavelengths and is also a too narrow to fit the observations (see Fig. 6.5). From these very rough estimations, it seems reasonable to assume a 'shielding' of corundum particles at temperatures below 300 K owing to condensation of silicates or amorphous Al_2O_3 on the corundum particles (core-mantle-particles). This assumption has been remarked already by Gail and Sedlmayr (1998) and Molster and Waters (2003). In calculations, done with the DDSCAT model by Draine and Flatau (1994), we found that the emissivity in the 13 μm band of small particles with a spinel core and a mantle of astrosil[4] decreases rapidly with increasing V_{mantle}/V_{core} ratio. For convenience, we have chosen spinel and not corundum for the calculations but the principal effects are the same. In Fig. 6.5, the results of the calculations are given. The V_{mantle}/V_{core} ratio is 0.5. The 13 μm feature is shifted 0.6 μm toward longer wavelengths and becomes broader.

If the low-temperature corundum particles become shielded by other materials, then in the temperature distribution hotter particles will be favored.

6.2. Silicates in protoplanetary disks - features as temperature indicator

By forming a PPD around a new-born star, the properties of the dust, that comes from the ISM, are changing. It is likely that the (amorphous) silicates from the ISM are confronted with annealing processes when heated close to the star but also gas-phase condensation can happen. Therefore, crystalline silicates can be created and indeed, it has been proved by IR spectroscopy of PPDs around Herbig Ae/Be stars that crystalline silicates in form of forsterite and enstatite can be found rather close to the star. But hints on their existence were also found in the outer (or at least cooler) parts of PPDs which points to a mixing of dust in a disk. Therefore, for both forsterite and enstatite dust grains, it is reasonable to assume a wide temperature distribution.

[4]that is an invented material which represents the optical properties of a mean dust particle in space. It consists manly of amorphous, Mg-rich silicates.

In order to get information on the temperature of the dust species, we compared the emissivity of olivine and enstatite dust with the emission spectra of several Herbig Ae/Be stars which were chosen because of the relatively high content of forsterite and enstatite, according to Juhasz et al. (2010). Since Herbig Ae/Be stars are very young (<10 Myrs), processes that lead to a decrease of the amount of dust around the star (planet formation, 'outblow' of dust grains,...), should not yet been finished and therefore the dust disk is well observable with IR spectroscopic instruments. The spectra which we have used are taken with the Spitzer-Space-Observatory and are already reduced to the pure emission from the respective PPD. A. Juhasz kindly provided the spectra which he had also used in Juhasz et al. (2010).

With the aid of the oscillator parameters that are derived by the fits of the olivine and enstatite spectra, the absorption cross section according to the CDE model (Eq. (2.74)) was calculated to simulate a certain distribution of different grain shapes (see section 2.4.3). The emission spectra of the PPDs are then directly compared with the respective absorption cross sections. For convenience, we did not calculate the emissivity for the comparisons. This is reasonable because we are only interested in the positions of the features which do not change significantly by using the spectral emissivity. For a direct comparison between the absorption cross sections at different temperatures, see Fig. 6.6. To get information about the temperature of olivine and enstatite dust from the positions of the features alone is of course somewhat too simple. Especially the Fe content in olivine and enstatite has also a significant influence on the positions of the features: they shift toward longer wavelengths as the Fe content increases. Also, features at longer wavelengths suffer more from the shift than features at shorter wavelengths as found by Fabian et al. (2000). Therefore, in principle also the width has to be considered that is not influenced by the Fe content for most of the features. However, this is difficult to measure in the given astronomical spectra but since our olivine sample is already Fe containing and even somewhat Fe rich compared to olivines in PPDs (Molster and Waters, 2003; Bradley, 2003), we can give an at least lower limit for the temperature estimation.

In Figs. 6.7, 6.8, and 6.9 the emission spectra of the PPDs of the Herbig Ae/Be stars HD37806, HD145263, and HD179218, respectively, are shown together with the calculated absorption cross sections of olivine and enstatite at those temperatures where the best fit with the positions of the olivine and enstatite features is reached. Each figure is divided into a diagram showing the spectral range 5–14 μm and a diagram showing the spectral range 15–35 μm. Following the outcomes of Juhasz et al. (2010), the different spectral ranges show different forsterite-enstatite ratios. While the short wavelengths range shows a decreased forsterite-enstatite ratio, the opposite is true for the long wavelengths range. Apparently, this is due to an overabundance of pyroxene-like silicates in the inner and hotter part of the PPD (Juhasz et al., 2010).

Actually, for the stars HD145263 and HD37806, in the long wavelengths range no feature has

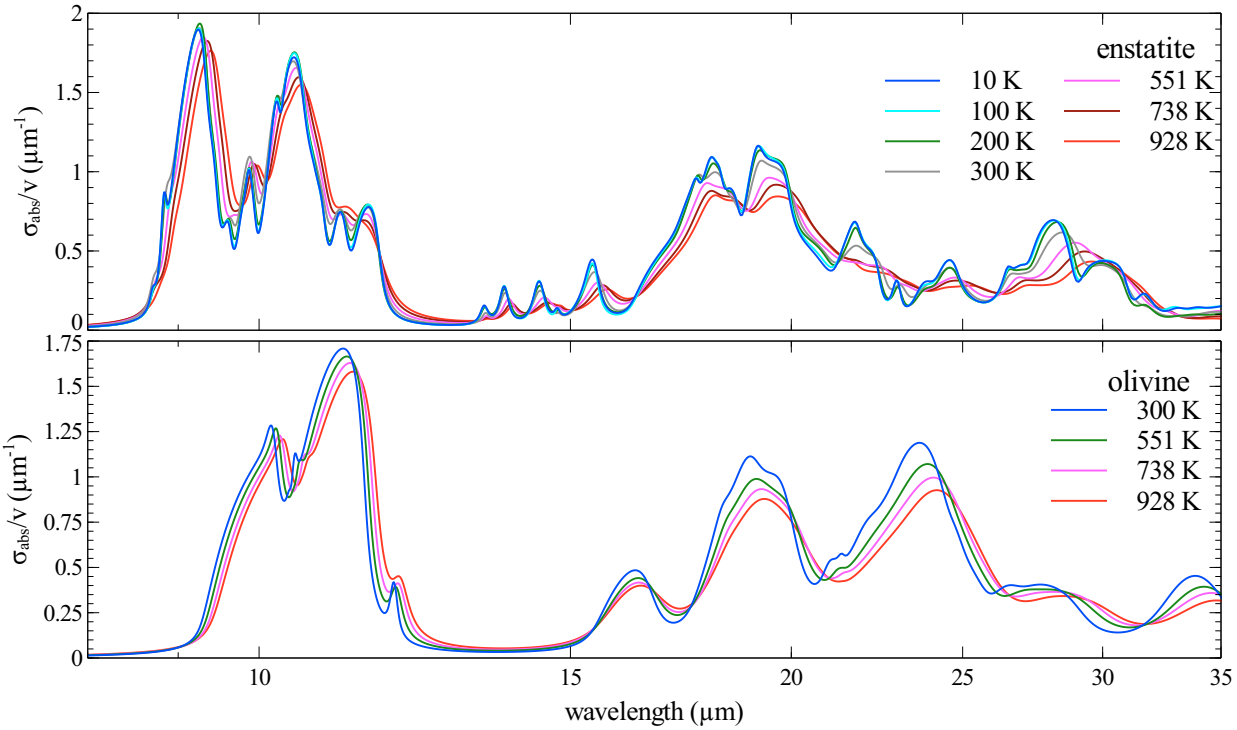

Figure 6.6.: Volume normalized absorption cross sections for enstatite (top) and olivine (bottom) at different temperatures, calculated with the CDE model.

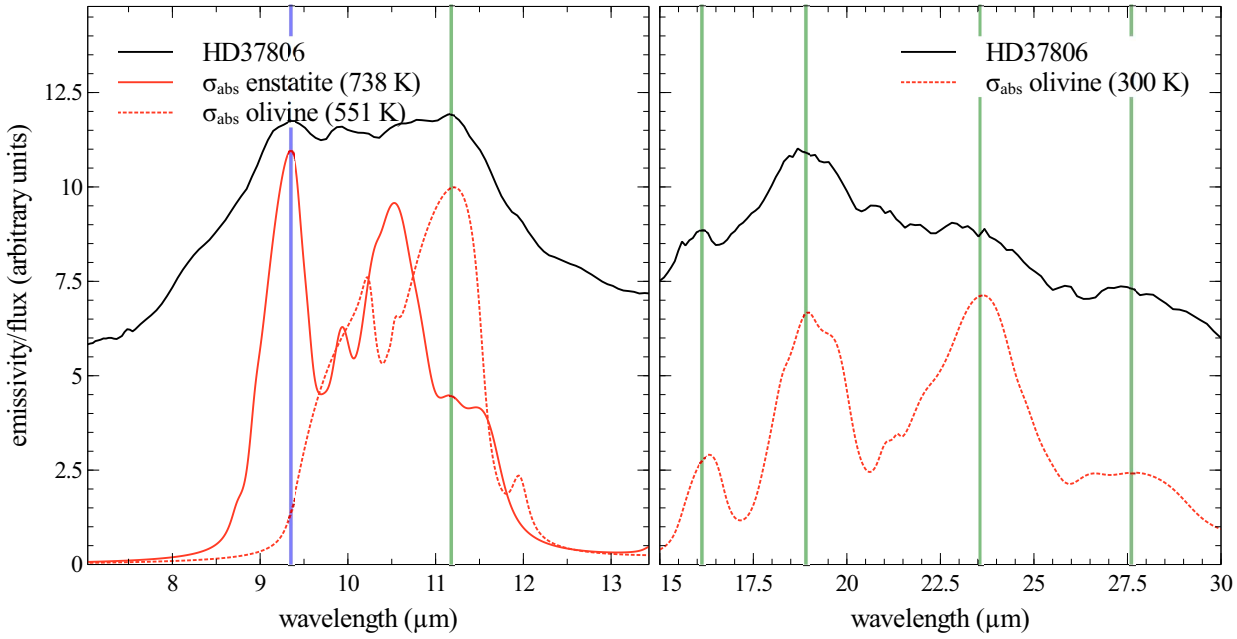

Figure 6.7.: Comparison between the absorption cross sections of enstatite and olivine dust, calculated with the CDE model, and the flux of the star HD37806. The vertical lines indicate features of olivine (green) and enstatite (blue) in the spectrum of the star.

been found that explicitly corresponds to small enstatite grains but in the short wavelengths range in all three spectra a prominent feature at 11.4 μm corresponds quite well with a strong absorption feature of enstatite grains at 738 and 928 K, respectively. Another prominent feature in this wavelengths range is found at 11.2 μm which can be represented by olivine dust at 551 and 738 K, respectively. In the long wavelengths range of HD37806 and HD179218, the spectral features at 16.1, 18.9, 23.5, and 27.6 μm wavelengths agree well with the absorption features of olivine dust at 300 K. For HD145263, these features are shifted 0.4–2 μm toward longer wavelengths which now corresponds with olivine dust at 738 K. The olivine dust in the short wavelengths range of HD145263 seems also to have a higher temperature than for the other two stars (738 K instead of 551 K). Peak related evidences for enstatite in the long wavelengths range have been found only for the star HD179218. Features at 15.4, 18.1, 21.7, and 28.1 μm wavelength are associated with enstatite dust at 200 K whereas the feature at 28.1 μm is in a competition to the contribution of 300 K olivine dust (at 27.7 μm wavelength). In the short wavelengths range, an additional feature at 10.6 μm has been attributed to enstatite dust at 928 K.

For the PPDs of all three stars, we found evidences for hot ($> 300\,K$) olivine and enstatite in the dust at short wavelengths, corresponding to the findings of Juhasz et al. (2010). For long wavelengths, contributions for cold dust has been found at least for two of the three stars. In HD145263, it seems that hot dust is dominating the whole spectral range. Anyway, it should be noted that the findings in this section are only related to grain shapes which correspond to the CDE. For other shapes, the conclusions might be different. Therefore, the comparisons with the astronomical spectra should rather be an idea of how our data can be used as a thermometer for dust species in PPDs.

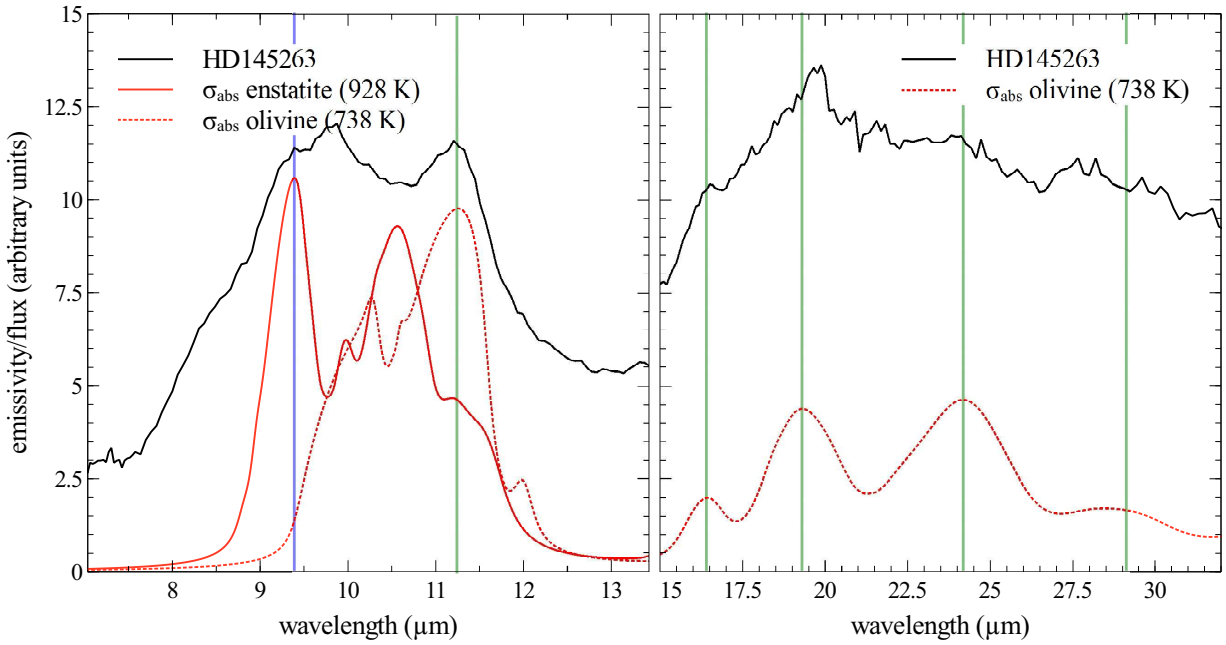

Figure 6.8.: Comparison between the absorption cross sections of enstatite and olivine dust, calculated with the CDE model, and the flux of the star HD145263. The vertical lines indicate features of olivine (green) and enstatite (blue) in the spectrum of the star.

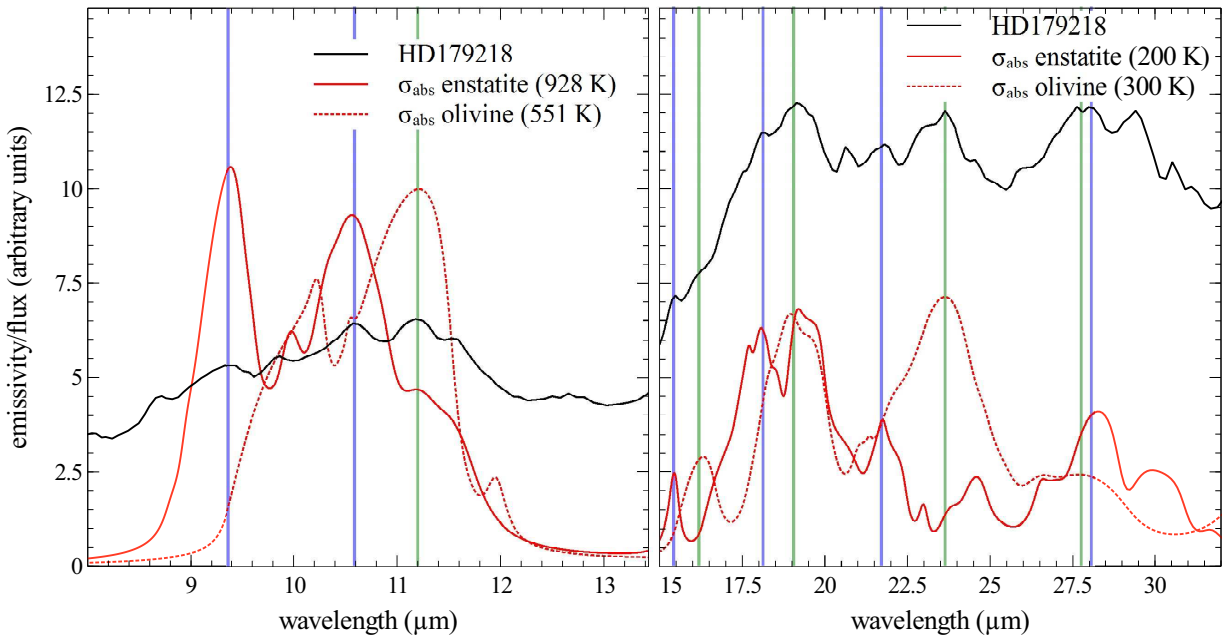

Figure 6.9.: Comparison between the absorption cross sections of enstatite and olivine dust, calculated with the CDE model, and the flux of the star HD179218. The vertical lines indicate features of olivine (green) and enstatite (blue) in the spectrum of the star.

7. Conclusions

The aim of this work was to investigate spectroscopically the temperature dependence of the optical properties of selected, astrophysical relevant minerals and to give ideas of how these data can be applied to analysis of astronomical spectra. Therefore, reflectance spectra of the polished, and along the crystal axes oriented, surfaces of corundum, spinel, quartz, olivine, and enstatite single crystals at different temperatures (T) were taken with polarized light in the wavelengths range of 7 to 60 μm (IR) with the aid of an FTIR spectrometer. Additionally, transmittance spectra of olivine single crystals were taken at different temperatures in the wavelengths range of 0.8 to 8 μm (NIR) with the aid of a Lambda 19 UV–NIR spectrometer. In order to heat and cool the samples, a high-temperature cell, a liquid-helium-flow cryostat (for the FTIR spectrometer), and a closed-cycle cooler (for the Lambda 19) were applied. For all samples, measurements were done at 300, 551, 773, and 928 K while for enstatite, spinel and olivine, also spectra at 10, 100, and 200 K were taken (olivine only in the NIR). All reflectance spectra were fitted with the aid of an oscillator models resulting in a set of oscillator parameters for each spectrum. With these data, the optical constants n and k and small-particle spectra (absorption cross section, emissivity) of the respective material and at each temperature were calculated. In the case of those crystals with a strong polar character (corundum, spinel, and quartz), we have used the FPSQ (Four-Parameter-Semi-Quantum) model (Gervais and Piriou, 1974) and in the case of olivine and enstatite, the Lorentz model for the fits. With the aid of the FPSQ model we were able to determine the frequency and the damping of the TO and LO modes while the Lorentz model gives the frequency and the damping of the TO mode only and the oscillator strength as a third parameter.

We found that features in the reflectance spectra usually shift to longer wavelengths with increasing temperature while they become broader and their maximum values decreases. The same holds true for the features of the calculated n and k and small-particle spectra, respectively. The temperature dependent change of the frequency and the damping is stronger for temperatures higher than 300 K and follows a linear, in a few cases also quadratic function. For lower temperatures the dependence of the parameters on the temperature is not that significant as the results of spinel and enstatite show. We also compared weak with strong modes and could find differences in the temperature dependence. For weak modes, the oscillator strength shows a much stronger temperature dependence than for strong modes (the oscillator strength was estimated as $\omega_{LO}^2 - \omega_{TO}^2$ for the FPSQ fitted spectra). An effect that

is also due to the difficulties in fitting very weak reflectance features as it has been shown for spinel. For the spectra of quartz, the shift of the frequency for both TO and LO modes, is strongly influenced by the phase transition from α- to β-quartz at 846 K and shows an exponential development. The oscillator strength is is not very influenced by the transition for temperatures below the transition point but shows a sudden 'jump' to higher and lower values right after 846 K. In the case of corundum, we gave an estimate of the contributions of the thermal expansion and the phonon-interaction to the change of the oscillator frequency with the temperature. In both the thermal expansion and the phonon-interaction, linear terms dominate the temperature dependence at $T > 300$ K which hints to a domination of cubic terms in the anharmonic contribution to the crystals Hamiltonian. Except for quartz, similar developments are shown also by all other high-temperature spectra. The most comprehensive data regarding to the investigated temperature (10–928 K) and wavelengths (7–90 μm) range have been obtained for the reflectance spectra of enstatite. They show very clearly the trend of an increased temperature dependence of the spectral position for modes at longer wavelengths, a behavior that has been found also for olivine and quartz.

From the transmission measurements in the NIR, k could be determined for olivine. With the data, we investigated the temperature development of multiphonon excitations at low (down to 10 K) and the crystal field bands at low and at high (up to 773 K) temperatures. The multiphonon excitations did not show a significant change with the temperature. However, the CF bands show a strong increase in their strength for temperatures higher than 300 K but only a minimal change for those lower than 300 K. The development of the strength of the band could be well fitted with a hyperbolic cotangent function of the reciprocal temperature as predicted by theory.

With the aid of the temperature dependent oscillator parameters of corundum and spinel, we could show that oblate corundum grains (as predicted by Takigawa et al. (2012)) with a temperature of 551 K rather than spinel is responsible for the well known 13 μm band profile in spectra of oxygen rich AGB stars. With our data, even at low temperatures the feature of spinel particles is too much shifted toward longer wavelengths to fit the 13 μm band. We further outlined how features of the temperature dependent small-particle spectra of olivine and enstatite, directly compared with astronomical emission spectra, can be used as a thermometer to determine the mean temperature of olivine and enstatite grains in dust disks around stars.

8. Zusammenfassung

Das Ziel dieser Arbeit war es die Temperaturabhängigkeit der optischen Eigenschaften von ausgewählten Mineralen mit astrophysikalischer Bedeutung spektrospisch zu untersuchen und Ideen aufzuzeigen wie die Ergebnisse dieser Untersuchungen auf astronomische Spektren angewendet werden können. Zu diesem Zweck wurden Reflexionsspektren von polierten Oberflächen von, bezüglich der Kristallachsenrichtung, orientierten Korund-, Spinell-, Quarz-, Olivin- und Enstatit-Einkristallen in einem Wellenlängenbereich von 7 bis 60 μm (IR) und bei unterschiedlichen Temperaturen (T) mittels eines FTIR Spektrometers und polarisiertem Licht aufgenommen. Zusätzlich wurden auch Transmissionsspektren an Olivin-Einkristallen in einem Wellenlängenbereich von 0.8 bis 8 μm (NIR) bei unterschiedlichen Temperaturen mittels eines Lambda 19 UV–NIR Spektrometers aufgenommen. Das Heizen und Abkühlen der Proben wurde über eine Hoch-Temperatur-Zelle bzw. über einen Flüssig-Helium Kryostaten (für das FTIR) und einem Kreislauf-Kühler (für das Lambda 19) realisiert. Hoch-Temperatur Spektren bei 300, 551, 773, und 928 K wurden für alle Proben im IR gemessen. Für Enstatit, Spinel und Olivin wurden zusätzlich auch Spektren bei 10, 100, und 200 K aufgenommen (Olivin dabei nur im NIR). Alle Reflexionsspektren wurden mit einem Oszillatormodell angefitted um mittels der daraus erhaltenen Oszillatorparameter die optischen Konstanten n und k bzw. Klein-Teilchenspektren (Absorptionsquerschnitt, Emissivität) zu bestimmen. Im Falle der stark polaren Kristalle des Korunds, Spinells und des Quarz benutzten wir das FPSQ (Four-Parameter-Semi-Quantum) Modell von Gervais and Piriou (1974) und im Falle des Olivins und des Enstatits das Lorentz Modell für die Fits. Mit Hilfe des FPSQ Modells war es uns möglich die Frequenz und die Dämpfung der TO und LO Moden zu bestimmen, während das Lorentz Modell die Frequenz und die Dämpfung der TO Moden und als dritten Parameter die Oszillatorstärke hat.

Wir konnten feststellen, dass die Banden in den Reflexionsspektren im Allgemeinen sich zu längeren Wellenlängen hin verschieben wobei sie breiter werden und ihr Maximalwert fällt. Dieselben Entwicklungen konnten wir auch in den Banden der n und k bzw. der Klein-Teilchenspektren beobachten. Die temperaturabhängige Änderung der Frequenz und der Dämpfung ist dabei stärker für Temperaturen höher als 300 K und folgt einer linearen, in manchen Fällen auch quadratischen Funktion. Für tiefere Temperaturen ist die Abhängigkeit der Parameter von der Temperatur weniger deutlich wie die Ergebnisse vom Spinell und vom Enstatit zeigen. Wir verglichen auch starke mit schwachen Moden und stellten Unterschiede

in der Temperaturabhängigkeit fest. Bei schwachen Moden zeigt sich eine im Vergleich zu den starken Moden deutlichere Abhängigkeit der Oszillatorstärke von der Temperatur (die Oszillatorstärke wurde für FPSQ gefittete Spektren mittels $\omega_{LO}^2 - \omega_{TO}^2$ abgeschätzt). Dieser Effekt ist auch auf das Problem zurückzuführen schwache Banden in den Spektren korrekt anzufitten, wie für den Spinell gezeigt wurde. In den Spektren von Quarz ist der Frequenzversatz der TO und LO Moden stark vom Phasenübergang bei 846 K geprägt und zeigt einen exponentiellen Verlauf. Die Oszillatorstärke der einzelnen Moden zeigt für Temperaturen unter 846 K nur wenige Änderungen mit der Temperatur, springt aber für $T > 846$ K auf sehr viel höhere bzw. niedrigere Werte. Für Korund konnte eine Abschätzung über die Beiträge der thermischen Ausdehnung und der Phononenwechselwirkung zum Frequenzversatz bei hohen Temperaturen gegeben werden. In beiden dominieren lineare Terme die Temperaturabhängigkeit für $T > 300$ K was auf eine Dominanz kubischer, anharmonischer Beiträge zur Hamilton-Funktion des Kristalls hindeutet. Ähnliche Entwicklungen zeigen, mit Ausnahme derer des Quarz, auch alle anderen Hoch-Temperatur Spektren. Den wohl umfangreichsten Datensatz in den Reflexionsspektren bezüglich Temperatur- und Wellenlängenbereich wurde für den Enstatit aufgenommen. Mit ihm ist sehr klar sehen, dass der temperaturabhängige Wellenlängenversatz der Moden bei längerwelligen Moden stärker ist als be kürzerwelligen, ein Verhalten welches auch bei Quarz und Olivin beobachtet werden konnte.

Wir konnten k aus den NIR Transmissionsspektren von Olivin berechnen. Mit den erhaltenen Daten haben wir die Entwicklung der Multiphononenanregungen bei tiefen (bis zu 10 K) und die Kristallfeldbanden sowohl bei tiefen als auch bei hohen (bis zu 773 K) Temperaturen untersucht. Die Multiphononenanregungen zeigten keine signifikante Änderung. Die Kristallfeldbanden allerdings zeigten einen Anstieg in ihrer Stärke für hohe Temperaturen und nur eine minimale Änderung bei tiefen Temperaturen im Vergleich zu den 300 K Spektren. Die Entwicklung der Bandenstärke konnte sehr gut mittels einer durch die Theorie vorhergesagten Kotangens-Hyperbolicus-Funktion des reziproken der Temperatur gefittet werden.

Mit Hilfe der temperaturabhängigen Oszillatorparameter von Korund und Spinell konnten wir zeigen, dass oblate Korundteilchen (wie durch Takigawa et al. (2012) vorhergesagt) mit einer Temperatur von etwa 551 K eher als Spinell für die bekannte 13 μm-Bande in den Spektren sauerstoffreicher AGB Sterne verantwortlich ist. Nach unseren Daten, können Spinellpartikel die 13 μm-Bande nur bedingt wiedergeben. Zudem haben wir eine Möglichkeit aufgezeigt wie temperaturabhängige Klein-Teilchenspektren von Olivin und Enstatit dafür verwedet werden können bei einem direkten Vergleich mit astronomischen Spektren von Staubscheiben um junge Sterne die Temperatur der dortigen Olivin- und Estatitpartikel zu bestimmen.

Appendices

A. Oscillator parameters of the reflectance fits

Table A.1.: Comparison of the fit parameters of corundum for the ordinary (E⊥c) and the extraordinary (E‖c) ray at four different temperatures. For the ordinary ray, all oscillators are of the E_u–type while for the extraordinary ray, only the respective first two oscillators are of the A_{2u}–type. The third oscillator could not be verified belonging to an A_{2u}-type mode.

		E⊥c					E‖c				
T(K)	j	ω_{TOj} (cm^{-1})	γ_{TOj} (cm^{-1})	ω_{LOj} (cm^{-1})	γ_{LOj} (cm^{-1})	ϵ_∞	ω_{TOj} (cm^{-1})	γ_{TOj} (cm^{-1})	ω_{LOj} (cm^{-1})	γ_{LOj} (cm^{-1})	ϵ_∞
300	1	384.02	6.03	387.46	5.18	3.05	399.68	4.68	511.05	1.42	2.9
	2	439.22	3.23	481.96	2.96		481.58	3.42	480.93	3.21	
	3	569.35	7.86	908.23	22.37		582	4.17	884.75	21.57	
	4	634.36	5.6	630.59	8.53						
551	1	380.83	6.13	383.22	6.55	3.06	394.76	11.2	508.09	2.79	2.91
	2	436	7.51	477.49	3.86		476.38	7.83	475.7	6.99	
	3	564.42	8.89	901.64	27.84		577.36	8.93	882.32	35.96	
	4	628.8	8.13	624.95	11.37						
738	1	379.9	9.86	382.36	8.56	3.08	391.91	18.58	505.24	2.88	2.91
	2	432.94	8.19	474.39	6.99		472	13.3	471	12.13	
	3	560.1	10.24	898.5	36.78		573.5	11.37	878.47	44.71	
	4	624.51	10.8	620.9	14.32						
928	1	377.51	10.97	379.8	10.1	3.1	390.54	22.57	502.65	3.22	2.97
	2	430.21	10.49	471.18	10.15		471.19	17.11	469.84	16.32	
	3	555.46	14.82	894.5	45.36		573.35	15.74	874.39	49.24	
	4	619.99	14.21	616.66	17.55						

Table A.2.: Comparison of the fit parameters of spinel. The frequencies indicated by a * represent the positions of the T_{1u}-type mode oscillators of a perfect spinel predicted by theory.

$T(K)$	j	ω_{TOj} (cm^{-1})	γ_{TOj} (cm^{-1})	ω_{LOj} (cm^{-1})	γ_{LOj} (cm^{-1})	ϵ_∞
10	1	231.8	21.44	232.41	20.9	2.8
	2	307.62*	11.6	310.95	12.12	
	3	429.03	137.32	443.05	111.55	
	4	480.47*	32.29	609.56	38.46	
	5	532.05*	60.75	557.19	67.34	
	6	579.01	84.33	543.14	124.05	
	7	670.03*	38.6	862.87	31.94	
	8	800.23	107.09	788.41	82.47	
100	1	231.79	15.6	232.12	14.9	2.87
	2	308.29*	10.58	311.59	11.27	
	3	429.75	140.93	445.87	114.81	
	4	482.06*	30.08	611.05	35.66	
	5	533.97*	61.9	560.36	61.92	
	6	581.92	77.1	544.65	137.8	
	7	674.92*	34.04	864.14	26.21	
	8	801.41	125.53	789.03	92.54	
300	1	231.05	8.97	231.58	8.29	2.77
	2	307.12*	12.65	310.73	13.68	
	3	427.11	134.26	442.85	112.26	
	4	481.53*	30.58	608.03	37.88	
	5	531.37*	55.1	558.16	70.14	
	6	581.8	74.64	546.32	120.96	
	7	672.28*	36.67	866.53	39.52	
	8	811.63	77.37	800.67	73.77	
551	1	226.96	9.99	227.54	9.41	2.8
	2	304.4*	16.38	308.36	17.02	
	3	426.34	139.54	438.44	108.65	
	4	475.24*	35.89	598.4	42.79	
	5	527.69*	63.05	553.85	74.68	
	6	576.95	74.12	547.55	122.79	
	7	662.28*	47.55	862.97	47.55	
	8	797.84	86.36	785.72	76.12	
738	1	230.02	9.79	230.34	9.18	2.82
	2	302.2*	20.15	306.49	20.68	
	3	438.12	140.41	444.8	96.33	
	4	469.66*	38.7	590.55	48.62	
	5	521.27*	65.86	549.66	79.03	
	6	569.98	75.11	542.25	126.64	
	7	655.42*	55.98	860.15	55.98	
	8	789.47	92.02	776.78	79.87	
928	1	227.33	13.81	227.78	13.45	2.77
	2	300.07*	20.15	304.01	20.58	
	3	440.49	140.09	442.56	97.23	
	4	466.52*	45.67	582.36	55.59	
	5	520.32*	76.53	546.93	82.07	
	6	563.9	73.29	544.39	126	
	7	649.32*	64.24	855.98	64.24	
	8	786.4	93.61	772.56	85.91	

Table A.3.: Comparison of the fit parameters of quarz for the ordinary (E⊥c) and the extraordinary ray (E∥c).

		E⊥c					E∥c				
T(K)	j	Ω_{TOj} (cm^{-1})	γ_{TOj} (cm^{-1})	Ω_{LOj} (cm^{-1})	γ_{LOj} (cm^{-1})	ϵ_∞	Ω_{TOj} (cm^{-1})	γ_{TOj} (cm^{-1})	Ω_{LOj} (cm^{-1})	γ_{LOj} (cm^{-1})	ϵ_∞
300	1	264.13	6.68	265.36	7.08	2.34	363.03	5.18	386.42	3.76	2.39
	2	393.55	4.25	402.88	4.33		494.99	10	552.82	5.3	
	3	449.78	3.43	507.89	2.87		775.58	8.48	789.17	6.51	
	4	694.3	11.91	697.31	12.11		1073.37	15.21	1238.42	16.41	
	5	795.36	7.75	808.72	8.11						
	6	1064.57	6.98	1226.34	10.91						
	7	1160.03	8.38	1157.02	7.98						
551	1	257.69	9.21	258.36	9.05	2.36	369.72	7.89	388.87	11.92	2.38
	2	395.03	5.26	401.96	4.88		486.1	17.85	547.22	10.28	
	3	445.61	4.9	504.58	7.88		775.09	13.78	785.37	15.29	
	4	695.37	13.54	697.13	12.52		1070.08	20.03	1237.02	30.04	
	5	790.2	13.44	804.58	13.02						
	6	1063.3	9.31	1221.61	18.66						
	7	1157.62	10.57	1155.85	9.98						
738	1	255.06	9.29	255.77	9.87	2.38	376.11	15.02	392.48	18.9	2.38
	2	396.5	10.44	402.99	11.05		473.93	23.83	540.15	14.12	
	3	438.27	9.28	499.84	9.29		775.27	19.98	782.47	20.58	
	4	688.59	15.17	688.99	14.51		1066.91	22.76	1234.71	39.73	
	5	786.14	16.97	799.52	16.62						
	6	1058.36	15.17	1217.97	20.43						
	7	1155.9	36.83	1153.29	34.45						
833	1	256.4	11.18	256.69	10.94	2.39	386.59	20.1	396.64	20.05	2.38
	2	400.14	12.7	404.6	11.83		465.2	24.9	533.84	17.53	
	3	432.7	11.19	495.08	10.62		777.02	31.45	782.29	30.85	
	4	680.64	38.36	680.51	37.27		1065.91	26.52	1239.85	50.93	
	5	782.98	19.92	796.81	20.2						
	6	1057.85	20.31	1220.69	31.12						
	7	1154.85	41.18	1154.19	39.93						
928	1	-	-	-	-	2.36	-	-	-	-	2.44
	2	-	-	-	-		442.2	30.04	527.43	24.19	
	3	423.04	11.85	491.45	12.18		-	-	-	-	
	4	-	-	-	-		1064.14	32.9	1240.89	55.58	
	5	780.28	22.85	793.68	26.32						
	6	1060.37	19.53	1226.38	43.43						
	7	-	-	-	-						

Table A.4.: Comparison of the fit parameters from the Lorentz fit of the reflection measurements on both olivine crystals C1 and D1 at four different temperatures. The denomination is the same as given in Eq. (2.38). For those values indicated as ∼0, a number <0.01 has been obtained during the fit procedure.

		E‖a (B_{1u}; C1)			E‖b (B_{2u}; D1)			E‖c (B_{3u}; C1)			E‖c (B_{3u}; D1)		
T(K)	j	ω_j	γ_j	σ_j	ω_j	γ_j	σ_j	ω_j	γ_j	σ_j	ω_j	γ_j	σ_j
300	1	287.95	16.55	1.2	281.21	19.61	2.15	292.77	52.97	1.02	291.31	23.4	0.31
	2	361.12	37.22	0.32	343.4	18.01	1.34	372.54	15.04	1.24	372.0	12.71	0.95
	3	403.23	9.78	0.19	389.77	13.82	0.45	400	10.91	1.39	399.95	13.69	1.4
	4	413.75	14.57	0.83	409.03	11.17	0.26	467.67	4.93	0.01	467.63	7.04	0.01
	5	473.74	9.74	0.09	450.07	15.13	0.17	498.13	19.68	0.38	498.07	19.66	0.33
	6	499.95	19.96	0.43	502.21	22.77	0.1	545.48	12.48	0.01	545.98	7.46	0.01
	7	873.83	23.25	0.54	523.54	15.26	0.15	599.71	20	0.26	600.47	21.61	0.24
	8	960.14	6.38	∼0	836.77	8.66	0.09	840.87	8.17	∼0	839.67	13.02	0.01
	9				871.67	13.24	0.41	953.17	8.18	0.09	952.02	10.79	0.09
	10				979.38	13.61	0.01	978.09	19	0.42	975.09	17.02	0.24
	11									996.32	18.87	0.11	
		ϵ_∞=2.43			ϵ_∞=2.67			ϵ_∞=3.01			ϵ_∞=2.74		
551	1	284.16	19.38	1.14	276.2	28.56	2.25	291.74	53.42	0.93	287.32	25.11	0.28
	2	356.83	47.1	0.29	337.28	22.47	1.2	365.4	20.97	1.19	365.42	20.43	0.92
	3	397.72	16.65	0.15	386.41	18.08	0.4	395.05	17.04	1.42	395.72	20.13	1.34
	4	408.27	19.62	0.82	403.41	17.35	0.33	467.28	6.05	∼0	465.84	8	∼0
	5	469.89	9.25	0.03	445.44	24.27	0.17	494.75	31.97	0.41	495.09	30.15	0.34
	6	494.82	26.97	0.48	497.6	20.86	0.07	542.97	14.18	0.01	542.67	9.03	0.01
	7	869.15	26.06	0.54	519.73	23.94	0.19	596.65	26.91	0.27	597.46	27.18	0.24
	8	954.6	8.7	∼0	833.43	14.58	0.13	840.75	8.23	∼0	839.18	13.03	∼0
	9				867.36	13.7	0.38	947.67	11.17	0.11	946.41	14.6	0.11
	10				973.64	12.82	0.01	972.03	20.79	0.42	969.28	18.95	0.25
	11										990.77	18.59	0.08
		ϵ_∞=2.39			ϵ_∞=2.69			ϵ_∞=3.01			ϵ_∞=2.67		
738	1	280.26	24.65	1.25	272.24	33.89	2.36	290.95	53.92	0.8	285.7	25.13	0.18
	2	355.75	47.94	0.24	333.45	23.05	1.07	360.27	24.99	1.15	361.25	21.91	0.73
	3	399.3	19.98	0.35	384.2	22.72	0.45	391.3	22.99	1.47	392.84	25.34	1.51
	4	405.43	25.06	0.59	400.53	19.22	0.3	467.07	6.32	∼0	465.84	8.07	∼0
	5	466.29	9.37	0.02	441.88	33.27	0.18	492.51	37.29	0.41	493.49	37.23	0.36
	6	491.42	29.97	0.5	495.69	30.87	0.07	541.21	15.18	0.01	542.15	9.43	∼0
	7	865.28	27.32	0.54	516.61	28.72	0.21	595.8	31.9	0.28	596.5	32.14	0.26
	8	949.49	9.58	∼0	829.98	17.48	0.15	840.72	8.31	∼0	839.13	13.08	∼0
	9				862.83	15.13	0.36	941.84	13.29	0.12	941	16.52	0.13
	10				968.59	15.76	0.01	966.85	22.72	0.4	964.38	21.68	0.27
	11										986.18	19.3	0.07
		ϵ_∞=2.39			ϵ_∞=2.69			ϵ_∞=2.99			ϵ_∞=2.74		
928	1	278.92	27.59	1.17	270.59	36.39	2.12	290.78	54.62	0.74	284.11	21.62	0.16
	2	354.42	48.61	0.2	329.69	26.6	1.06	354.66	28.87	1.02	357.11	23.79	0.57
	3	396.82	21.1	0.46	386.99	29.37	0.66	387.43	28.39	1.59	389.9	31.07	1.59
	4	405.99	27.77	0.44	400.83	20.09	0.17	467.32	6.5	∼0	465.55	8.18	∼0
	5	466.34	9.42	∼0	439	32.42	0.16	491.81	41.7	0.4	492.58	41.52	0.35
	6	488.65	35.11	0.54	489.34	39.95	0.03	540.69	15.58	0.01	541.48	9.56	∼0
	7	860.49	32.22	0.55	513.48	33.6	0.3	594.35	36.18	0.3	595.38	36.14	0.28
	8	944.06	10.91	∼0	827.95	20.16	0.19	840.69	8.38	∼0	839.11	13.1	∼0
	9				858.62	16.29	0.35	937.22	16.06	0.13	935.84	19.19	0.13
	10				963.9	19.42	0.01	961.76	25.71	0.41	959.62	24.93	0.29
	11										981.6	20.22	0.06
		ϵ_∞=2.39			ϵ_∞=2.78			ϵ_∞=3.02			ϵ_∞=2.78		

Table A.5.: Comparison of the fit parameters from the Lorentz fit of the reflection measurements on both pieces of the enstatite crystal from Burma at four different temperatures. The denomination is the same as given in Eq. (2.38). For those values indicated as ∼0, a number <0.01 has been obtained during the fit procedure.

		E‖a (B_{2u})			E‖b (B_{3u})			E‖c (B_{1u})		
T(K)	j	ω_j	γ_j	σ_j	ω_j	γ_j	σ_j	ω_j	γ_j	σ_j
10	1	176.77	∼0	0.02	219.9	6.86	1.4	140.97	10.5	0.15
	2	203.39	10.55	0.26	239.22	7	0.12	193.54	7.84	0.1
	3	229.99	0.83	0.02	268.27	8.67	0.5	227.67	1.23	∼0
	4	238.88	10.36	0.18	293.6	10.31	0.08	232.86	7.56	0.25
	5	283.43	18.72	0.81	334.2	17.39	0.13	276.27	12.18	0.11
	6	301.37	10.11	0.38	349.77	7.91	0.52	325.02	12.59	0.07
	7	313.21	7.79	0.83	376.38	4.35	0.03	364.79	47.37	0.52
	8	322.93	4.52	0.75	406.4	16.12	0.04	402.73	7.55	0.51
	9	346.83	4.62	0.16	458.62	6.74	0.11	458.18	9.28	0.63
	10	368.82	6.66	0.03	477.73	20.52	1.01	502	7.23	1.11
	11	397.7	19.38	0.1	547.49	5.31	0.02	535.82	6.55	0.14
	12	417.26	10.55	0.11	564.66	5.46	0.03	568.83	14.33	0.04
	13	434.25	3.93	0.06	724.62	8.87	0.05	651.82	20.02	0.04
	14	446.03	5.47	0.11	744.91	9.08	0.02	691.34	9.81	0.04
	15	499.73	14.72	0.04	892.85	13.6	0.19	855.09	13.17	0.32
	16	520.73	8.31	0.06	918.57	12.46	0.04	930.14	15.36	0.25
	17	540.98	9.37	0.04	1019.29	15.48	0.08	974.57	7.68	0.01
	18	553.39	7.49	0.08	1072.6	12.95	0.21	1005.22	9.61	0.01
	19	643.64	9.33	0.08				1038.2	10.51	0.01
	20	677.89	6.08	0.01				1129.93	7.47	0.01
	21	944.53	15.22	0.44						
	22	1010.74	9.31	0.03						
	23	1056.28	13.01	0.18						
	24	1147.68	10.07	∼0						
			ϵ_∞=2.78			ϵ_∞=2.84			ϵ_∞=2.75	
100	1	176.57	0.93	0.06	219.08	6.27	1.47	139.55	11.57	0.18
	2	198.08	7.68	0.47	238.69	6.48	0.11	193.08	6.91	0.1
	3	229.92	3.1	0.05	267.83	9.54	0.53	227.09	1.12	∼0
	4	240.46	10.22	0.2	294.39	10.78	0.06	233.35	7.93	0.23
	5	285.47	15.42	0.69	332.2	16.8	0.16	277.25	11.97	0.1
	6	302.28	10.23	0.45	348.8	8.21	0.55	324.88	12.69	0.07
	7	313.45	7.33	0.68	376.1	4.96	0.03	364.34	46.59	0.5
	8	322.93	4.91	0.75	407.64	15.32	0.04	402.59	7.61	0.52
	9	346.37	4.89	0.16	458.67	8.01	0.14	458.05	9.75	0.64
	10	368.29	6.46	0.03	476.6	18.74	1.02	501.74	7.4	1.11
	11	397.29	20.94	0.1	547.27	5.76	0.02	535.66	7.05	0.13
	12	417.72	12.24	0.12	564.33	5.42	0.03	568.89	13.68	0.04
	13	434.17	3.67	0.05	724.42	9.14	0.05	654.61	21.26	0.04
	14	446.11	5.31	0.11	744.93	8.77	0.01	691.69	8.77	0.04
	15	499.69	12.33	0.04	892.59	13.96	0.2	855.14	12.69	0.33
	16	520.21	10.16	0.07	918.44	12.59	0.04	930.03	14.27	0.26
	17	540.86	9.22	0.04	1019.14	15.93	0.08	974.24	7.43	0.01
	18	553.1	7.92	0.08	1071.94	12.54	0.21	1004.93	9.58	0.01
	19	644.15	8.5	0.07				1037.81	10.65	0.01
	20	677.31	5.3	0.01				1130.1	6.95	0.01
	21	944.19	14.81	0.44						
	22	1010.62	9.59	0.03						
	23	1055.64	12.78	0.18						
	24	1146.77	12.08	∼0						

Continued

		E‖a			E‖b			E‖c		
T(K)	j	ω_j	γ_j	σ_j	ω_j	γ_j	σ_j	ω_j	γ_j	σ_j
		ϵ_∞=2.78			ϵ_∞=2.84			ϵ_∞=2.75		
200	1	177.76	0.63	0.02	216.49	6.46	1.7	138.08	11.72	0.24
	2	199.69	7.28	0.19	237.89	6.11	0.1	193.43	5.85	0.06
	3	227.27	2.36	0.02	266.9	9.02	0.49	226.99	0.86	0.01
	4	242.18	9.43	0.06	294.8	12.17	0.07	232.63	6.65	0.19
	5	286.22	14.13	0.29	334.7	12.25	0.11	276.15	11.39	0.08
	6	301.74	10.78	0.15	347.09	8.41	0.55	324.34	12.66	0.06
	7	313.85	8.84	0.63	375.92	5.77	0.04	364.65	46.1	0.49
	8	323.71	6.08	1.14	407.96	14.1	0.02	402.01	8.61	0.53
	9	345.51	6.02	0.2	458.86	6.27	0.13	457.61	11.58	0.65
	10	367.95	9.51	0.05	475.36	15.08	1.04	501.09	7.95	1.12
	11	395.31	22.52	0.09	546.47	7.57	0.02	535.3	7.94	0.13
	12	417.24	13.5	0.13	563.34	5.94	0.03	568.13	17.04	0.04
	13	433.65	4.96	0.06	723.96	11.16	0.05	652.08	25.84	0.04
	14	445.51	6.76	0.13	744.54	9.06	0.01	690.61	12.14	0.05
	15	501.38	11.56	0.03	892.07	14.88	0.21	855.92	13.17	0.33
	16	520.33	11.04	0.07	918.26	13.03	0.04	929.91	14.67	0.28
	17	539.53	9.64	0.04	1018.39	16.4	0.09	973.72	7.71	0.01
	18	552.53	9.04	0.09	1070.47	11.77	0.21	1004.64	10.13	0.01
	19	643.6	10.23	0.08				1036.59	11.32	0.01
	20	676.77	5.12	∼0				1128.87	7.73	0.01
	21	943.75	15.09	0.46						
	22	1010.01	11.54	0.03						
	23	1054.42	12.77	0.18						
	24	1145.81	13.12	∼0						
		ϵ_∞=2.78			ϵ_∞=2.84			ϵ_∞=2.75		
300	1	178.53	2.19	0.05	218.13	8.95	1.32		-	
	2	198.81	10.5	0.22	237.89	8.17	0.07	190.14	2.91	0.05
	3	228.11	2.76	0.05	267.42	9.08	0.47	228.06	9.06	0.18
	4	239.79	9.9	0.01	291.88	13.43	0.08	234.07	3.91	0.05
	5	286.48	13.48	0.29	332.5	9.42	0.07	284.26	10.82	0.06
	6	302.36	10.83	0.16	344	12.71	0.68	322.57	16.3	0.1
	7	313.08	10.06	0.48	375.11	7.6	0.04	344.68	16.45	0.11
	8	322.24	8.99	1.36	408.21	14.31	0.04	401.56	11.09	0.6
	9	343.77	10.39	0.22	457.34	11.36	0.12	459.01	14.5	0.66
	10	366.74	11.93	0.06	474.88	16.58	1.02	499.39	11.28	1.28
	11	395.58	22.88	0.1	545.19	9.61	0.02	534.71	10.19	0.15
	12	415.19	15.73	0.15	562.09	7.8	0.03	565.99	18.13	0.04
	13	431.75	8.26	0.07	723.74	10.89	0.05	651.64	17.5	0.03
	14	442.99	7.95	0.1	744.12	8.5	0.01	690.35	13.77	0.05
	15	499.16	11.11	0.01	891.95	17.97	0.23	855.29	15.72	0.36
	16	519.82	10.48	0.05	917.37	16.29	0.04	929.3	19.25	0.28
	17	539.11	9.66	0.02	1016.32	16.72	0.09	973.72	10.04	0.01
	18	551.41	11.92	0.11	1070.6	13.99	0.21	1004.54	12.46	∼0
	19	640.86	13.54	0.09				1034.82	14.05	0.01
	20	676.76	5.07	∼0				1125.9	12.96	0.02
	21	944.61	17.84	0.47						
	22	1008.14	13.94	0.03						
	23	1056.12	13.3	0.18						
	24	1145.71	13.41	∼0						
		ϵ_∞=2.78			ϵ_∞=2.84			ϵ_∞=2.75		
551	1	178.56	1.94	0.06	213.92	10.92	1.29		-	
	2	196.57	12.37	0.25	237.19	8.52	0.03	181.63	1.67	0.01
	3	223.85	10.93	0.11	264	12.86	0.47	228.35	4.13	0.04

Continued

		E‖a			E‖b			E‖c		
T(K)	j	ω_j	γ_j	σ_j	ω_j	γ_j	σ_j	ω_j	γ_j	σ_j
	4	238.11	10.41	0.01	289.04	13.64	0.07	232.53	7.15	0.08
	5	283.74	13.94	0.3	333.45	14.9	0.3	285.77	21.37	0.11
	6	305.61	10.8	0.23	339.67	18.04	0.41	315.22	17.97	0.08
	7	315.95	12.56	0.04	371.42	9.44	0.05	340.69	24.86	0.17
	8	318.84	13.09	1.66	407.94	14.34	0.01	398.39	16.03	0.55
	9	338.2	14.43	0.18	456.78	12.04	0.06	458.79	21.42	0.62
	10	363.55	20.1	0.1	471.73	22.2	1.07	496.66	16.47	1.28
	11	391.66	28.42	0.1	540.39	15.15	0.03	531.02	15.62	0.14
	12	410.91	21.02	0.15	557.01	12.96	0.04	560.97	32.99	0.05
	13	427.79	16.22	0.1	720.56	13.01	0.04	648.53	34.89	0.03
	14	438.46	12.99	0.08	743.6	8.81	0.01	686.75	19.04	0.05
	15	499.15	11.22	∼0	889.14	23.76	0.24	855.12	20.09	0.35
	16	516.59	13.91	0.04	916.07	19.85	0.04	926.07	21.98	0.28
	17	537.24	12.91	0.02	1011.74	19.39	0.09	969.8	13.06	0.01
	18	548.06	18.17	0.11	1064.34	16.39	0.21	1001.39	17.1	0.01
	19	638.52	19.7	0.09				1029.06	18.05	0.01
	20	676.07	6	∼0				1120.85	15.86	0.01
	21	940.7	20.87	0.5						
	22	1004.94	17.9	0.04						
	23	1049.62	15.27	0.18						
	24	1142.07	18.93	∼0						
		ϵ_∞=2.79			ϵ_∞=2.9			ϵ_∞=2.76		
738	1	176.69	1.34	0.03	211.64	12.43	1.24		-	
	2	189.6	10.7	0.14	237.03	8.46	0.04	180.97	1.38	0.01
	3	218.82	11.9	0.1	260.44	15.6	0.47	227.53	12.13	0.19
	4	238.02	10.47	∼0	288.14	14.14	0.05	231.34	7.74	∼0
	5	278.46	22.21	0.21	329.64	19.78	0.46	284.43	24.84	0.09
	6	304.33	6.09	0.11	337.98	19.63	0.24	311.69	15.77	0.06
	7	315.89	11.92	1.04	368.52	12.46	0.06	335.16	27.49	0.17
	8	321.99	15.38	0.58	407.11	14.17	0.02	394.24	21.68	0.6
	9	334.4	17.36	0.22	458.24	11.54	0.11	455.65	26.07	0.61
	10	359.55	23.88	0.14	469.49	23.66	1.06	493.18	21.59	1.24
	11	385.88	29.17	0.11	536.63	19.34	0.03	528.48	17.7	0.11
	12	406.36	20.49	0.13	553.06	15.62	0.04	553.68	47.98	0.08
	13	424.21	18.7	0.1	718.33	14.96	0.04	645.4	38.8	0.02
	14	434.91	19.61	0.12	743.2	8.99	∼0	684.44	24.75	0.04
	15	493.08	12.52	0.01	885.58	28.4	0.27	854.44	25.62	0.33
	16	513.42	16.87	0.03	915.17	22.62	0.04	922.97	25.86	0.28
	17	533.72	17.76	0.02	1007.23	23.29	0.1	966.43	17.3	0.01
	18	544.71	25.47	0.12	1058.71	17.12	0.2	998.22	20.93	∼0
	19	635.06	21.68	0.09				1024.57	22.35	0.01
	20	674.5	6.75	∼0				1115.7	20.34	0.01
	21	937.08	23.92	0.51						
	22	1001.83	22.22	0.04						
	23	1044.21	17.13	0.18						
	24	1142.39	24.91	∼0						
		ϵ_∞=2.85			ϵ_∞=2.89			ϵ_∞=2.76		
928	1	179.45	1.9	0.02	208.46	14.29	1.13		-	
	2	188.37	12.32	0.11	236.77	8.52	∼0	180.94	1.49	∼0
	3	220.43	11.67	0.06	259	16.79	0.4	225.44	14.32	0.14
	4	238.07	10.54	∼0	288.24	14.4	0.03	230.91	7.8	0.02
	5	278.27	21.83	0.08	326.3	21.57	0.48	285	24.71	0.11
	6	304.98	6.56	0.03	338.91	20.09	0.15	311.91	16.5	0.1
	7	314.73	13.56	1.19	368.17	13.1	0.06	334.4	27.74	0.13
	8	323.1	16.71	0.4	407.02	14.18	∼0	391.63	23.78	0.51

Continued

		E‖a			E‖b			E‖c		
T(K)	j	ω_j	γ_j	σ_j	ω_j	γ_j	σ_j	ω_j	γ_j	σ_j
	9	333.55	18.42	0.18	460.16	11.34	0.22	453.52	26.9	0.48
	10	357.34	24.56	0.18	469.84	29.51	0.94	491.26	29.36	1.47
	11	386.06	29.82	0.15	535.3	22.24	0.04	527.11	20.52	0.1
	12	406.01	21.54	0.14	550.12	16.47	0.04	553.52	50.43	0.07
	13	424.88	19.81	0.12	717.5	15.37	0.03	644.65	39.76	0.02
	14	436.26	22.68	0.07	743.14	9.02	$\sim$0	682.56	25.24	0.04
	15	492.95	12.56	$\sim$0	882.38	30.39	0.27	854.2	32.54	0.35
	16	514.08	17	0.03	915.6	23.71	0.03	918.53	30.75	0.29
	17	532.52	18.09	0.04	1002.72	25.06	0.1	963.81	19.5	0.01
	18	545.81	26.64	0.09	1053.43	19.73	0.21	994.62	23.54	$\sim$0
	19	632.06	24.15	0.09				1020.21	24.89	0.01
	20	674.35	7.03	$\sim$0				1113.72	21.2	0.01
	21	933.25	27	0.54						
	22	998.08	25.6	0.04						
	23	1038.34	19.21	0.17						
	24	1133.4	24.74	$\sim$0						
		ϵ_∞=2.85			ϵ_∞=2.91			ϵ_∞=2.83		

Bibliography

N.W. Ashcroft and D.N. Mermin. *Festkörperphysik*. Oldenbourg, München, 2007.

A.S. Barker. Infrared lattice vibrations and dielectric dispersion in corundum. *Physical Review*, 132:1474–1481, 1964a.

A.S. Barker. Transverse and longitudinal optic modes study in mgf_2 and znf_2. *Physical Review*, 136 No 5A:1290–1295, 1964b.

B. Begemann, J. Dorschner, Th. Henning, and H. Mutschke. Aluminum oxide and the opacity of oxygen-rich circumstellar dust in the 12-17 micron range. *The Astrophysical Journal*, 640:199–208, 1997.

D. Billard, F. Gervais, and B. Piriou. Analysis of multiphonon absorption in corundum. *Phys. stat. sol.*, 75:117, 1976.

J.A.D.L. Blommaert, E. Vanhollebeke, J. Cami, M.A.T. Groenewegen, H. J. Habing, F. Markwick-Kemper, A. Omont, M. Schultheis, A.G.G.M. Tielens, L.B.F.M. Waters, and P. R. Wood. The dust sequence along the agb. In F. Kerschbaum, C. Charbonnel, and R.F. Wing, editors, *WHY GALAXIES CARE ABOUT AGB STARS*. ASP, 2007.

Graig F. Bohren and Donald R. Huffman. *Absorption and Scattering of Light by Small Particles*. John Wiley and Sons, New York, 1983.

N. Boudet and H. Mutschke. Temperature dependence of the submillimeter absorption coefficient of amorphous silicate grains. *the Astrophysical Journal*, 633:272, 2006.

J.E. Bowey, C. Lee, C. Tucker, A.M. Hofmeister, P.A.R. Ade, and M.J. Barlow. Temperature effects on the 15-85 μm spectra of olivines and pyroxenes. *Mon. Not. R. Astron*, 325: 886896, 2001.

J.P. Bradley. The astromineralogy of interstellar dust particles. In Th. Henning, editor, *Astromineralogy*. Springer, 2003.

R.G. Burns. *Mineralogical Applications of Crystal Field Theory, 2nd ed.* Cambridge University Press, Cambridge, 1993.

H. Chihara, C. Koike, and A. Tsuchiyama. Low-temperature Optical Properties of Silicate Particles in the Far-Infrared Region. *Publ. Astr. Soc. Japan*, 53:243–250, 2001.

R.A. Cowley. The lattice dynamics of an anharmonic crystal. *Advances in Physics*, 12: 421–480, 1963.

K.L. Day. Temperature dependence of mid-infrared silicate absorption. *Astrophys. J., Lett.*, 203, No 2:L99–L101, 1976.

A. Debernardi and M. Cardona. Isotopic effects on the lattice constant in compound semiconductors by perturbation theory: An ab initio calculation. *Physical Review B*, 54, No 11:305–310, 1996.

R. Demichelis, H. Suto, Y. Noel, H. Sogawa, T. Naoi, C. Koike, H. Chihara, N. Shimobayashi, M. Ferrabone, and R. Dovesi. The infrared spectrum of ortho-enstatite from reectance experiments and first-principle simulations. *Mon. Not. R. Astron. Soc.*, 420:147–154, 2012.

K. DePew, A. Speck, and C. Dijkstra. Astromineralogy of the 13 m feature in the spectra of oxygen-rich asymptotic giant branch stars. i. corundum and spinel. *The Astrophysical Journal*, 640:971–981, 2006.

B.T. Draine and P.J. Flatau. Discrete dipole approximation for scattering calculations. *J. Opt. Soc. Am. A,*, 11:1491–1499, 1994.

J.L. Escamilla-Reyes and E. Haro-Poniatowski. Anharmonic coefficients in high symmetry directions for the diamond structure. *Revista Mexicana De Fisica*, 51:452–460, 2005.

D. Fabian. *optische Eigenschaften und strukturelle Umwandlungen ausgewaehlter Silikate und Oxide als Analoga des kosmischen Staubes*. PhD thesis, FSU Jena, 2002.

D. Fabian, C. Jäger, Th. Henning, J. Dorschner, and H.Mutschke. Steps toward interstellar silicate mineralogy, V-Thermal evolution of amorphous magnesium silicates and silica. *A&A*, 364:282–292, 2000.

D. Fabian, T. Henning, C. jger, H. Mutschke, J. Dorschner, and O. Wehrhan. Steps toward interstellar silicate mineralogy, VI-Dependence of crystalline olivine IR spectra on iron content and particle shape. *A&A*, 378:228–238, 2001.

G. Fiquet, P. Richet, and G. Montagnac. High-temperature thermal expansion of lime, periclase, corundum and spinel. *Phys. Chem. Minerals*, 27:103–111, 1999.

H.P. Gail. Formation and Evolution of Minerals in Accreation Discs and Stellar Outflows. In Th. Henning, editor, *Astromineralogy*. Springer, 2003.

H.P. Gail and E. Sedlmayr. Inorganic dust formation in astrophysical environments. *Faraday Discuss.*, 109:303–319, 1998.

F. Gervais and B. Piriou. Anharmonicity in several-polar-mode crystals: adjusting phonon self-energy of LO and TO modes in Al_2O_3 and TiO_2 to fit infrared reflectivity. *J. Phys. C: Solid State Phys.*, 7:2374–2385, 1974.

F. Gervais and B. Piriou. Temperature dependence of transverse and longitudinal optic modes in the α and β phases of quartz. *Physical Review B*, 11, No. 10:3944–3950, 1975.

A. El Goresy, P. Dera, T.G. Sharpand, C.T. Prewitt, M. Chen, L. Dubrovinsky, B. Wopenka, N. Z. Boctor, and R. J. Hemley. Seifertite, the dense orthorhombic polymorph of silica from the Martian meteorites Shergotty and Zagami. *European Journal of Mineralogy*, 20: 523–528, 2008.

E. Grüneisen. Theorie des festen Zustandes einatomiger Elemente. *Annalen der Physik*, 12, 1912.

M.S. Hanner. The Mineralogy of Cometary Dust. In Th. Henning, editor, *Astromineralogy*. Springer, 2003.

W.K. Hartmann. *Moons and Planets, 5th ed.* Thomson, Belmont, CA, 2005.

Th. Henning. Cosmic silicates: a review. In V. Pirronello, J. Krelowski, and L. Manico, editors, *Solid-State Astrochemistry*. Kluwer, 2003a.

Th. Henning. Laboratory Astrophysics of Cosmic Dust Analogues. In Th. Henning, editor, *Astromineralogy*. Springer, 2003b.

Th. Henning and H. Mutschke. Low-temperature infrared properties of cosmic dust analogues. *A&A*, 327:743–754, 2003.

W. Hinz. *Silikate - Grundlagen der Silikatwissenschaft und Silikattechnik*. VEB - Verlag fr Bauwesen, Berlin, 1970.

D.R. Huffman. Total Intensities of Some Crystal Field Transitions in MnO and MnS Related to the Antiferromagnetism. *Journal of Applied Physics*, 40:1334–1335, 1969.

K. Iishi. Lattice Dynamics of Corundum. *Phys. Chem. Minerals*, 3:1–10, 1978.

I.P. Ipatova, A.A. Maradudin, and R.F. Wallis. Temperature Dependence of the Width of the Fundamental Lattice-Vibration Absorption Peak in Ionic Crystals: II Approximate Numerical Results. *Physical Review*, 155 No 3:882–895, 1967.

J.R. Jasperse, A. Kahn, J.N. Plendl, and S.S. Mitra. Temperature dependence of infrared dispersion in ionic crystals lif and mgo. *Physical Review*, 146, No 2:526–542, 1966.

A. Juhasz, J. Bouwman, Th. Henning, B.Acke, M.E. van den Ancker, G. Meeus, C. Dominik, M. Min, A.G.G.M. Tielens, and L.B.F.M. Waters. Dust evolution in protoplanetary disks around herbig ae/be stars - the spitzer view. *The Astrophysical Journal*, 721:431–455, 2010.

C. Klein and C.S. Hurlbut. *Manual of Mineralogy (after J.D. Dana).* Wiley, New York, 1999.

C. Koike, H. Mutschke, H. Suto, T. Naoi, H. Chihara, Th. Henning, C. Jäger, A. Tsuchiyama, J. Dorschner, and H. Okuda. Temperature effects on the mid- and far-infrared specra of olivine particles. *A&A*, 449:583–596, 2006.

D.L. Lakshtanov, S.V. Sinogeikin, and J.D. Bass. High-temperature phase transitions and elasticity of silica polymorphs. *Phys. Chem. Minerals*, 34:11–22, 2007.

Th. Lebzelter, Th. Posch, K. Hinckle, P.R. Wood, and J. Bouwman. Tracing the development of dust around evolved stars - the case of 47 tuc. *The Astrophysical Journal*, 53:L145L148, 2006.

I. Levin and D. Brandon. Metastable Alumina Polymorphs: Crystal Structures and Transition Sequences. *Journal of the American Ceramic Society*, 81:1–8, 1998.

Z. Lodziana and K. Parlinski. Dynamical stability of the alpha and theta phases of alumina. *Physical Review B*, 67, 2003.

R.P. Lowndes. Influence of lattice anharmonicitiy on the longitudinal optic modes of cubic ionic solids. *Physical Review B*, 1:2754–2763, 1970.

A.A. Maradudin and A.E. Fein. Scattering of neutrons by an anharmonic crystal. *Physical Review*, 128 No 6:2589–2608, 1962.

S. Matthes. *Mineralogie.* Springer, Berlin, 1990.

V. Menella, J.R. Brucato, L. Colangell, P.Palumbo, A. Rutundi, and E. Bussoletti. Temperature dependence of the absorption coefficient os cosmic analog grains in the wavelength range 20 microns to 2 millimeters. *the Astrophysical Journal*, 496:1058–1066, 1998.

M. Min, J.W. Hovenier, C. Dominik, A. de Koter, and M.A. Yurkin. Absorption and scattering properties of arbitrarily shaped particles in the rayleigh domain: a rapis computational method and a theoretical foundation for the statistical approach. *Journal of Quantitative Spectroscopy & Radiative Transfer*, 97:161–180, 2008.

F.J. Molster and L.F.B.M. Waters. The mineralogy of interstellar and circumstellar dust. In Th. Henning, editor, *Astromineralogy.* Springer, 2003.

K. Momma and F. Izumi. VESTA 3 for three-dimensional visualization of crystal, volumetric and morphology data. *J. Appl. Crystallogr.*, 44:1272–1276, 2011.

K. Murata. *Crystallization Processes of circumstellar Silicate Dust.* PhD thesis, Department of Earth and Space Science, Graduate School of Science, Osaka University, 2009.

M.P. O'Horo, A.L. Frisillo, and W.B. White. Lattice vibrations of $mgal_2o_4$ spinel. *Physics and Chemistry of Solids*, 34:23–28, 1973.

K.M. Pittman, A.M. Hofmeister, and A.K. Speck. Revisiting astronomical crystalline forsterite in the UV to near-IR. *Earth Planets Space*, 65:129–138, 2013.

Th. Posch, F. Kerschbaum, H. Mutschke, D. Fabian, J. Dorschner, and J. Hron. On the origin of the 13μm feature - a study of iso-sws spectra of oxygen rich agb stars -. *A&A*, 352:609–618, 1999.

Th. Posch, F. Kerschbaum, H. Mutschke, D. Fabian, D. Clement, and J. Dorschner. Features of oxide dust particles in circumstellar shells of AGB stars. *ESA Publication Series*, SP 511:141–144, 2003.

J. Preudhomme and P. Tarte. Infrared studies of spinels-iii - the normal ii-iii spinels. *Spectrochim. Acta*, 27A:1817–1835, 1972.

M. Schall. *Phononenprozesse und Ladungstrgerdynamik in Halbleitern.* PhD thesis, Albert-Ludwigs-Universitt-Freiburg, 2001.

Scilab Consortium. *Scilab: The free software for numerical computation.* Scilab Consortium, Paris, France, 2011. URL `http://www.scilab.org`.

J.F. Scott and S.P.S. Porto. Longitudinal and transverse optical lattice vibrations in quartz. *Physical Review*, 161, No 3:903–910, 1967.

T.J. Shankland and U. Nitsan. Optical Absorption and radiative Heat Transport in Olivine at High Temperature. *Journal of Geophysical Research*, 84 No.B4:1603–1609, 1979.

R.M. Sova, M.J. Linevsky, M.E. Thomas, and F.F. Mark. High-temperature infrared properties of sapphire, alon, fused silica, yttria, and spinel. *Infrared Physics & Technology*, 39: 251–261, 1998.

A.K. Speck. *The Mineralogy of Dust Around Evolved Stars.* PhD thesis, University College London, 1998.

W. G. Spitzer and D. A. Kleinman. Infrared Lattice Bands of Quartz. *Physical Review*, 121: 1324–1335, 1961.

H. Suto, H. Sogawa, S. Tachibana, C. Koike, H. Karoji, A. Tsuchiyama, H. Chihara, K. Mizutani, J. Akedo, K. Ogiso, T. Fukui, and S. Ohara. Low-temperature single crystal reflection spectra of forsterite. *Mon. Not. R. Astron. Soc.*, 370:1599–1606, 2006.

A. Takigawa, S. Tachibana, H. Nagahara, and K. Ozawa. Anisotropic Evaporation and Condensation of Circumstellar Corundum. *Lunar and Planetary Science Conference*, 43, 2012.

A. Tamanai, H.Mutschke, J. Blum, and G. Meeus. The $10\mu m$ infrared band of silica dust: A laboratory study comparing the Aerosol and KBr pellet Techniques. *the Astrophysical Journal*, 648:L147–L150, 2006.

P. Thibaudeau and F. Gervais. Ab initio investigation of phonon modes in the MgAl204 spinel. *J. Phys.: Condens. Matter*, 14:3543–3552, 2002.

P. Thibaudeau, A. Debernardi, V. Ta Phoc, S. da Roche, and F. Gervais. Phonon anharmonicity in disordered MgAl2O4 spinel. *Physical review B*, 63:1–7, 2006.

M.E. Thomas. Temperature Dependence of the Complex Index of Refraction. In E.D. Palik, editor, *Handbook of Optical Constants of Solids*. Academic Press, 1991.

M.E. Thomas, R.I. Joseph, and W.J. Tropf. Infrared transmission properties of sapphire, spinel, yttria, and ALON as a function of temperature and frequency. *Applied Optics*, 27: 239–245, 1988.

M.E. Thomas, S.K. Andersson, R.M. Sova, and R.I. Joseph. Frequency and temperature dependence of the refractive index of sapphire. *Infrared Physics & Technology*, 39:235–249, 1998.

R.S. Tripathi and K.N. Pathak. Self Energy of Photons in an Anharmonic Crystal to $O(\lambda^4)$. *International Atomic Energy Agency*, 117, 1973.

W.J. Tropf and M.E. Thomas. Magnesium Aluminum Spinel. In E.D. Palik, editor, *Handbook of Optical Constants of Solids II*. Academic Press, 1991.

K. Ullrich, K. Langer, and K.D. Becker. Temperature dependence of the polarized electronic absorption spectra of olivines. Part I - fayalite. *Phys Chem Minerals*, 29:409–419, 2002.

S. Zeidler, T. Posch, H. Mutschke, H. Richter, and O. Wehrhan. Near-infrared absorption properties of oxygen-rich stardust analogs - The influence of coloring metal ions. *A&A*, 526:A68 1–10, 2011.

S. Zeidler, T. Posch, and H. Mutschke. Optical Constants of Refractory Oxides at High Temperatures - The Mid-infrared Properties of Corundum, Spinel and α-Quartz. *A&A*, accepted, 2013.

Ehrenwörtliche Erklärung

Ich erkläre hiermit ehrenwörtlich, dass ich die vorliegende Arbeit selbständig, ohne unzulässige Hilfe Dritter und ohne Benutzung anderer als der angegebenen Hilfsmittel und Literatur angefertigt habe. Die aus anderen Quellen direkt oder indirekt übernommenen Daten und Konzepte sind unter Angabe der Quelle gekennzeichnet.

Bei der Auswahl und Auswertung folgenden Materials haben mir die nachstehend aufgeführten Personen unentgeltlich geholfen:

- **Dr. Harald Mutschke** – helfend bei der Probenauswahl; gab wertvolle Hinweise und Tipps zur Auswertung und Darstellung der Messergebnisse
- **Fr. Gabriele Born** – Probenvorbereitung (sägen und polieren der Kristalle); EDX-Analysen
- **Dr. Thomas Posch** – Stellte die AGB-Sternspektren sowie die Berechnungen zum Kondensationsgrad und zur Temperatur von Korundpartikeln in AGB-Sternumgebungen zur Verfügung
- **Dr. Attila Juhasz** – Stellte die Hergig Ae/Be-Sternspektren zur Verfügung
- **Dr. Ortrud Wehrhan** – Stellte die Kristallachsenorientierung der Olivin Kristalle fest

Weitere Personen waren an der inhaltlich-materiellen Erstellung der vorliegenden Arbeit nicht beteiligt. Insbesondere habe ich hierfür nicht die entgeltliche Hilfe von Vermittlungs- bzw. Beratungsdiensten (Promotionsberater oder andere Personen) in Anspruch genommen. Niemand hat von mir unmittelbar oder mittelbar geldwerte Leistungen für Arbeiten erhalten, die im Zusammenhang mit dem Inhalt der vorgelegten Dissertation stehen.

Die Arbeit wurde bisher weder im In- noch im Ausland in gleicher oder ähnlicher Form einer Prüfungsbehörde vorgelegt.

Die geltende Promotionsordnung der Physikalisch-Astronomischen Fakultät ist mir bekannt.

Ich versichere ehrenwörtlich, dass ich nach bestem Wissen die reine Wahrheit gesagt und nichts verschwiegen habe.

Ort, Datum Unterschrift des Verfassers

Lebenslauf

Persönliche Daten

Simon Zeidler
Talstraße 27
07745 Jena

Tel.:0179/7191361
Email:szirulan@gmx.de

Geb. am 28.08.1982 in Halle/Saale
Ledig, deutsch

Schulbildung

08/1989–07/1993	Grundschule "Leipziger Straße", Magdeburg
09/1993–01/1997	Geschwister-Scholl-Gymnasium in Magdeburg
01/1997–06/2002	Gymnasium Egeln in Egeln(Sachsen-Anhalt, Salzlandkreis) Abschluss: Abitur mit Note: 1,2

Wehrdienst

10/2002–12/2002	Grundausbildung (4.Kompanie, PzGrLehrbatallion Munster)
01/2003–06/2003	Wehrpflichtiger (1.Kompanie, PzGrLehrbatallion Munster), Tätigkeit als Büroangestellter der Kfz-Gruppe

Studium

10/2003–09/2005	Physikvordiplom an der Friedrich-Schiller Universität Jena Note: 1,7
05/2008–07/2008	Studentische Hilfskraft am astrophysikalischen Institut und Universitätssternwarte Jena
10/2008–02/2009	Studentische Hilfskraft am astrophysikalischen Institut und Universitätssternwarte Jena
10/2005–03/2009	Physikdiplom an der Friedrich-Schiller Universität Jena Note: 1,32 Schwerpunktfach: Stellarphysik Diplomarbeit mit dem Thema: *Spektroskopie amorpher und hydrierter Silikate bei tiefen Temperaturen*

Promotionsstudium

04/2009	Beginn des Promotionsstudiums an der Friedrich Schiller Universität Jena
06/2009–08/2009	Forschungsaufenthalt in Osaka(Japan) im Rahmen des "JSPS summer-program"
10/2009–12/2009	Beschäftigung als wissenschaftliche Hilfskraft an der Friedrich Schiller Universität Jena
01/2010–heute	Wissenschaftlicher Mitarbeiter (Drittmittel) an der Friedrich Schiller Universität Jena Bearbeitung des Forschungsprojekts: "Measurement of the high-temperature optical constants of solar nebula minerals" im Rahmen des Schwerpunktprogramms 1385 der Deutschen Forschungsgesellschaft (DFG): "The First 10 Million Years of the Solar System - A Mineralogical Approach"

Ort, Datum Unterschrift

Danksagung

Hiermit möchte ich allen von Herzen Danken, die für die Entstehung dieser Arbeit unerlässlich waren. Allen voran, den Leiter der Laborgruppe des astrophysikalischen Instituts Dr. Harald Mutschke, ohne den ich mit Sicherheit einen anderen Weg in meinem Leben eingeschlagen hätte und der mir immer mit Rat, Tat und Motivation zur Seit stand. Desweiteren danke ich Gabriele Born für ihre aufopfernde Unterstützung in der Vorbereitung der für die hier präsentierten Messungen verwendeten Proben. Dr. Thomas Posch danke ich für die vielen anregenden Gespräche und die Begeisterung für AGB Sterne, die er in mir geweckt hat.

Vielen Dank an meine ganze Familie, die mich immer in meinem Weg bestärkt und gefördert hat und danke auch an meine vielen Freunde, die mich zur rechten Zeit zu notwendigen Pausen von der Arbeit verleiteten.

Ganz besonderen Dank aber richte ich an meine Verlobte, ohne die ich nicht die Kraft gehabt hätte die Arbeit in der kurzen Zeit anzufertigen und die mir immer mit tröstenden Worten Beistand leistete und mich motivierte weiterzumachen. Danke!